Argonne NATIONAL LABORATORY

ANL/LWRS-18/01

Implementation of ANL's Mechanics Based Evolutionary Fatigue Modeling Through ABAQUS-WARP3D Based High-Performance Computing Framework

With Application to Fatigue Evaluation of PWR Surge Line under Design-Basis Loading Cycles

Nuclear Engineering Division

About Argonne National Laboratory

Argonne is a U.S. Department of Energy laboratory managed by UChicago Argonne, LLC under contract DE-AC02-06CH11357. The Laboratory's main facility is outside Chicago, at 9700 South Cass Avenue, Argonne, Illinois 60439. For information about Argonne and its pioneering science and technology programs, see www.anl.gov.

ANL/LWRS-18/01

Implementation of ANL's Mechanics Based Evolutionary Fatigue Modeling Through ABAQUS-WARP3D Based High-Performance Computing Framework

With Application to Fatigue Evaluation of PWR Surge Line under Design-Basis Loading Cycles

Subhasish Mohanty, Bipul Barua, Joseph Listwan, Saurin Majumdar, and Ken Natesan

Nuclear Engineering Division, Argonne National Laboratory

April 2018

This page intentionally left blank

ABSTRACT

This report presents an update on the environmental fatigue research that is being conducted at Argonne National Laboratory in support of the Department of Energy's Light Water Reactor Sustainability (LWRS) program. Argonne is developing a fully mechanistic fatigue evaluation approach without using empirical fatigue (S~N) curves. This approach is based on the fundamental concept of the time evolution of progressive fatigue damage rather than on the conventional S~N curve approaches using end-of-life data. In FY 2017, we performed extensive validation of this approach with respect to fatigue test data for 316 stainless steel [1]. This validation was performed for different loading cases, including constant, variable, and random amplitude. In the present FY 2018 semi-annual report, we present the further advances of Argonne's environmental fatigue research work in the context for more practical applications. In this report, we discuss a methodology for fully mechanistic (i.e., not using S~N curves) fatigue life evaluation of reactor components subjected to realistic loading cycles, namely, design-basis loading cycles. The loading cycles include plant heat-up, full-power, and cool-down operations. As a test case, we considered a typical pressurized water reactor surge line, which is made of 316 SS. To perform the fatigue simulation for thousands of fatigue cycles in a computationally cost effective way, we modified our previous desktop-based finite element (FE) modeling approach to work in a high-performance computing (HPC) framework. For the HPC implementation, we developed a hybrid framework based on commercial FE software (ABAQUS), open-source FE software (WARP3D), and Argonne-developed evolutionary cyclic-plasticity modeling methods. We validated this HPC-based cycle-by-cycle damage model for the entire fatigue life of a Pressurized Water Reactor (PWR) surge line (SL) pipe with respect to assumed loading cycles. The simulated fatigue life was found to be 5855 cycles, which is 85% accurate as compared to the corresponding small-specimen-based experimental fatigue life (6914 cycles). Also, the simulated stress history captures the cyclic hardening and softening behavior of the material for entire fatigue cycles. The FE simulation of the PWR SL pipe was conducted in a reasonable time of 12.5 days. **These results show the promise that a fully mechanistic (not using S~N curves) fatigue life evaluation of a safety-critical nuclear reactor component (or even other safety critical components like those in aircraft, aero-engines, etc.) is possible.** We anticipate that this type of methodology will drastically reduce the uncertainly associated with conventional fatigue life estimates based on empirical S~N curves. We also proposed an FE model that is based on a hybrid full-component and single-element approach and that can readily be used by industry if HPC resources are not available. In this approach, a single-cycle FE simulation has to be performed first for the required loading cycle. Then, the resulting strain/stress profile at the hotspot (highest strain/stress location) is used as input strain/stress loading to the single-element FE model. The single-element FE model is run under multiple fatigue cycles as long as the failure criteria are achieved. The cycle number at failure gives the fatigue life of the component in question. This cost-effective framework does not require expensive HPC hardware and can be performed in a reasonable time by using a desktop computer. We demonstrated this approach with respect to PWR SL fatigue evaluation under two realistic design-basis loading cycles (simple and detailed). The associated results were validated with respect to test data obtained through fatigue testing of uniaxial specimens under the in-air condition at 300 °C. The approach is in the development stage and requires further improvement and validation.

This page intentionally left blank

TABLE OF CONTENTS

Implementation of ANL's Mechanics Based Evolutionary Fatigue Modeling Through ABAQUS-WARP3D Based High-Performance Computing Framework ..... *i*

ABSTRACT ..... *i*

Table of Contents ..... *iii*

List of Figures ..... *v*

List of TABLES ..... *x*

Abbreviations ..... *xi*

Acknowledgments ..... *xii*

1 Organization of This Report *1*

2 ABAQUS Based Single-Cycle Heat Transfer and Structural Analysis of PWR Surge Line under Design-Basis Loading Cycles *2*

2.1 Heat Transfer Analysis **5**

2.1.1 Heat transfer analysis of SL pipe subjected to case 1: simplified design-basis loading cycle 5

2.1.2 Heat transfer analysis of SL pipe subjected to case 2: detailed design-basis loading cycle 7

2.2 Structural Analysis **8**

2.2.1 **Structural analysis of SL pipe subjected to case 1: simplified design-basis loading cycle** 8

2.2.2 **Structural analysis of SL pipe subjected to case 2: detailed design-basis loading cycle** 19

3 Fatigue Experiment Results *33*

3.1 ET-F47 Fatigue Test Subjected to Case 1 ..... **34**

3.2 ET-F48 Fatigue Test Results under Case 2 ..... **38**

4 Implementation and Validation of Fully Mechanistic Modeling in an ABAQUS-WARP3D High Performance Computing Framework *42*

4.1 High Performance Computing Framework **43**

4.1.1 OpenMP Approach 44

4.1.2 Message Passing Interface Approach 45

4.1.3 Hybrid MPI + OpenMP Approach 46

4.2 Framework for Fully Mechanistic Fatigue Evaluation using HPC **46**

4.3 Fully Mechanistic Fatigue Evaluation of PWR SL Pipe under Ideal Loading **47**

4.3.1 Computational Time vs. Number of CPUs 49

4.3.2 Full-Life Fatigue Simulation and Comparison with Experiment 50

5 Finite Element Full-Life Simulation of Fatigue Specimen Subjected to PWR-SL Experienced Design-Basis Loading Profiles *52*

5.1 Full-Life Simulation of ET-F47 Specimen Subjected to Case 1: Simplified Design-Basis Loading Profile **55**

5.2 Full-Life Simulation of ET-F48 Specimen Subjected to Case 2: Detailed Design-Basis Loading Profile **58**

6 Summary and Future Study 62

6.1 Summary 62

6.2 Future Work 62

References 63

LIST OF FIGURES

Figure 2. 1 Finite element model of a typical PWR type surge line used for heat transfer and structural analysis simulation. 2
Figure 2. 2 Temperature boundary conditions applied to HT analysis model of SL under case 1: simplified design-basis loading cycle. 3
Figure 2. 3 Temperature boundary conditions applied to HT analysis model of SL under case 2: detailed design-basis loading cycle: (a) full cycle, (b) during heat-up, and (c) during cool-down. 4
Figure 2. 4 Simulated temperature histories at typical nodes near pressurizer end, mid-section, and HL end of SL for case 1. 6
Figure 2. 5 Simulated temperature contour of SL at different times for case-1 temperature boundary conditions. 6
Figure 2. 6 Simulated temperature history at typical FE nodes near pressurizer end, mid-section, and HL end of SL for case 2: (a) full cycle, (b) during heat-up, and (c) during cool-down. 7
Figure 2. 7 Simulated temperature contour of SL at different times for case-2 temperature boundary conditions. 8
Figure 2. 8 Contour plots at 20 hr with pressurizer temperature of 344 °C and HL temperature of 326.4 °C: (a) vertical-direction (LE33) total strain, (b) vertical-direction (THE33) thermal strain, and (c) Von Mises stress. The elastic FE simulation was conducted for case 1. 10
Figure 2. 9 Time-dependent total strain (ϵ_{33}^{to}), thermal strain (ϵ_{33}^{θ}), and the corresponding mechanical strain (ϵ_{33}^{me}) along the vertical direction at the centroid of a typical element near pressurizer end. The elastic FE simulation was conducted for case 1. 11
Figure 2. 10 Time-dependent equivalent stress or Von Mises stress (σ_{Mises}) and stress component along the vertical direction (σ_{33}) at the centroid of a typical element near pressurizer end. The elastic FE simulation was conducted for case 1. 11
Figure 2. 11 Elastic FE simulated max. principal stress ($\sigma_{Max.\ prin}$) and min. principal stress ($\sigma_{Min.\ prin}$) at the centroid of a typical element near pressurizer end. The simulation was conducted for case 1. 12
Figure 2. 12 Hysteresis curves ($\epsilon_{33}^{to} \sim \sigma_{33}$ and $\epsilon_{33}^{me} \sim \sigma_{33}$) at the centroid of a typical element near pressurizer end and comparison with respect to tensile test strain~stress curve at 300 °C. The elastic FE simulation was conducted for case 1. 12
Figure 2. 13 Hysteresis curves ($\epsilon_{33}^{to} \sim \sigma_{Mises}$ and $\epsilon_{33}^{me} \sim \sigma_{Mises}$) at the centroid of a typical element near pressurizer end and comparison with respect to tensile test strain~stress curve at 300 °C. The elastic FE simulation was conducted for case 1. 13
Figure 2. 14 Estimated total strain rates (along the vertical direction) at the centroid of a typical element near pressurizer end. The elastic FE simulation was conducted for case 1. 13
Figure 2. 15 Contour plots at 20 hr with pressurizer temperature of 344 °C and HL temperature of 326.4 °C: (a) vertical-direction (LE33) total strain, (b) vertical-direction (THE33) thermal strain, (c) Von Mises stress, and (d) effective plastic strain (PEMAG). The elastic-plastic FE simulation was conducted for case 1. 15
Figure 2. 16 Time-dependent total strain (ϵ_{33}^{to}), thermal strain (ϵ_{33}^{θ}), and the corresponding mechanical strain (ϵ_{33}^{me}) along the vertical direction at the centroid of a typical element near pressurizer end. The elastic-plastic FE simulation was conducted for case 1. 16

Figure 2. 17 Time-dependent equivalent plastic strain magnitude (ϵ_{mag}^{pl}) and plastic strain component along the vertical direction (ϵ_{33}^{pl}) at the centroid of a typical element near pressurizer end. The elastic-plastic FE simulation was conducted for case 1. 16
Figure 2. 18 Time-dependent equivalent stress or Von Mises stress (σ_{Mises}) and stress component along the vertical direction (σ_{33}) at the centroid of a typical element near pressurizer end. The elastic-plastic FE simulation was conducted for case 1. 17
Figure 2. 19 Time-dependent maximum principal stress ($\sigma_{Max.\ prin}$) and minimum principal stress ($\sigma_{Min.\ prin}$) at the centroid of a typical element near pressurizer end. The elastic-plastic FE simulation was conducted for case 1. 17
Figure 2. 20 Hysteresis curves ($\epsilon_{33}^{to}\sim\sigma_{33}$ and $\epsilon_{33}^{me}\sim\sigma_{33}$) at the centroid of a typical element near pressurizer end and comparison with respect to tensile test strain~stress curve at 300 ºC. The elastic-plastic FE simulation was conducted for case 1..... 18
Figure 2. 21 Hysteresis curves ($\epsilon_{33}^{to}\sim\sigma_{Mises}$ and $\epsilon_{33}^{me}\sim\sigma_{Mises}$) at the centroid of a typical element near pressurizer end and comparison with respect to tensile test strain~stress curve at 300 ºC. The elastic-plastic FE simulation was conducted for case 1..... 18
Figure 2. 22 Estimated total strain rates (along the vertical direction) at the centroid of a typical element near pressurizer end. The elastic-plastic FE simulation was conducted for case 1. 19
Figure 2. 23 Contour plots at 1.975 days with pressurizer temperature of 347.3 ºC and HL temperature of 326.4 ºC: (a) vertical-direction total strain, (b) vertical-direction thermal strain, and (c) Von Mises stress. The elastic FE simulation was conducted for case 2..... 20
Figure 2. 24 Time-dependent total strain (ϵ_{33}^{to}), thermal strain (ϵ_{33}^{θ}), and the corresponding mechanical strain (ϵ_{33}^{me}) along the vertical direction at the centroid of a typical element near the pressurizer end. The elastic FE simulation was conducted for case 2 (a) under full cycle, (b) during heat-up, and (c) during cool-down..... 21
Figure 2. 25 Time-dependent equivalent stress or Von Mises stress (σ_{Mises}) and stress along the vertical direction (σ_{33}) at the centroid of a typical element near pressurizer end. The elastic FE simulation was conducted for case 2 (a) under full cycle, (b) during heat-up, and (c) during cool-down. 22
Figure 2. 26 Time-dependent maximum principal stress ($\sigma_{Max.\ prin}$) and minimum principal stress ($\sigma_{Min.\ prin}$) at the centroid of a typical element near pressurizer end. The elastic FE simulation was conducted for case 2 (a) under full cycle, (b) during heat-up, and (c) during cool-down. 23
Figure 2. 27 Hysteresis curves ($\epsilon_{33}^{to}\sim\sigma_{33}$ and $\epsilon_{33}^{me}\sim\sigma_{33}$) at the centroid of a typical element near pressurizer end and comparison with respect to tensile test strain~stress curve for 300 ºC. The elastic FE simulation was conducted for case 2. 23
Figure 2. 28 Hysteresis curves ($\epsilon_{33}^{to}\sim\sigma_{Mises}$ and $\epsilon_{33}^{me}\sim\sigma_{Mises}$) at the centroid of a typical element near pressurizer end and comparison with respect to tensile test strain~stress curve at 300 ºC. The elastic FE simulation was conducted for case 2. 24
Figure 2. 29 Time-dependent total strain rates (along vertical direction) at the centroid of a typical element near pressurizer end. The elastic FE simulation was conducted for case 2 (a) under full cycle, (b) during heat-up, and (c) during cool-down..... 24
Figure 2. 30 Contour plots at 1.975 days with pressurizer temperature of 347.3 ºC and HL temperature of 326.4 ºC: (a) vertical-direction (LE33) total strain, (b) vertical-direction

(THE33) thermal strain, (c) Von Mises stress, and (d) effective plastic strain (PEMAG). The elastic-plastic FE simulation was conducted for case 2..... 26
Figure 2. 31 Time-dependent total strain (ϵ_{33}^{to}), thermal strain (ϵ_{33}^{θ}), and the corresponding mechanical strain (ϵ_{33}^{me}) along the vertical direction at the centroid of a typical element near pressurizer end. The elastic-plastic FE simulation was conducted for case 2 (a) under full cycle, (b) during heat-up, and (c) during cool-down. 27
Figure 2. 32 Time-dependent equivalent plastic strain magnitude (ϵ_{mag}^{pl}) and plastic strain component along the vertical direction (ϵ_{33}^{pl}) at the centroid of a typical element near pressurizer end. The elastic-plastic FE simulation was conducted for case 2 (a) under full cycle, (b) during heat-up, and (c) during cool-down. 28
Figure 2. 33 Time-dependent equivalent stress or Von Mises stress (σ_{Mises}) and stress component along the vertical direction (σ_{33}) at the centroid of a typical element near pressurizer end. The elastic-plastic FE simulation was conducted for case 2 (a) under full cycle, (b) during heat-up, and (c) during cool-down. 29
Figure 2. 34 Time-dependent maximum principal stress ($\sigma_{Max.\ prin}$) and minimum principal stress ($\sigma_{Min.\ prin}$) at the centroid of a typical element near pressurizer end. The elastic-plastic FE simulation was conducted for case 2 (a) under full cycle, (b) during heat-up, and (c) during cool-down..... 30
Figure 2. 35 Hysteresis curves ($\epsilon_{33}^{to} \sim \sigma_{33}$ and $\epsilon_{33}^{me} \sim \sigma_{33}$) at the centroid of a typical element near pressurizer end and comparison with tensile test strain~stress curve for 300 ^{o}C. The elastic-plastic FE simulation was conducted for case 2 (a) under full cycle, (b) during heat-up, and (c) during cool-down..... 31
Figure 2. 36 Hysteresis curves ($\epsilon_{33}^{to} \sim \sigma_{Mises}$ and $\epsilon_{33}^{me} \sim \sigma_{Mises}$) at the centroid of a typical element near pressurizer end and comparison with tensile test strain~stress curve for 300 ^{o}C. The elastic-plastic FE simulation was conducted for case 2 (a) under full cycle, (b) during heat-up, and (c) during cool-down..... 31
Figure 2. 37 Time-dependent total strain rates (along the vertical direction) at the centroid of a typical element near pressurizer end. The elastic-plastic FE simulation was conducted for case 2 (a) under full cycle, (b) during heat-up, and (c) during cool-down. 32

Figure 3. 1 ET-F47 input strain profile. The profile was estimated based on elastic-plastic FE model of PWR surge line pipe that was subjected to case 1..... 35
Figure 3. 2 Observed stress history from ET-F47 test. The fatigue specimen was subjected to asymmetric (with non-zero baseline) strain input obtained from FE model with case 1. 35
Figure 3. 3 Observed fatigue cycle versus maximum stress amplitudes for ET-F47 test. The fatigue specimen was subjected to asymmetric (with non-zero baseline) strain input obtained from FE model with case 1. 36
Figure 3. 4 Observed fatigue cycle versus maximum stress amplitudes in our earlier conducted ET-F13 test. The fatigue specimen was subjected to symmetric (zero baseline) stroke loading (frame crosshead displacement) or equivalent symmetric gauge area symmetric strain loading [4]..... 36
Figure 3. 5 First 10 cycle of hysteresis (input strain versus observed stress) curves for ET-F47 test. The fatigue specimen was subjected to asymmetric (with non-zero baseline) strain input obtained from FE model with case 1. 37

Figure 3. 6 First 10 cycle of input strain history for ET-F47 test. The fatigue specimen was subjected to asymmetric (with non-zero baseline) strain input obtained from FE model with case 1. 37
Figure 3. 7 First 10 cycle of observed stress history for ET-F47 test. The fatigue specimen was subjected to asymmetric (with non-zero baseline) strain input obtained from FE model with case 1. 38
Figure 3. 8 ET-F48 input strain profile. The profile was estimated based on elastic-plastic FE model of PWR surge line pipe for case 2. 39
Figure 3. 9 Observed stress history from ET-F48 test. The fatigue specimen was subjected to asymmetric (with non-zero baseline) strain input obtained from FE model for case 2. 39
Figure 3. 10 Observed fatigue cycle versus maximum stress amplitudes for ET-F48 test. The fatigue specimen was subjected to asymmetric (with non-zero baseline) strain input obtained from FE model for case 2. 40
Figure 3. 11 First 10 cycles of hysteresis curves (input strain versus observed stress) for ET-F48. The fatigue specimen was subjected to asymmetric (non-zero baseline) strain input obtained from FE model for case 2. 40
Figure 3. 12 First 10 cycles of input strain history for ET-F48. The fatigue specimen was subjected to asymmetric (with non-zero baseline) strain input obtained from FE model for case 2. 41
Figure 3. 13 First 10 cycles of observed stress history for ET-F48 test. The fatigue specimen was subjected to asymmetric (non-zero baseline) strain input obtained from FE model for case 2. 41

Figure 4. 1 Flowchart showing the steps in mechanistic-based fatigue modeling framework. 43
Figure 4. 2 Shared memory system where Processor 1, 2, 3, and 4 can see whole memory (OpenMP). 44
Figure 4. 3 Illustration of multi-threading during OpenMP. 45
Figure 4. 4 Distributed memory system where CPUs can see only limited memory of their own and communicate via message passing through a network cable (MPI). 45
Figure 4. 5 Hybrid MPI + OpenMP model for a cluster of four nodes. 46
Figure 4. 6 Schematic of ANL's approach for fully mechanistic fatigue evaluation of large components/systems using high performance computing. 47
Figure 4. 7 (a) FE mesh of the PWR SL pipe. Blue arrows at two ends show the fixed boundary condition, (b) yellow arrows indicate the location and direction of applied cyclic displacement. (c) profile of the applied cyclic displacement. 48
Figure 4. 8 Contour plot (from ABAQUS simulation) of the von Misses stress at an instant during the displacement control fatigue loading shown in Figure 4.7. The highlighted element in the magnified inset is the element of interest for analyzing results from full life simulation using WARP3D and hybrid MPI + OpenMP. 51
Figure 4. 9 Von Mises stress amplitudes from experiment and simulation. 51

Figure 5. 1 Three-dimensional 8-node brick element used for FE simulation of fatigue experiment in WARP3D. 53
Figure 5. 2 APSE-dependent elastic modulus. 53
Figure 5. 3 APSE-dependent elastic limit stresses, which was used as the yield stress. 54
Figure 5. 4 APSE-dependent nonlinear kinematic hardening parameter C_1. 54

Figure 5. 5 APSE-dependent nonlinear kinematic hardening parameter, γ1. 55
Figure 5. 6 Simulated stress profile for ET-F47 fatigue specimen under case 1 (strain input shown in Figure 3.1). 56
Figure 5. 7 First 10 cycles of simulated stress-strain hysteresis curves for ET-F47 (case 1). 57
Figure 5. 8 First 10 cycles of simulated stress history for ET-F47 (case 1). 57
Figure 5. 9 Simulated fatigue cycles versus maximum stress amplitudes for ET-F47 (case 1). . 58
Figure 5. 10 Simulated stress history for ET-F48 fatigue specimen under case 2 (strain input shown in Figure 3.8). 59
Figure 5. 11 First 10 cycles of simulated stress-strain hysteresis curves for ET-F48 (case 2). ... 59
Figure 5. 12 First 10 cycles of simulated stress history for ET-F48 (case 2). 60
Figure 5. 13 Simulated fatigue cycles versus maximum stress amplitudes for ET-F48 (case 2). 60

LIST OF TABLES

Table 4. 1 Computation time as a function of CPUs to simulate PWR SL for 10 fatigue cycles using ABAQUS 49
Table 4. 2 Computation time as a function of CPUs to simulate PWR SL for 10 fatigue cycles using WARP3D and HPC 50

Table 5. 1 Experimental and simulated fatigue life under different design basis loading types . 56

ABBREVIATIONS

3D	Three Dimensional
ANL	Argonne National Laboratory
ASME	American Society of Mechanical Engineers
APSE	Accumulated Plastic Strain Energy
CFD	Computational Fluid Dynamics
FE	Finite Element
HL	Hot Leg
HPC	High Performance Computing
HT	Heat Transfer
ID	Inner Diameter
LWRS	Light Water Reactor Sustainability
MP	Multi-Processing
MPI	Message Passing Interface
OpenMP	Open Multi-Processing
PWR	Pressurized Water Reactor
SL	Surge Line
SS	Stainless Steel

ACKNOWLEDGMENTS

This research was supported through the U.S. Department of Energy's Light Water Reactor Sustainability program under the work package of environmental fatigue study, program manager Dr. Keith Leonard.

This page intentionally left blank

1 Organization of This Report

This report is organized in to following sections:

Section 1: Organization of this report

Section 2: ABAQUS Based Single-Cycle Heat Transfer and Structural Analysis of PWR Surge Line under Design-Basis Loading Cycles

Section 3: Fatigue Experiment Results

Section 4: Implementation and Validation of Fully Mechanistic Modeling in an ABAQUS-WARP3D High Performance Computing Framework

Section 5: Finite Element Full-Life Simulation of Fatigue Specimen Subjected to PWR-SL Experienced Design-Basis Loading Profiles

Section 6: Summary and Future Study

2 ABAQUS Based Single-Cycle Heat Transfer and Structural Analysis of PWR Surge Line under Design-Basis Loading Cycles

Finite element (FE) models of a typical PWR surge line (SL) were constructed to perform a heat transfer and the subsequent structural analysis. In FY 2017 we simulated the PWR SL under different transient conditions [1], that is, without considering the full reactor cycle. In this report, we present FE model results of the SL pipe under full reactor cycle, which includes plant heat-up, full-power, and cool-down operations. The FE model of the SL pipe is shown in Figure 2.1.

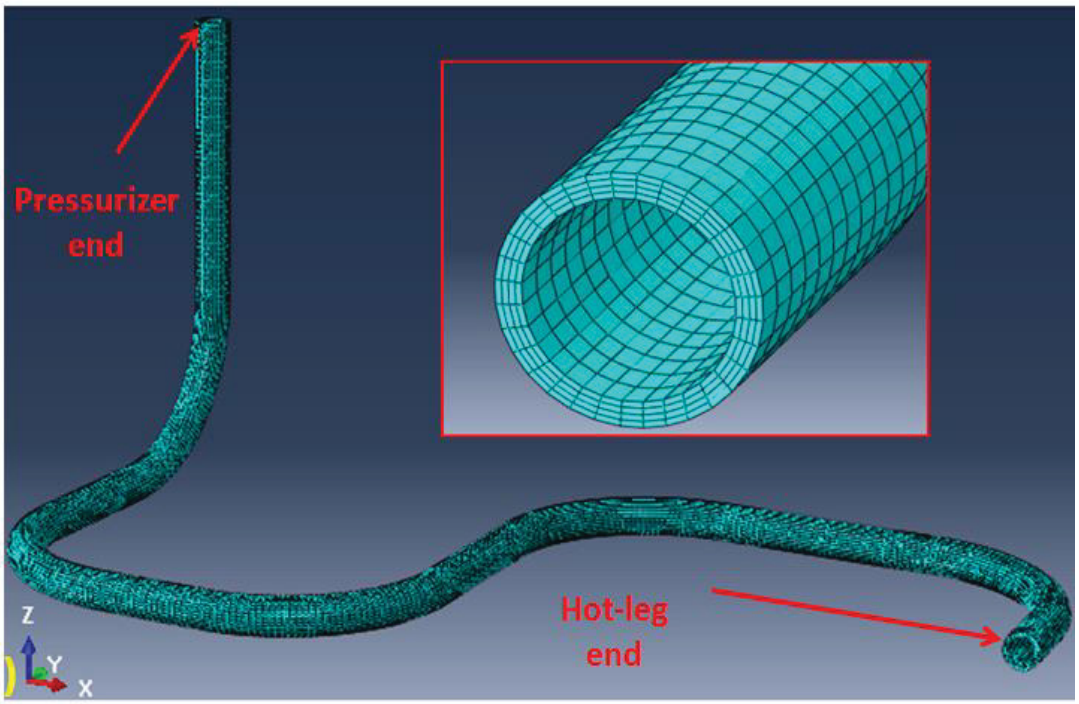

Figure 2. 1 Finite element model of a typical PWR type surge line used for heat transfer and structural analysis simulation.

The full cycle simulation of the SL pipe involved two types of design basis loading cycles, described below.

Case 1: Simplified design-basis loading cycle. This case uses a one-step and single-loading rate both during heat-up (from initial cold shut-down condition to hot standby) and cool-down (from hot standby to initial cold shut-down condition). It is a simplification of the detailed multi-step approach typically followed during actual reactor heat-up and cool-down operations. The maximum temperatures (during full power operation) for the pressurizer and hot leg (HL) were considered equal to 651.2 ºF (344 ºC) and 619.52 ºF (326.4 ºC), respectively. At the start and end of the cycle (i.e., during the cold shut-down condition), the temperature of the pressurizer and HL were assumed equal to 131 ºF (55 ºC). With a single heating rate of 34.68 ºF/hr, the pressurizer end of the SL was heated up from 131 ºF to 651.2 ºF over 15 hours. The same cooling rate was followed to cool down the pressurizer end from 651.2 ºF to the initial 131 ºF over 15 hours. To reach the hot-standby condition, the HL end was heated from 131 ºF

(55 ºC) to 557 ºF (291.67 ºC) at a rate of 28.4 ºF/hr. From hot standby, the HL was heated to full power with temperature of 619.52 ºF (326.4 ºC) over 2 hours with a heat-up rate of 31.26 ºF/hr. A symmetric cooling rate was followed for the HL end of the SL, with the cooling rate being the same as the heating rate. For the heat transfer analysis, the above-mentioned temperature boundary conditions were applied at the pressurizer and HL ends of the SL pipe. The inner diameter (ID) surface of the SL applied with an average temperature history (pressurizer and HL end temperature histories as estimated for the above-mentioned rates). Note that the heating and cooling rates are similar as the heating and cooling rate information given in an Electric Power Research Institute (EPRI) report [2]. Figure 2.2 shows the resulting temperature boundary conditions applied to the pressurizer and HL end and the average ID wall temperature of the SL pipe.

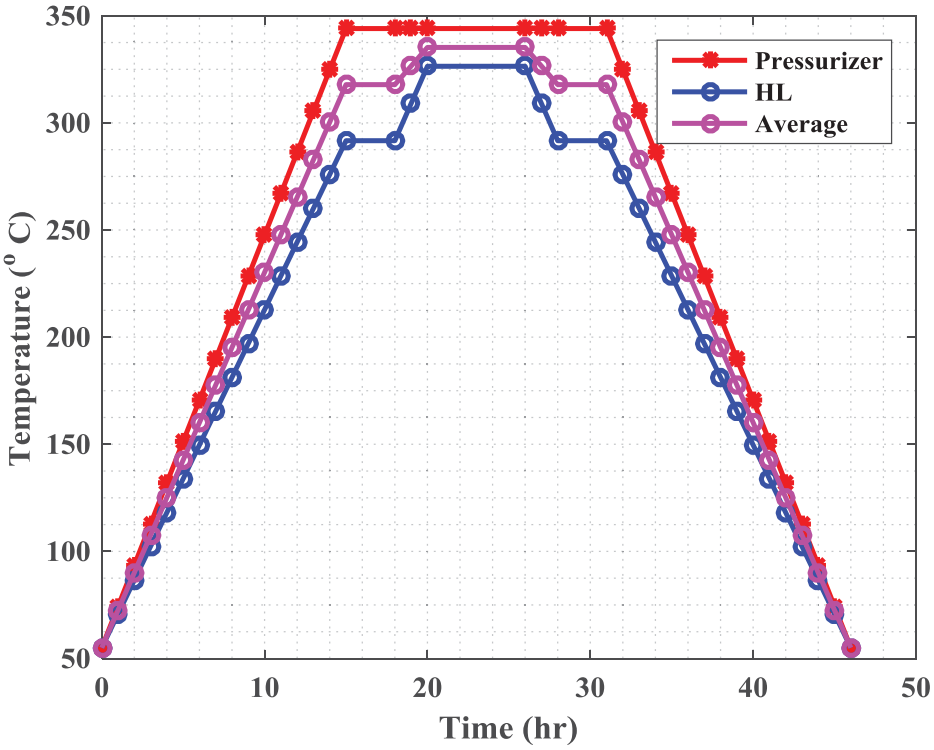

Figure 2. 2 Temperature boundary conditions applied to HT analysis model of SL under case 1: simplified design-basis loading cycle.

Case 2: Detailed design-basis loading cycle: This case involves the multi-steps and differential loading rates that are typically followed during heat-up and cool-down operations of real nuclear power plant. To design this loading cycle, we followed the heating and cooling rate of a coolant loop as given in an EPRI document [2]. For example, the EPRI document shows that during a typical heat-up operation, the coolant loop has to be heated at a rate of 10 ºF/hr HU from 80 ºF to 160 ºF, then 23 ºF/hr HU to 183 ºF, then held at 183 ºF for 10.5 hours, then heated up at 33 ºF/hr to 330 ºF, then held at 330 ºF for 2.3 hours, then heated up at 33 ºF/hr to 550 ºF (287.8 ºC), which is the hot standby temperature. For this case, a ssimilar heating rate for the HL is followed with starting temperature of 80 ºF (26.67 ºC) up to the hot standby temperature of 550 ºF (287.8 ºC). The full-power operation temperature for the HL and pressurizer is considered equal to 619.52 ºF (326.4 ºF) and 657.06 ºF (347.3 ºC), respectively. For the discussed loading cycle, a heating rate of 33 ºF/hr was applied to heat up the HL temperature from hot standby to full power. During cool-down, a cooling rate of 33 ºF/hr was followed to reduce the HL

temperature from the full-power to hot-standby condition with a temperature of 550 ºF (287.8 ºC). This was followed by cool-down of the HL at a rate of 75 ºF /hr from 550 ºF (287.8 ºC) to 250 ºF (121.1 ºC), then 46 ºF /hr to 175 ºF (79.4 ºC). The temperature was held at 175 ºF (79.4 ºC) for 12 hours, then cooled down at 26 ºF /hr to 120 ºF (48.9 ºC), then 6.8 ºF /hr to 80 ºF (26.67 ºC). The temperature history of the pressurizer was estimated by back calculating the temperature for the saturation pressure history given in the EPRI document [2]. The maximum temperature of the pressurizer was considered equal to 657.06 ºF (347.3 ºC) at the saturation pressure of 2252.4 psi (15.53 MPa). The estimated HL and pressurizer temperature histories were applied to the HL and pressurizer end of SL pipe. In addition, the ID wall of SL pipe was subjected to the average the HL and pressurizer temperature. Figure 2.3 show the corresponding temperature histories used as temperature boundary conditions while performing the heat transfer analysis.

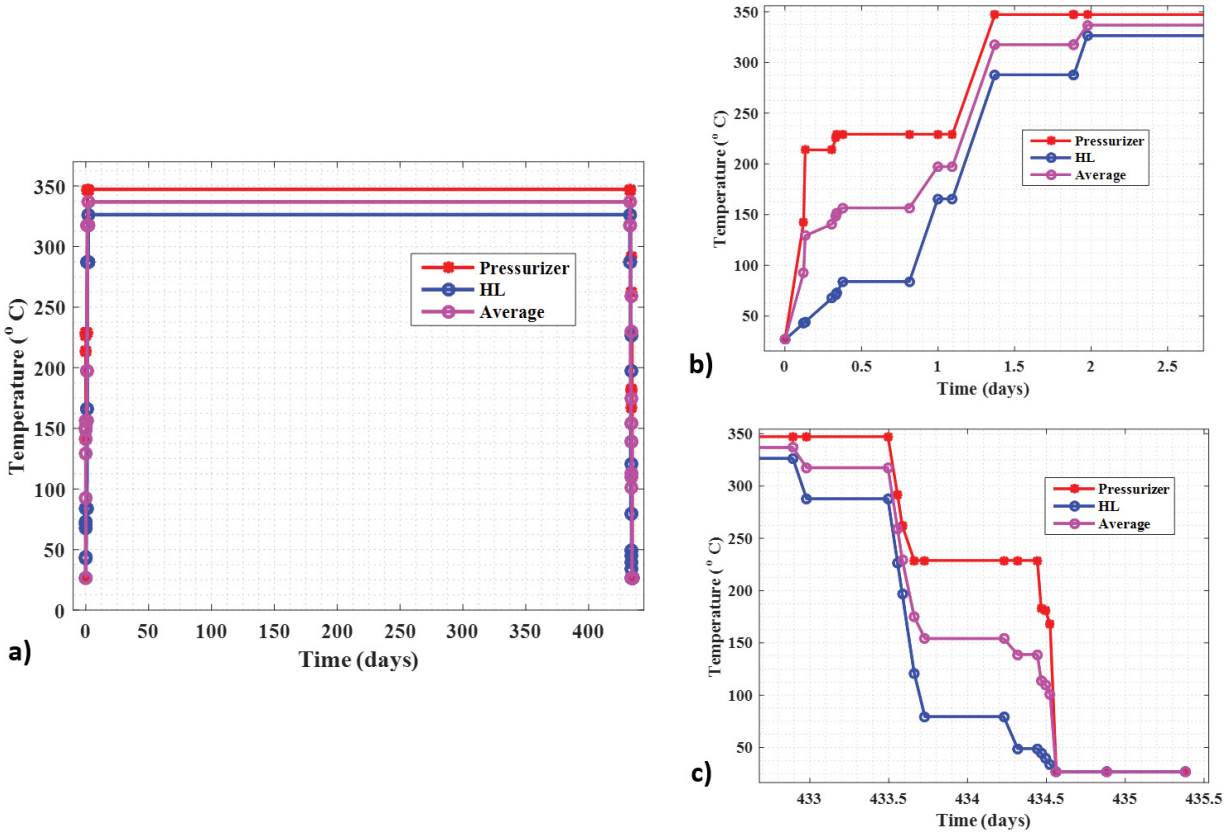

Figure 2. 3 Temperature boundary conditions applied to HT analysis model of SL under case 2: detailed design-basis loading cycle: (a) full cycle, (b) during heat-up, and (c) during cool-down.

For the heat transfer analysis during the full power operation (for the two loading cases), the temperature was assumed constant (as is assumed for typical design-basis loading cycles). The duration of full-power operation for both cases is different and has no bearing on the FE analysis results. The full-power duration was 5 hours for case 1 and 435 days for case 2. The effect of the ID wall pressure and end-cap pressure was not considered in subsequent structural analysis. Only the effect of temperature was considered for two reasons: pressure does not have much effect compared to temperature loading, and we wanted to estimate only the effect of temperature boundary conditions to understand how the temperature alone affects the stress-strain behavior and overall fatigue life

(estimated through the analytical model and fatigue experiments). The structural analysis was performed for both cases based on the nodal temperature from corresponding heat transfer analyses. The details of the material properties used for heat transfer analysis can be found in our previous report [1].

For the structural analysis discussed in this section, we assumed constant temperature properties at 300 ^{o}C (316 SS tensile test properties assuming the elastic limit as the yield limit). The reason for the single temperature is to follow a similar isothermal temperature condition to that of the fatigue test cases discussed in Section 3. The overall aim of this FE model calculation is to estimate the representative strain profile that can be used as input for the isothermal fatigue testing cases. Furthermore, for the structural analysis model we assumed fixed displacement boundary conditions for both the HL and pressurizer end. This is based on the assumption that the fixed boundary conditions would produce the most conservative strain estimate. The overall aim of the discussed work is not to estimate fatigue life of a particular reactor component, but to develop a methodology considering representative loading cases (with representative stress/strain profiles for fatigue testing and for multi-cycle analytical or mechanistic fatigue evaluation).

Below, we discuss the associated heat transfer analysis and structural analysis for a single reactor loading cycle. The aim is to understand the stress-strain behavior under these two loading cases and to estimate the associated strain profiles that can be used further as input loading profiles for subsequent fatigue tests (discussed in Section 3) and multi-cycle fatigue simulation (discussed in Section 5).

2.1 Heat Transfer Analysis

Heat transfer (HT) analyses were performed using the SL FE model shown in Figure 2.1. These analyses were performed to estimate the nodal temperatures that can be passed to the subsequent structural analysis FE models. They were performed for the simplified and detailed design-basis loading cycles. The associated results are discussed below.

2.1.1 Heat transfer analysis of SL pipe subjected to case 1: simplified design-basis loading cycle

First, the HT analyses were performed using the temperature boundary conditions given in Figure 2.2. Note that a detailed computational fluid dynamics (CFD) analysis was not performed before or along with the HT analysis to estimate the exact stratification of temperature along the length of the SL pipe. For simplicity, we directly assumed the temperature boundary conditions at the pressurizer end and HL end of the pipe in addition to average temperature boundary condition at the ID wall of the SL pipe. As mentioned before, the purpose of the discussed work is not to exactly estimate the fatigue behavior of a particular component, but to develop a methodology based on representative data. A detailed CFD analysis to estimate the temperature stratification (under transient loading) is presented in our previous work [1]. Similar thermo-hydraulics analysis for the full reactor cycle loading is planned for the future.

In this reported work, HT analyses were performed using the temperature boundary condition shown in Figure 2.2. Figure 2.4 shows the resulting simulated temperature history at typical nodes near the pressurizer end, mid-section, and HL end of the SL. Figure 2.5 shows the simulated temperature contour of the SL at different times. For these analyses, the maximum temperatures for HL and pressurizer were assumed to be 326.4 ^{o}C and 344 ^{o}C, respectively. The starting (or the minimum) temperature of the reactor coolant system was assumed equal to 55 ^{o}C.

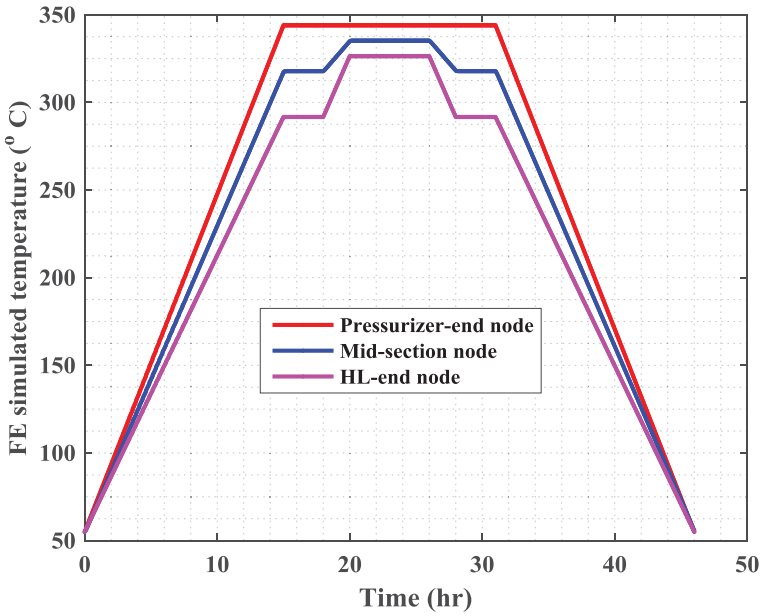

Figure 2. 4 Simulated temperature histories at typical nodes near pressurizer end, mid-section, and HL end of SL for case 1.

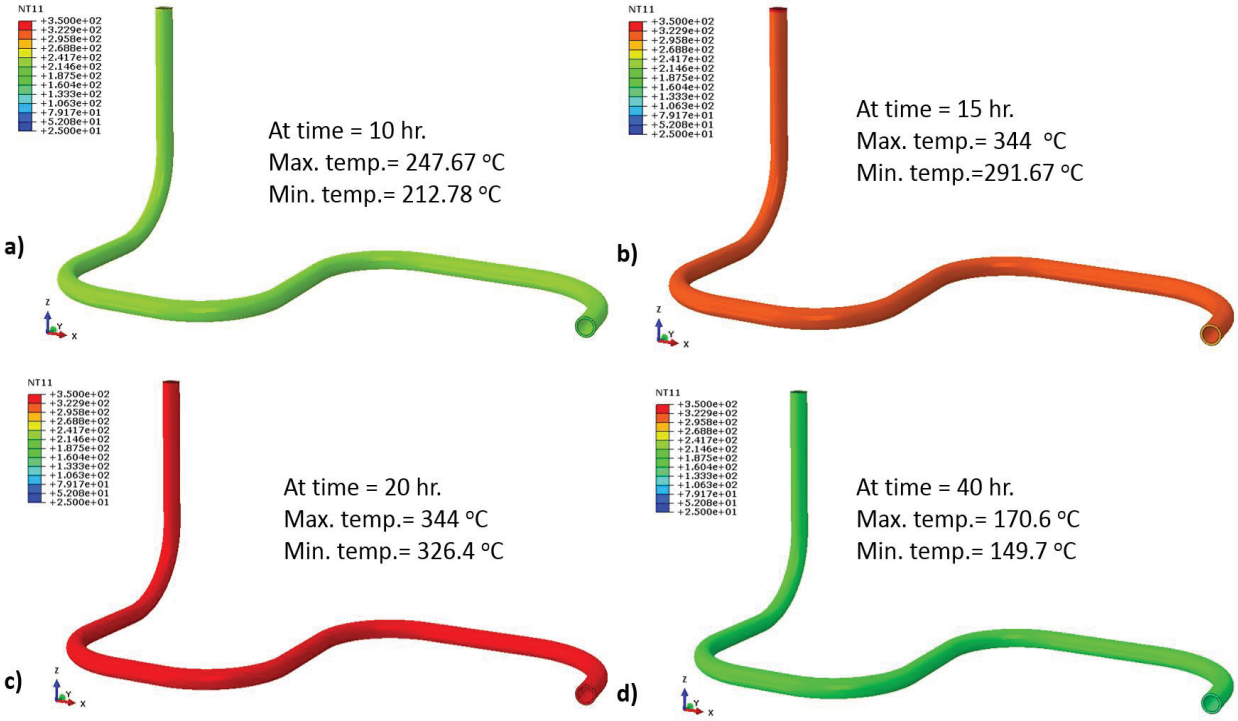

Figure 2. 5 Simulated temperature contour of SL at different times for case-1 temperature boundary conditions.

2.1.2 Heat transfer analysis of SL pipe subjected to case 2: detailed design-basis loading cycle

Another set of HT analyses was performed to estimate the nodal temperature in the SL pipe subjected to case 2, as shown in Figure 2.3. Similar to case 1, for simplicity, a detailed CFD thermal-hydraulics analysis was not performed; instead, a single-stage HT analysis was performed to estimate the nodal temperature in the SL pipe for subsequent structural analysis. Figure 2.6 shows the simulated temperature history at typical FE nodes near the pressurizer end, mid-section, and HL end of the SL pipe. Figures 2.6a, 2.6b, and 2.6c show the temperature history for the full cycle, during heat-up, and during cool-down, respectively. Figure 2.7 shows the simulated temperature contour of the SL at different times.

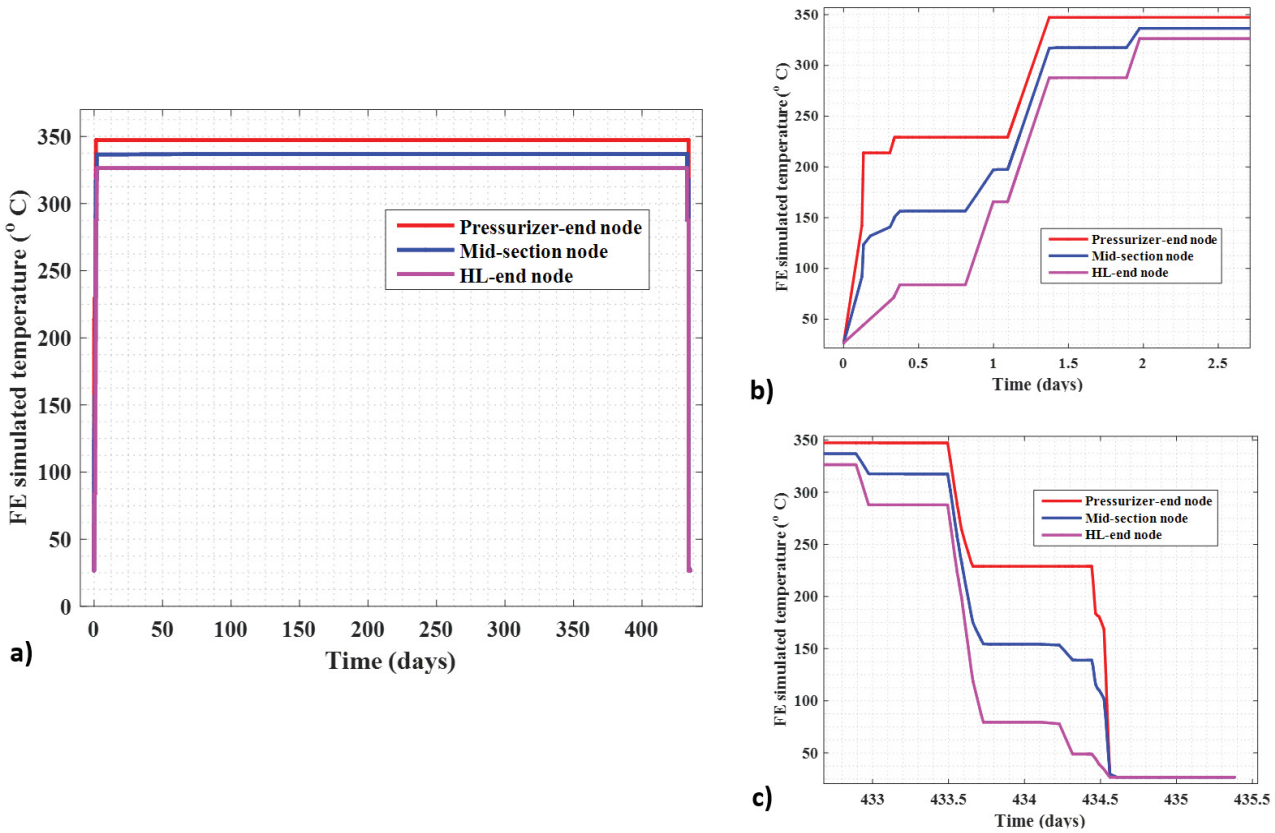

Figure 2. 6 Simulated temperature history at typical FE nodes near pressurizer end, mid-section, and HL end of SL for case 2: (a) full cycle, (b) during heat-up, and (c) during cool-down.

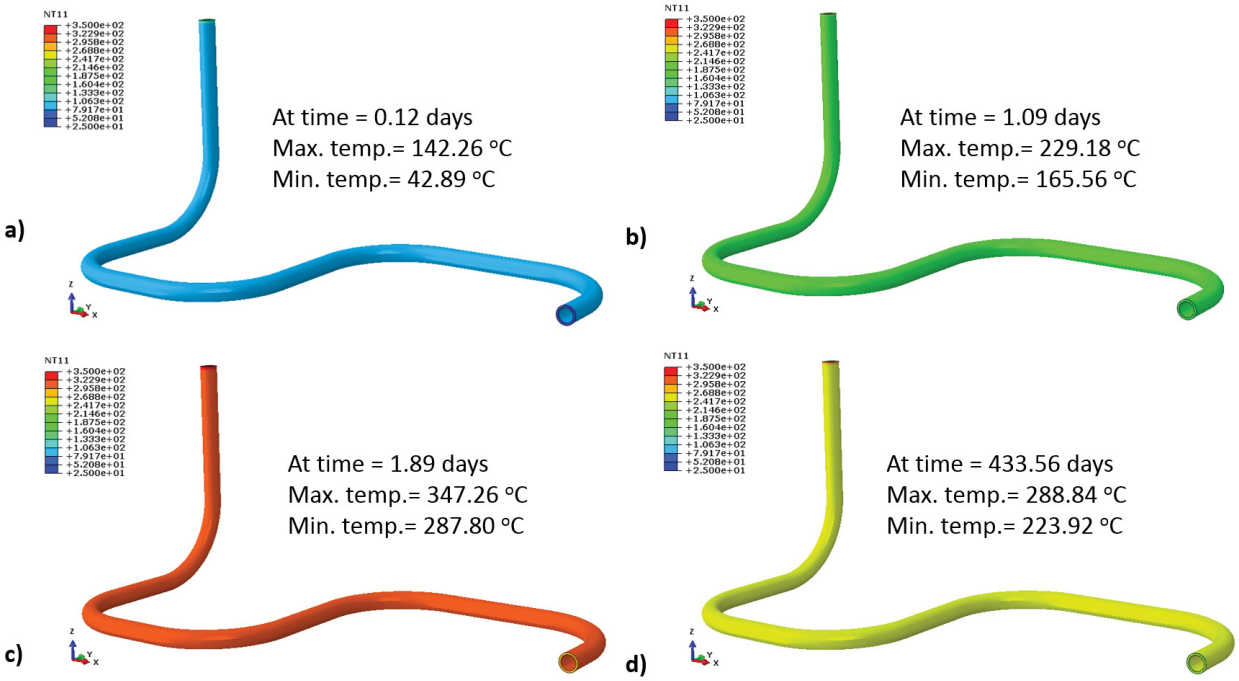

Figure 2. 7 Simulated temperature contour of SL at different times for case-2 temperature boundary conditions.

2.2 Structural Analysis

Structural analyses were performed based on the nodal temperature estimated from the above HT simulations. Both elastic-plastic and elastic analyses were performed to show the importance of performing elastic-plastic analysis compared to the elastic analysis. In general, elastic-analysis results are widely used for fatigue evaluation, which we feel extremely conservative at least for the discussed results. The structural analyses results for both loading cases are discussed below.

*2.2.1 **Structural analysis of SL pipe subjected to case 1: simplified design-basis loading cycle***

2.2.1.1 Elastic analysis under case 1

An elastic analysis was performed to simulate the time-dependent stress-strain in SL pipe subjected to case 1. Figure 2.8 shows the contour plots of total strain and thermal strain (both along the vertical direction) and the equivalent stress or Von Mises stress. These contour plots are at time, when the pressurizer and HL temperatures were at 344 ºC and 326.4 ºC, respectively. From these figures, it can be seen that the pressurizer end experiences higher stress/strain.

Figure 2.9 shows the time-dependent total strain (ϵ_{33}^{to}), thermal strain (ϵ_{33}^{θ}), and the corresponding mechanical strain (ϵ_{33}^{me}) component (along the vertical direction) at the centroid of a typical element near the pressurizer end. The curves show that the total, thermal, and mechanical strains return to their

starting values at the end of the loading cycle. Thermal strain returns to its starting value because of the linear calculation of the thermal strain in the FE model. This is as expected in the absence of creep strain. The rreturn of the total and mechanical strain to their original values is because of the linear elastic-plastic FE analysis.

Figure 2.10 shows a comparison of time-dependent Von Mises stress (σ_{Mises}) with respect to the corresponding stress component along the vertical direction (σ_{33}) at the centroid of a typical element near the pressurizer end of the SL pipe. Figure 2.11 shows the corresponding comparison of time-dependent maximum and minimum principal stresses. Figure 2.10 shows that the maximum Von Mises stress is 850 MPa, where the corresponding Von Mises stress amplitude is 850/2 = 425 MPa. For the fatigue life estimation, the ASME code suggests estimating the stress amplitude based on the principal stress components. With the Figure 2.11 results and ASME code criteria, the maximum stress amplitude is equal to

(1/2)x($\sigma_{Max.\ prin} - \sigma_{Min.\ prin}$)=(1/2)x(300 - (-650)) = 475 MPa

From both these methods of stress amplitude calculation, the amplitude calculation based on the principal stress component is more conservative and to be used for further fatigue evaluation. This is consistent with the ASME code suggestion. Also, Figure 2.10 shows that the Von Mises stress is much higher compared to the individual stress component (along the vertical direction). This is obvious because the Von Mises stress is the magnitude of all stress components. However, according to Figure 2.10, the Von Mises stress is very high compared to the experimental stress from the uniaxial test (see the tensile test stress-strain curves in Figure 2.12 or 2.13). Ideally, the Von Mises stress for a component should be similar to that observed in the uniaxial test. The similarity in experimental and FE results is expected, because for the FE simulation, stress-strain property based on the uniaxial test is used through a multiaxial Von Mises criteria. The large discrepancy in multiaxial FE estimated Von Mises stress with respect to the uniaxial experimental stress is due to the linear elastic FE analysis. A similar discrepancy can be observed in the principal stress results, which produce an unrealistic stress range of

($\sigma_{Max.\ prin} - \sigma_{Min.\ prin}$)=(300 - (-650) = 950 MPa

Also, a discrepancy can be observed in the hysteresis curves shown in Figures 2.12 and 2.13. Although elastic analysis is simple and widely followed for fatigue evaluation, it may not capture the actual elastic-plastic behavior of stress-strain curves. Hence it is essential to perform elastic-plastic structural analysis. These results are discussed in the following sub-section. Nevertheless, we also estimated the strain rate based on the component mechanical strain shown in Figure 2.9. The resulting time-dependent strain rate history is given in Figure 2.14, with a maximum strain rate of approximately 6.75 x 10^{-6} %/s. Note that for the fatigue experiment discussed in Section 3, we used the mechanical strain component (along the vertical direction) as input strain for the strain-controlled fatigue tests. Figure 2.9 indicates that the maximum mechanical strain is 0.35%, whereas the maximum thermal strain is 0.5%.

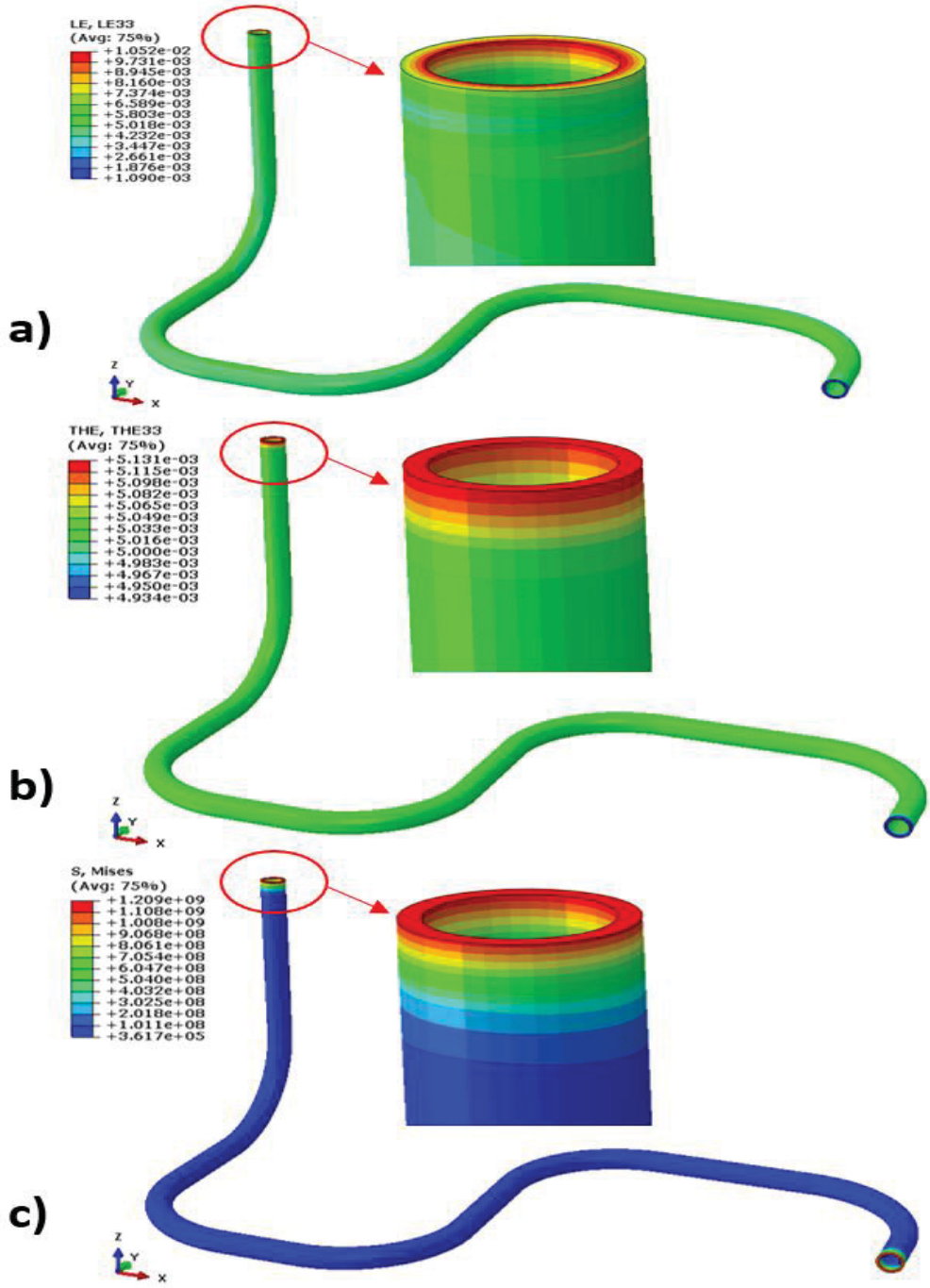

Figure 2. 8 Contour plots at 20 hr with pressurizer temperature of 344 °C and HL temperature of 326.4 °C: (a) vertical-direction (LE33) total strain, (b) vertical-direction (THE33) thermal strain, and (c) Von Mises stress. The elastic FE simulation was conducted for case 1.

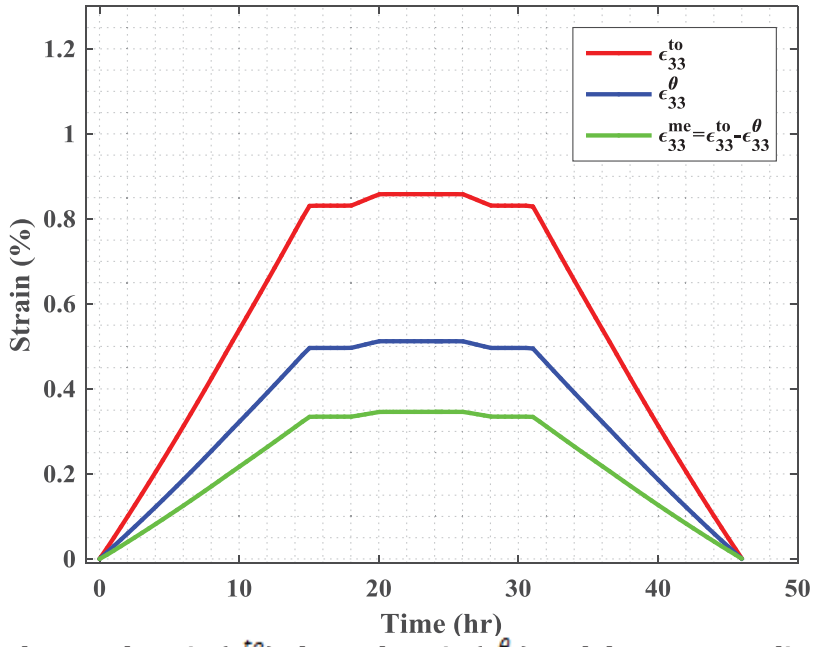

Figure 2. 9 Time-dependent total strain (ϵ_{33}^{to}), thermal strain (ϵ_{33}^{θ}), and the corresponding mechanical strain (ϵ_{33}^{me}) along the vertical direction at the centroid of a typical element near pressurizer end. The elastic FE simulation was conducted for case 1.

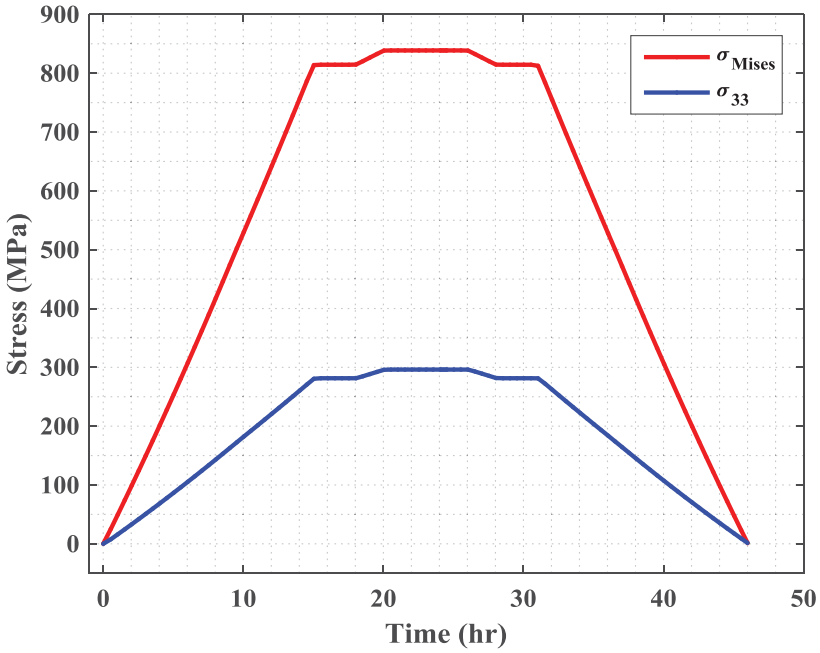

Figure 2. 10 Time-dependent equivalent stress or Von Mises stress (σ_{Mises}) and stress component along the vertical direction (σ_{33}) at the centroid of a typical element near pressurizer end. The elastic FE simulation was conducted for case 1.

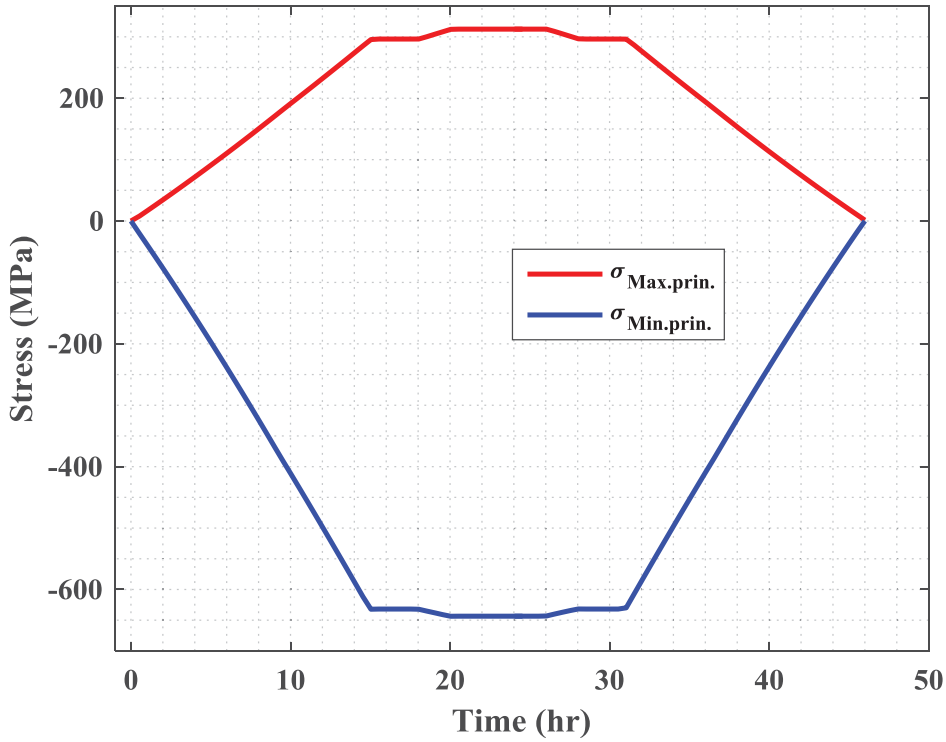

Figure 2. 11 Elastic FE simulated max. principal stress ($\sigma_{Max.\ prin}$) and min. principal stress ($\sigma_{Min.\ prin}$) at the centroid of a typical element near pressurizer end. The simulation was conducted for case 1.

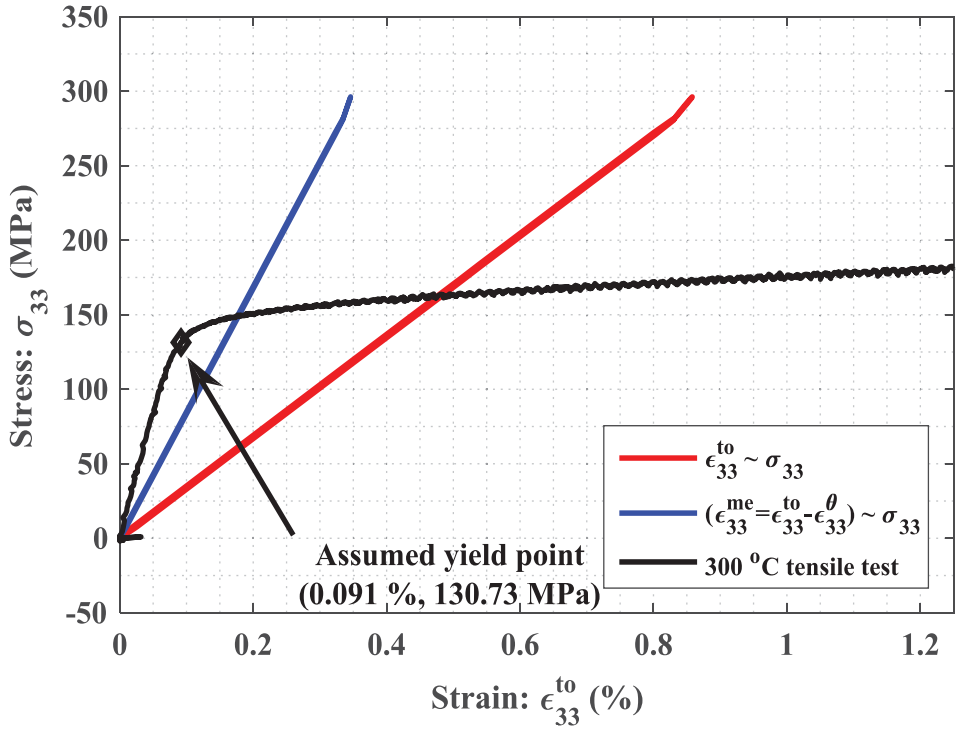

Figure 2. 12 Hysteresis curves ($\epsilon_{33}^{to} \sim \sigma_{33}$ and $\epsilon_{33}^{me} \sim \sigma_{33}$) at the centroid of a typical element near pressurizer end and comparison with respect to tensile test strain~stress curve at 300 °C. The elastic FE simulation was conducted for case 1.

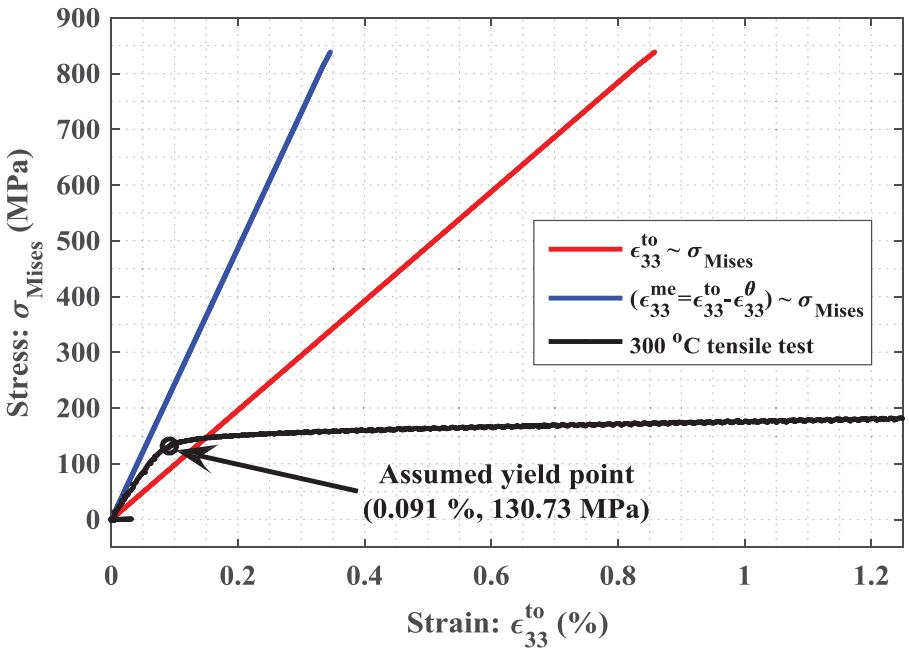

Figure 2. 13 Hysteresis curves ($\epsilon_{33}^{to} \sim \sigma_{Mises}$ and $\epsilon_{33}^{me} \sim \sigma_{Mises}$) at the centroid of a typical element near pressurizer end and comparison with respect to tensile test strain~stress curve at 300 °C. The elastic FE simulation was conducted for case 1.

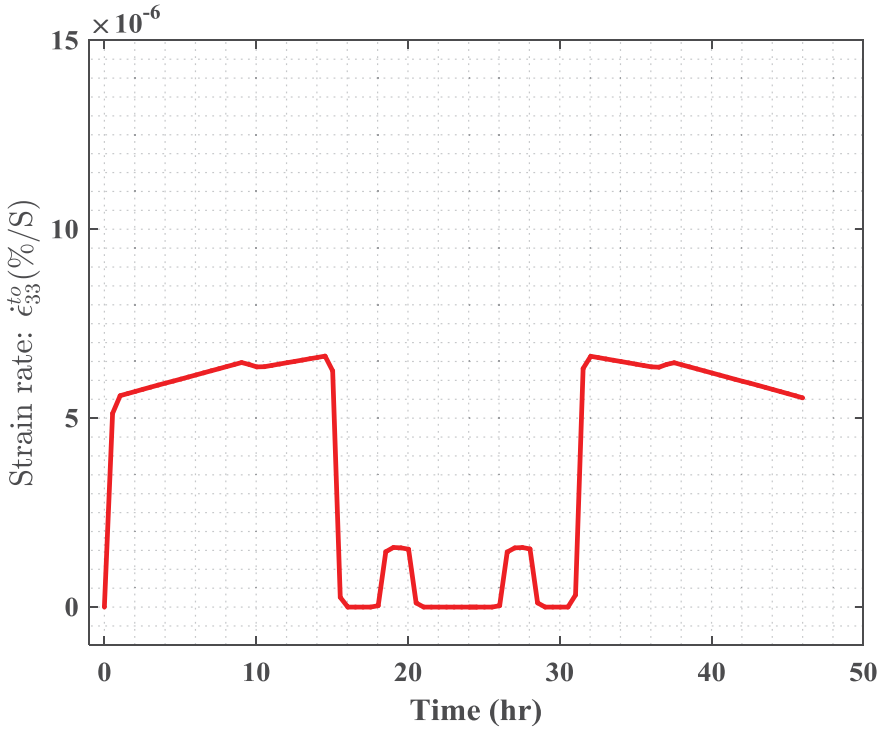

Figure 2. 14 Estimated total strain rates (along the vertical direction) at the centroid of a typical element near pressurizer end. The elastic FE simulation was conducted for case 1.

2.2.1.2 Elastic-plastic analysis results under case 1

In addition to elastic analysis, an elastic-plastic FE analysis of SL pipe was performed under case 1. The objective was to estimate more realistic stress/strain profiles of SL pipe, which can be used for fatigue experiments (discussed in Section 3) and multi-cycle mechanistic fatigue evaluation (discussed in Section 5). Figure 2.15 shows the contour plots of total strain and thermal strain (both along the vertical direction), Von Mises stress, and equivalent plastic strain or plastic strain magnitude with the pressurizer and HL temperatures at 344 ºC and 326.4 ºC, respectively. This figure shows that the pressurizer end experiences higher stress/strain compared to other regions of the SL pipe. Figure 2.16 shows the time-dependent total strain (ϵ_{33}^{to}), thermal strain (ϵ_{33}^{θ}), and the corresponding mechanical strain (ϵ_{33}^{me}) along the vertical direction at the centroid of a typical element near the pressurizer end. Similar to the elastic analysis results, the thermal strain returns to its starting value at the end of the loading cycle. This occurs because of the linear calculation of the thermal strain in the FE model and the lack of thermal creep at the stated temperatures. However, unlike the elastic analysis, the total and mechanical strain do not return to their starting values at the end of the simulation. This occurs because of the nonlinear elastic-plastic FE analysis, which simulates the non-recoverable plastic deformation and associated accumulated plastic strain. Nevertheless, the elastic-plastic analysis results are more realistic since the FE model uses the full elastic-plastic stress-strain curve as the material property rather than just the elastic portion of the stress-strain curve. The non-recoverable plastic deformation is also evident from Figure 2.17, which shows the time-dependent equivalent plastic strain magnitude (ϵ_{mag}^{pl}) and plastic strain along the vertical direction (ϵ_{33}^{pl}) at the centroid of a typical element near the pressurizer end. As shown, at the end of the first cycle the accumulated equivalent plastic strain magnitude (ϵ_{mag}^{pl}) is approximately 0.15%.

Usually, in a stress-controlled loading conditions (similar to a thermal cyclic loading condition as in the present case), the accumulated plastic strain could further grow (leading to strain ratcheting) or could stabilize due to stress hardening and/or a mean stress shifting effect. Conducting a stress-controlled test is highly complex (particularly if the material is subjected to elastic-plastic material behavior [3]). This type of plastic strain accumulation may not be observed in a strain-controlled fatigue test, although strain-controlled testing methods are widely followed for fatigue evaluation of metallic components. We also, for simplicity, performed a strain-controlled fatigue test based on the estimated mechanical strain shown in Figure 2.16. These results will be discussed in Section 3. Figure 2.16 indicates that the maximum mechanical strain is 0.575% at the full-power condition. The corresponding maximum mechanical strain from the elastic analysis is 0.35% (Figure 2.9).

Figure 2.18 shows the time-dependent Von Mises stress (σ_{Mises}) and stress component along the vertical direction (σ_{33}) at the centroid of a typical element near the pressurizer end. Figure 2.19 shows the corresponding time-dependent maximum principal stress ($\sigma_{Max.\ prin}$) and minimum principal stress ($\sigma_{Min.\ prin}$). Figure 2.18 shows that the maximum Von Mises stress is approximately 165 MPa, where the corresponding Von Mises stress amplitude is equal to 165/2= 82.5 MPa, which is much lower than the estimated elastic FE stress amplitude of 425 MPa. Based on the Figure 2.19 results and ASME code criteria, the corresponding stress amplitude from the principal stress components is

(1/2) x($\sigma_{Max.\ prin} - \sigma_{Min.\ prin}$)=(1/2)x(131.25 - (-100)) = 115.6 MPa

Comparing these strain amplitude estimates, the stress amplitude is higher and thus was used for fatigue evaluation as the more conservative life prediction.

Figures 2.20 and 2.21, respectively, show the hysteresis curves with respect to the component stress (σ_{33}) and Von Mises stress (σ_{Mises}). These curves are either with respect to the total strain component (ϵ_{33}^{to}) or the mechanical strain component (ϵ_{33}^{me}). Comparing Figures 2.21 with 2.20 shows that the hysteresis curve with respect to the Von Mises stress better matches the experimental stress-strain curve (both figures are comparable to the tensile test curve for 300 ^{o}C). The comparison matches up to the first stress reversal. After that, the tensile test curve should not be compared since it does not capture the stress reversal behavior as in the case of fatigue loading. Comparing the hysteresis curves $\epsilon_{33}^{to} \sim \sigma_{Mises}$ and $\epsilon_{33}^{me} \sim \sigma_{Mises}$ with the tensile test curve, we determined that the hysteresis curve with respect to mechanical strain (ϵ_{33}^{me}) better matches the tensile stress-strain curve compared to the hysteresis curve with respect to total strain (ϵ_{33}^{to}). Hence, the mechanical strain component should be used as the strain input for the isothermal fatigue test. The FE model-determined mechanical strain will be more representative compared to the total strain component because we used (which is also general practice) material properties from the FE model based on the mechanical stress-strain curves (obtained under isothermal test conditions).

Figure 2.22 shows the time-dependent total strain rates estimated based on the total strain component (ϵ_{33}^{to}) shown in Figure 2.16. This figure shows that the estimated strain rate has a maximum value of 12.25 x 10^{-6} %/s, which is higher than the corresponding elastic FE calculation value of 6.75 x 10^{-6} %/s. However, the stress-strain based on the elastic-plastic FE analysis and derived results is more representative if it is compared with realistic/experimental values.

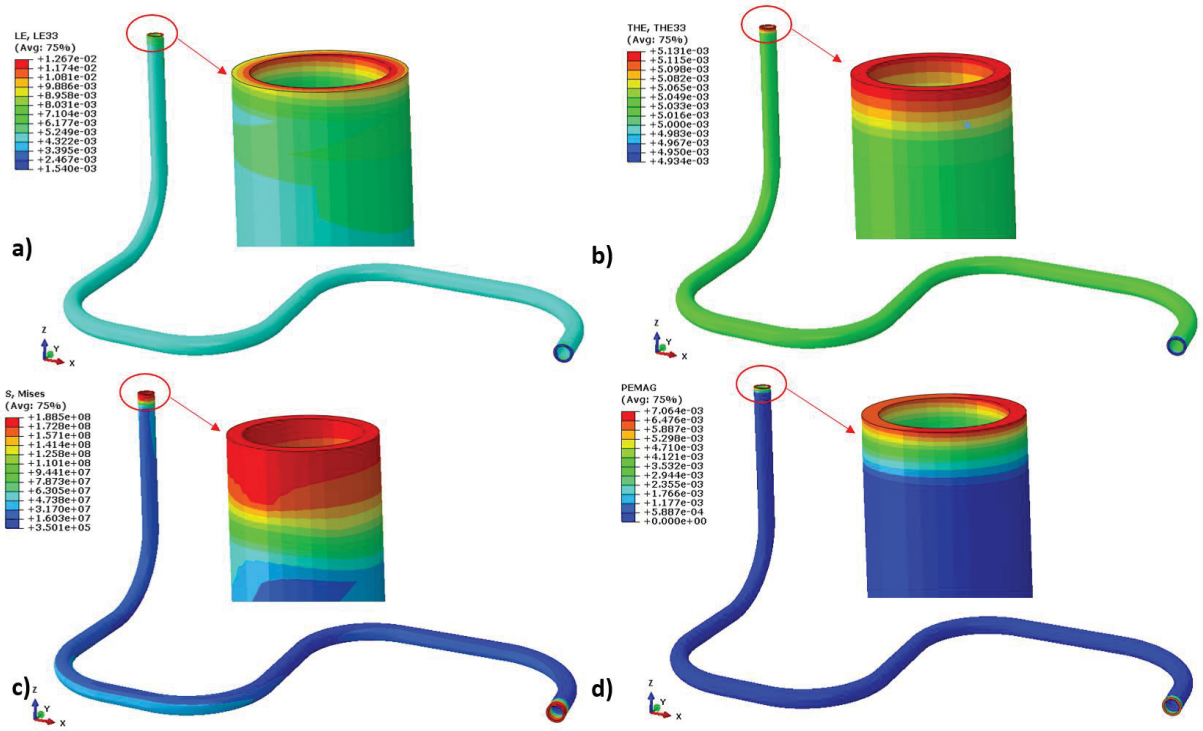

Figure 2. 15 Contour plots at 20 hr with pressurizer temperature of 344 ^{o}C and HL temperature of 326.4 ^{o}C: (a) vertical-direction (LE33) total strain, (b) vertical-direction (THE33) thermal strain, (c) Von Mises stress, and (d) effective plastic strain (PEMAG). The elastic-plastic FE simulation was conducted for case 1.

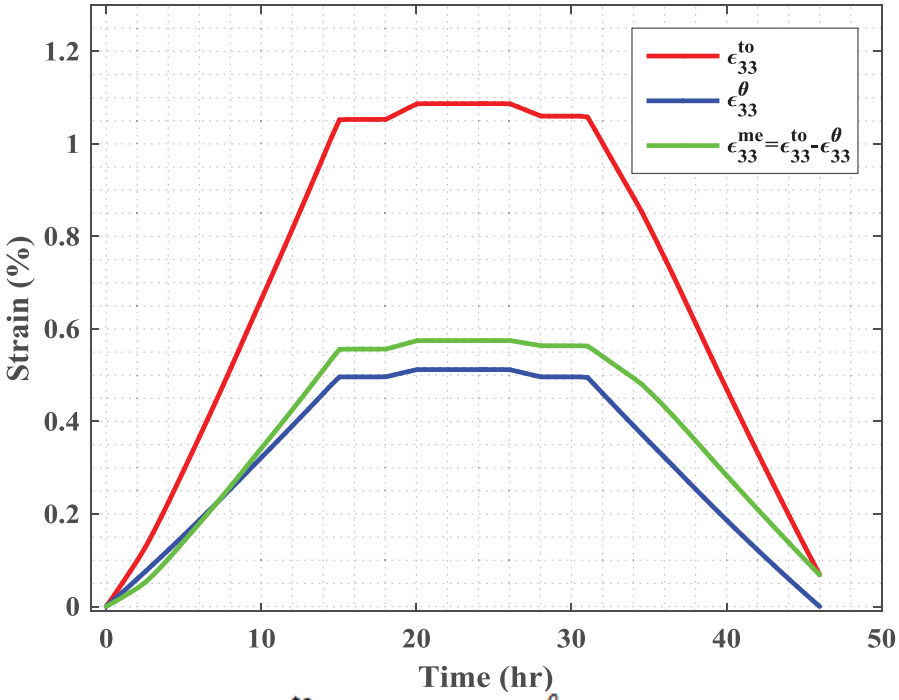

Figure 2. 16 Time-dependent total strain (ϵ_{33}^{to}), thermal strain (ϵ_{33}^{θ}), and the corresponding mechanical strain (ϵ_{33}^{me}) along the vertical direction at the centroid of a typical element near pressurizer end. The elastic-plastic FE simulation was conducted for case 1.

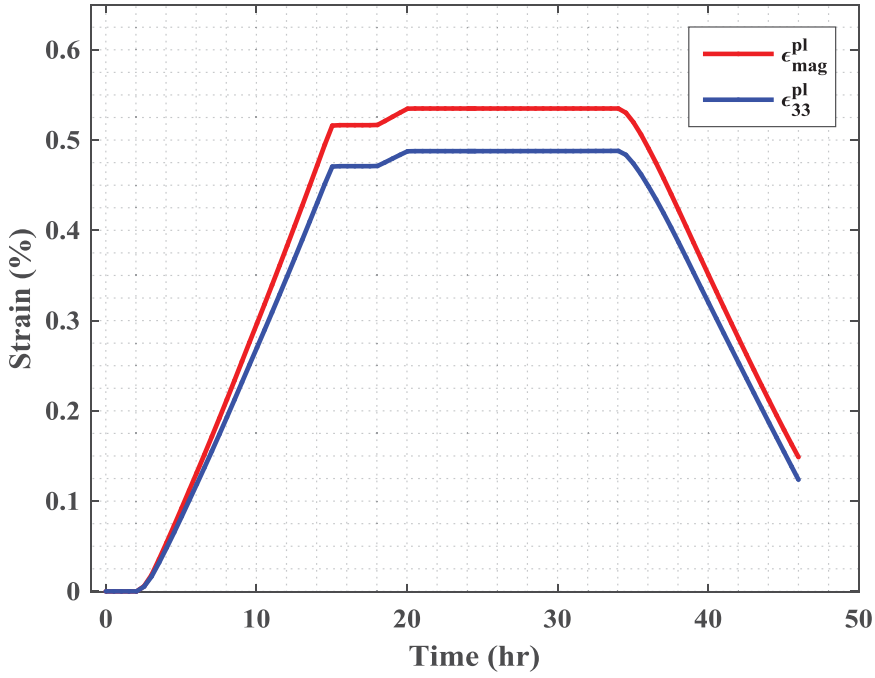

Figure 2. 17 Time-dependent equivalent plastic strain magnitude (ϵ_{mag}^{pl}) and plastic strain component along the vertical direction (ϵ_{33}^{pl}) at the centroid of a typical element near pressurizer end. The elastic-plastic FE simulation was conducted for case 1.

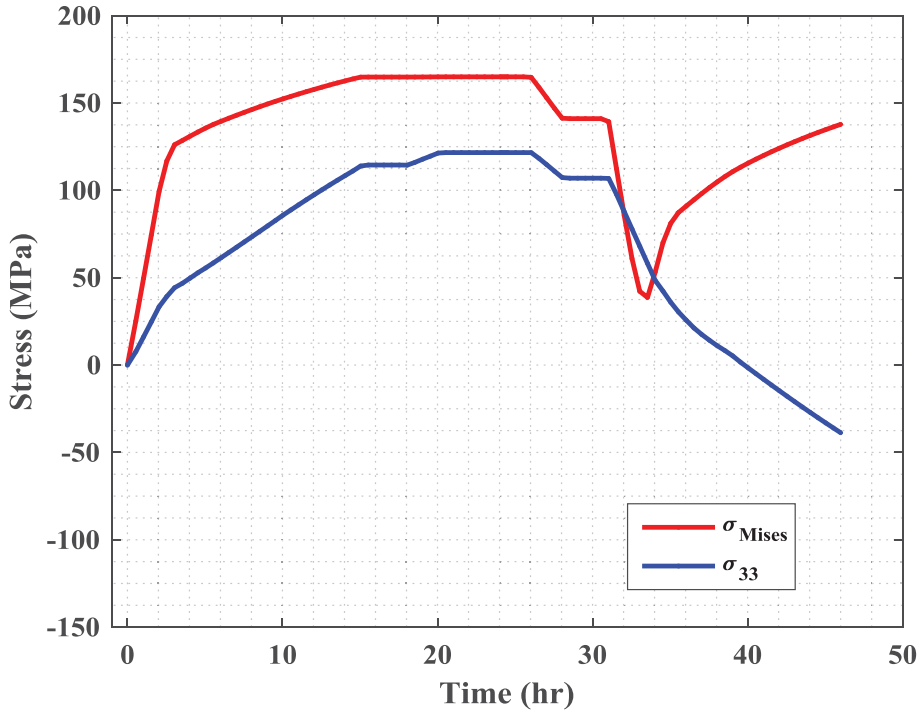

Figure 2. 18 Time-dependent equivalent stress or Von Mises stress (σ_{Mises}) and stress component along the vertical direction (σ_{33}) at the centroid of a typical element near pressurizer end. The elastic-plastic FE simulation was conducted for case 1.

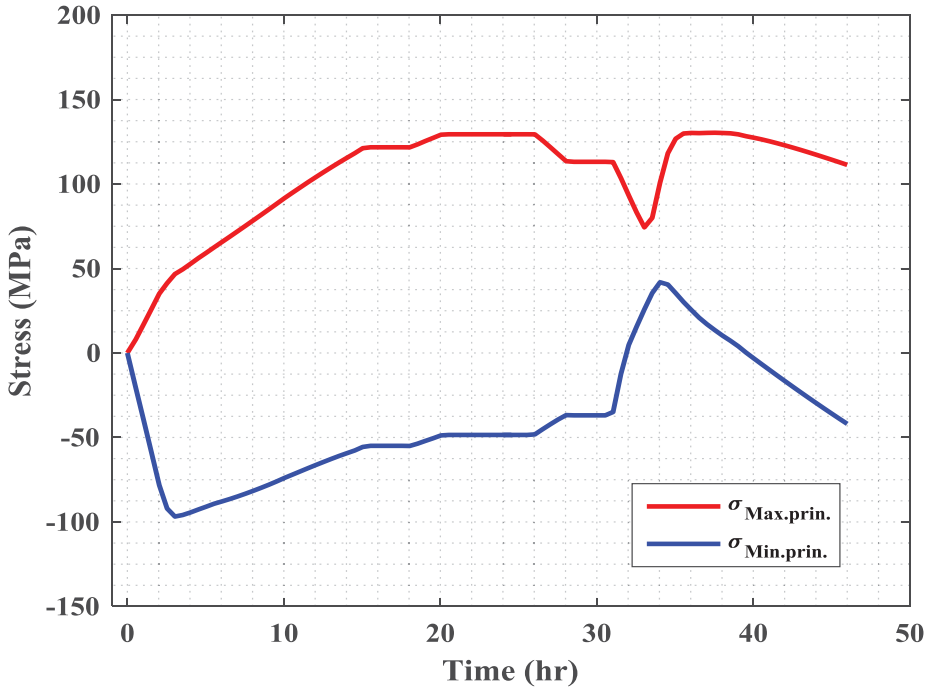

Figure 2. 19 Time-dependent maximum principal stress ($\sigma_{Max.\ prin}$) and minimum principal stress ($\sigma_{Min.\ prin}$) at the centroid of a typical element near pressurizer end. The elastic-plastic FE simulation was conducted for case 1.

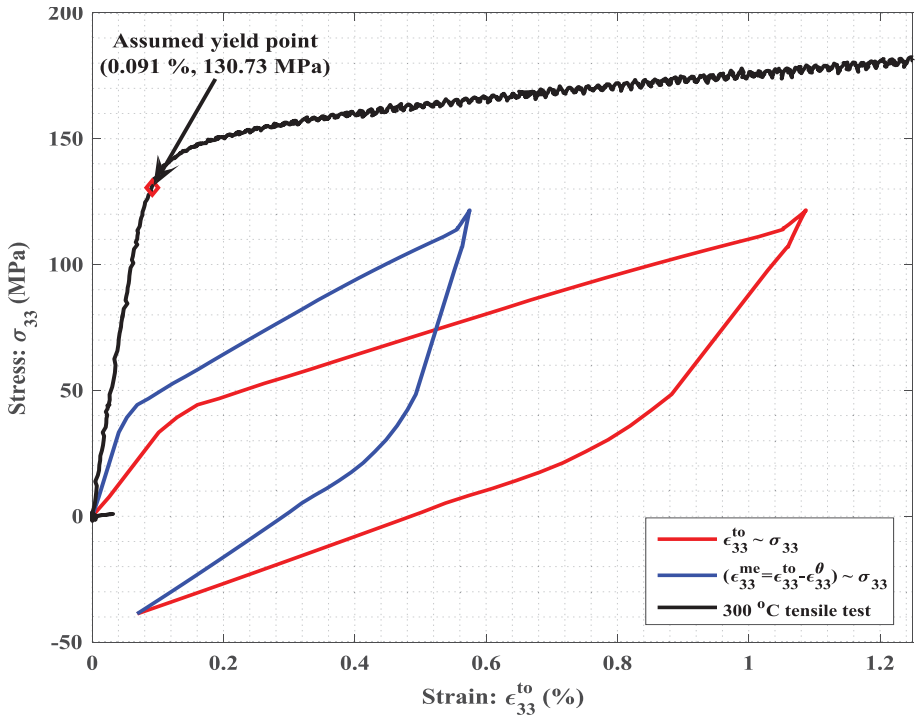

Figure 2. 20 Hysteresis curves ($\epsilon_{33}^{to} \sim \sigma_{33}$ and $\epsilon_{33}^{me} \sim \sigma_{33}$) at the centroid of a typical element near pressurizer end and comparison with respect to tensile test strain~stress curve at 300 °C. The elastic-plastic FE simulation was conducted for case 1.

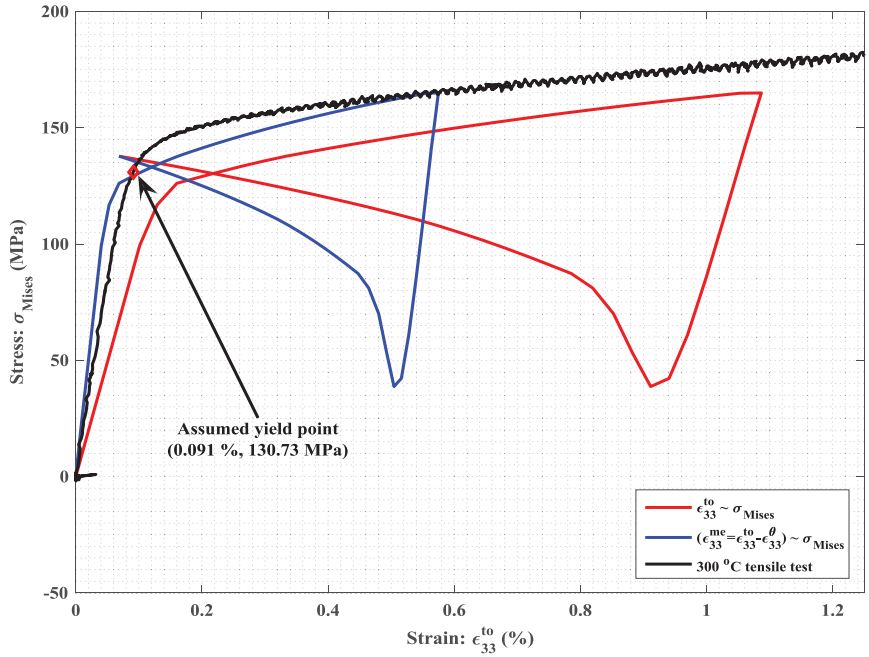

Figure 2. 21 Hysteresis curves ($\epsilon_{33}^{to} \sim \sigma_{Mises}$ and $\epsilon_{33}^{me} \sim \sigma_{Mises}$) at the centroid of a typical element near pressurizer end and comparison with respect to tensile test strain~stress curve at 300 °C. The elastic-plastic FE simulation was conducted for case 1.

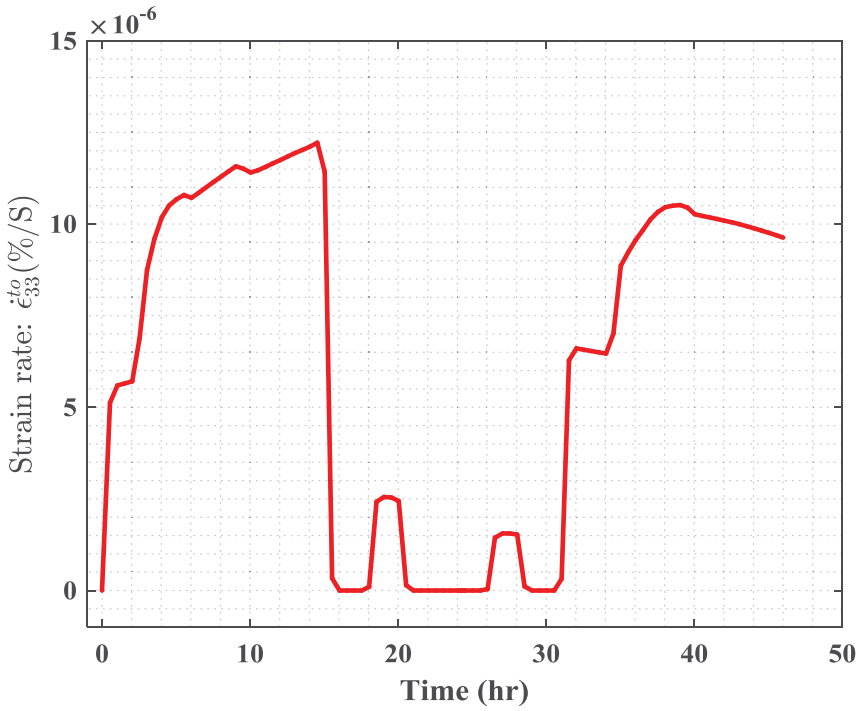

Figure 2. 22 Estimated total strain rates (along the vertical direction) at the centroid of a typical element near pressurizer end. The elastic-plastic FE simulation was conducted for case 1.

2.2.2 Structural analysis of SL pipe subjected to case 2: detailed design-basis loading cycle

Structural analyses were performed with the nodal temperature estimated through HT analysis of the SL pipe subjected to the detailed design-basis loading cycle shown in Figure 2.3. The stress analyses were performed by assuming elastic and elastic-plastic material properties. The associated results are presented below.

2.2.2.1 Elastic analysis results under case 2

Elastic FE analysis was performed for the detailed design-basis loading cycle. Figure 2.23 shows the contour plots at 1.975 days, that is, when the pressurizer and HL temperatures were 347.3 °C and 326.4 °C, respectively. Figure 2.24 shows the time-dependent total strain (ϵ_{33}^{to}), thermal strain (ϵ_{33}^{θ}), and the corresponding mechanical strain (ϵ_{33}^{me}) at the centroid of a typical element near the pressurizer end. Figure 2.25 shows the associated time-dependent equivalent stress or Von Mises stress (σ_{Mises}) and stress component along the vertical direction (σ_{33}). Figure 2.26 shows the corresponding time-dependent maximum principal stress ($\sigma_{Max.\ prin}$) and minimum principal stress ($\sigma_{Min.\ prin}$). Figure 2.27 shows the hysteresis curves ($\epsilon_{33}^{to} \sim \sigma_{33}$ and $\epsilon_{33}^{me} \sim \sigma_{33}$) and their comparison with the tensile test strain~stress curve for 300 °C. Figure 2.28 shows the hysteresis curves ($\epsilon_{33}^{to} \sim \sigma_{Mises}$ and $\epsilon_{33}^{me} \sim \sigma_{Mises}$) and their comparison with the tensile test strain~stress curve for 300 °C. Figure 2.29 shows the time-dependent total strain rates. Comparing Figures 2.23-2.29 with the corresponding results obtained with respect to case 1 (Figures 2.8-2.14) shows that the results are very similar, expect for a difference in time. However, note that the maximum mechanical strain component (0.4%) for case 2 is higher compared to the maximum mechanical strain component (0.35%) for case 1. This difference is possibly due to creation of higher

thermal strain (maximum value of 0.55%) in case 2 compared to the thermal strain created (maximum value of 0.5%) under case 1. This higher thermal strain in case 2 is due to the higher temperature differential (minimum and maximum temperatures of 26.67 ºC and 347.3 ºC, respectively) compared to that of case 1 (minimum and maximum temperature of 55 ºC and 344 ºC, respectively). Nevertheless, in both loading cases, the results look very similar qualitatively except for the difference associated with time.

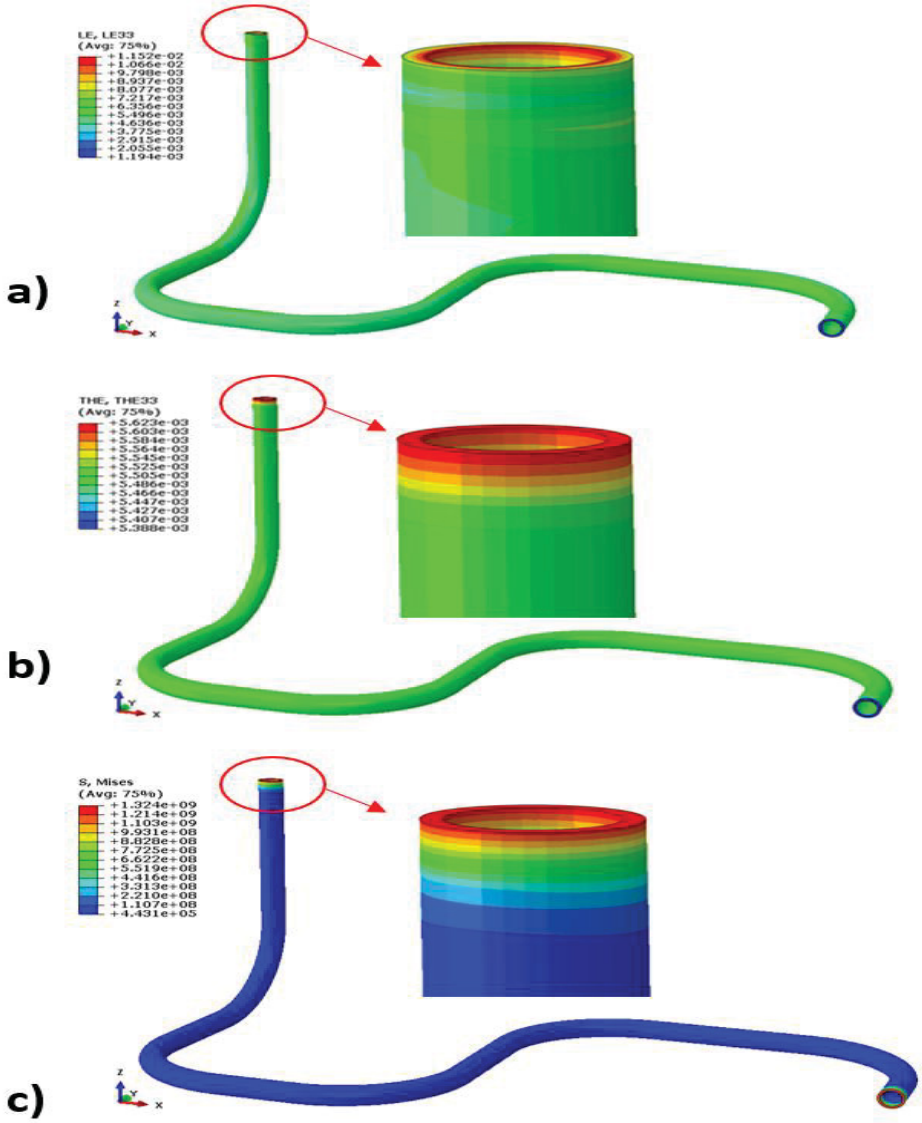

Figure 2. 23 Contour plots at 1.975 days with pressurizer temperature of 347.3 ºC and HL temperature of 326.4 ºC: (a) vertical-direction total strain, (b) vertical-direction thermal strain, and (c) Von Mises stress. The elastic FE simulation was conducted for case 2.

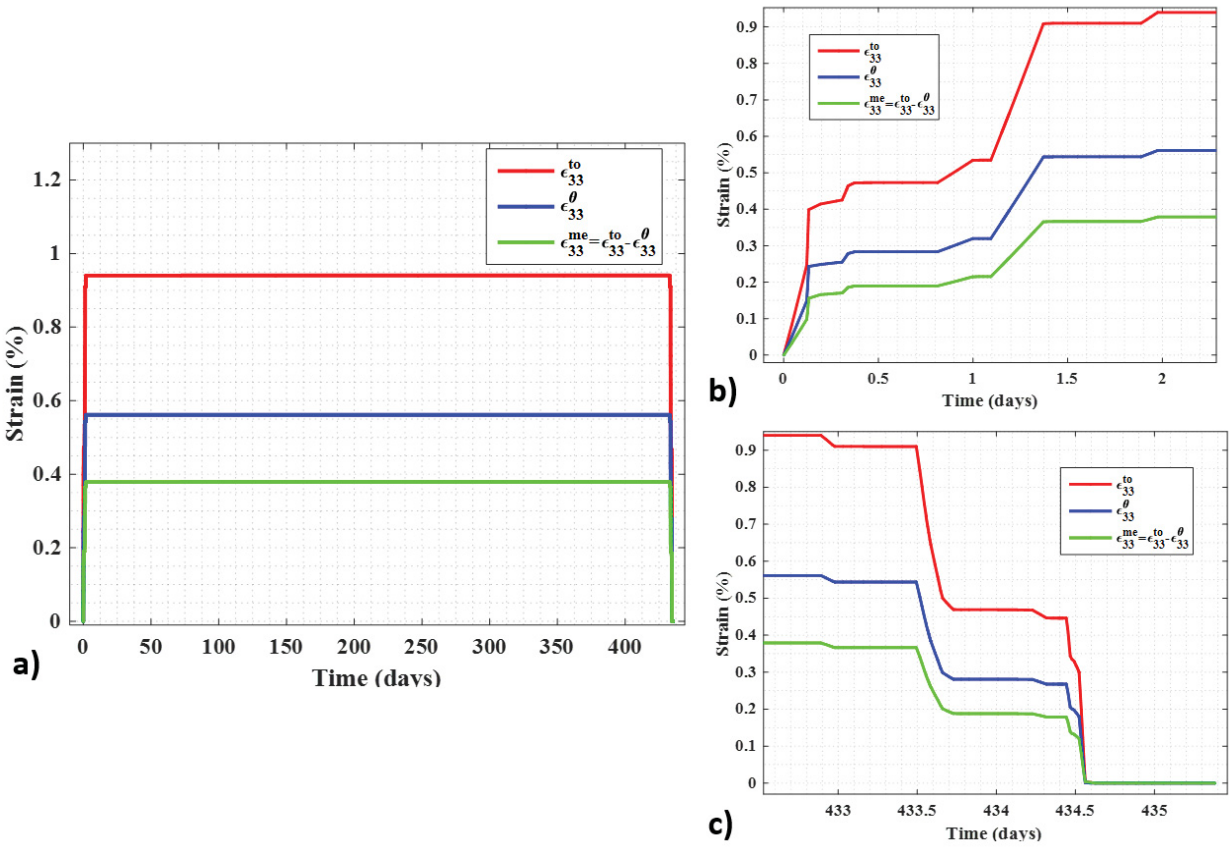

Figure 2. 24 Time-dependent total strain (ϵ_{33}^{to}), thermal strain (ϵ_{33}^{θ}), and the corresponding mechanical strain (ϵ_{33}^{me}) along the vertical direction at the centroid of a typical element near the pressurizer end. The elastic FE simulation was conducted for case 2 (a) under full cycle, (b) during heat-up, and (c) during cool-down.

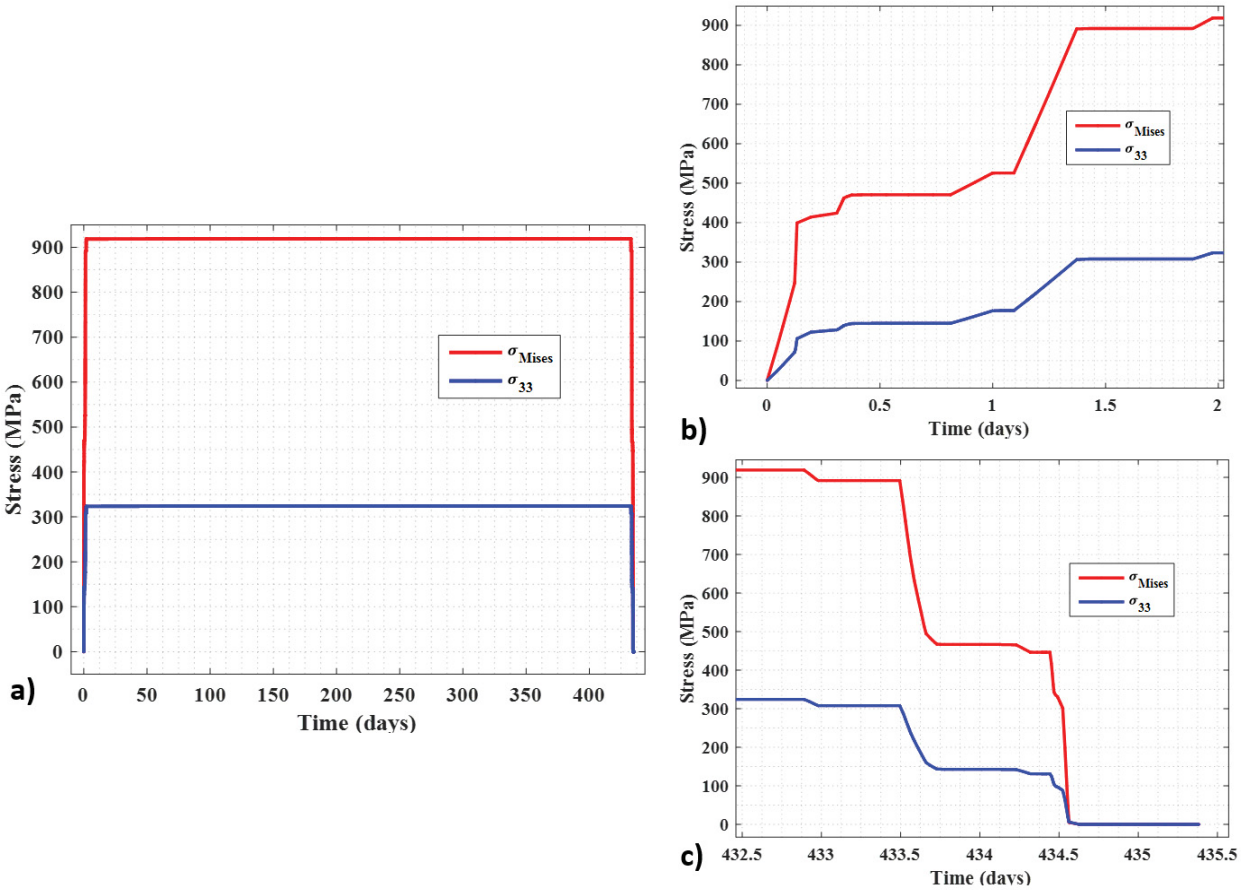

Figure 2. 25 Time-dependent equivalent stress or Von Mises stress (σ_{Mises}) and stress along the vertical direction (σ_{33}) at the centroid of a typical element near pressurizer end. The elastic FE simulation was conducted for case 2 (a) under full cycle, (b) during heat-up, and (c) during cool-down.

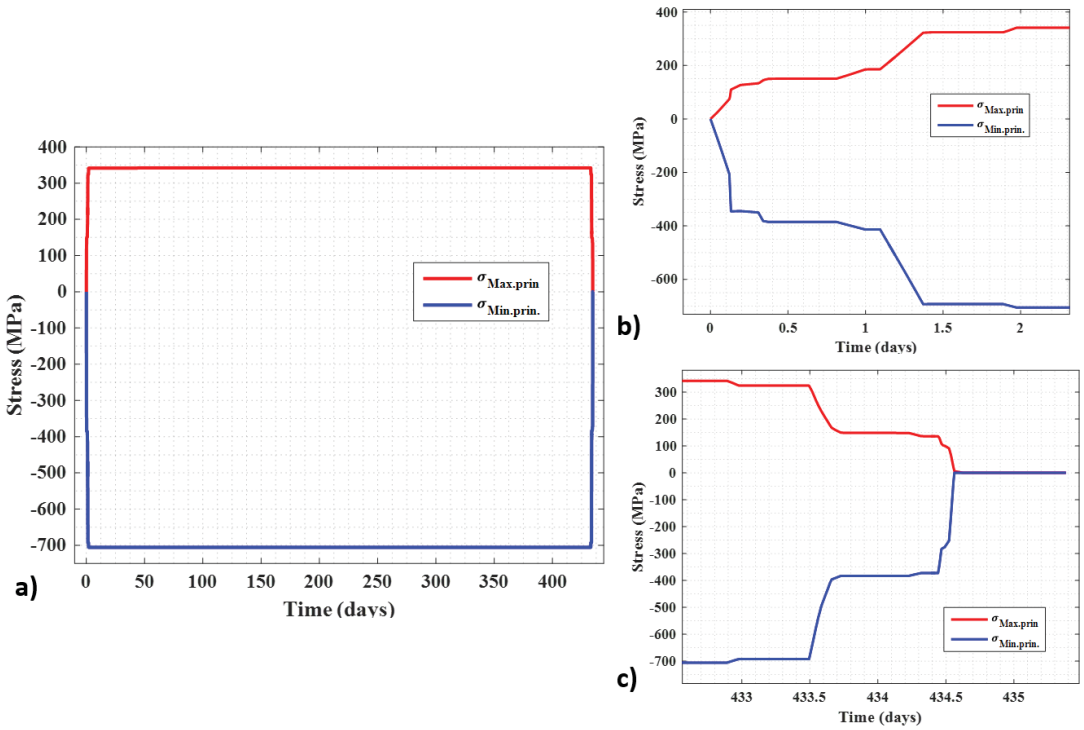

Figure 2. 26 Time-dependent maximum principal stress ($\sigma_{Max.\ prin}$) and minimum principal stress ($\sigma_{Min.\ prin}$) at the centroid of a typical element near pressurizer end. The elastic FE simulation was conducted for case 2 (a) under full cycle, (b) during heat-up, and (c) during cool-down.

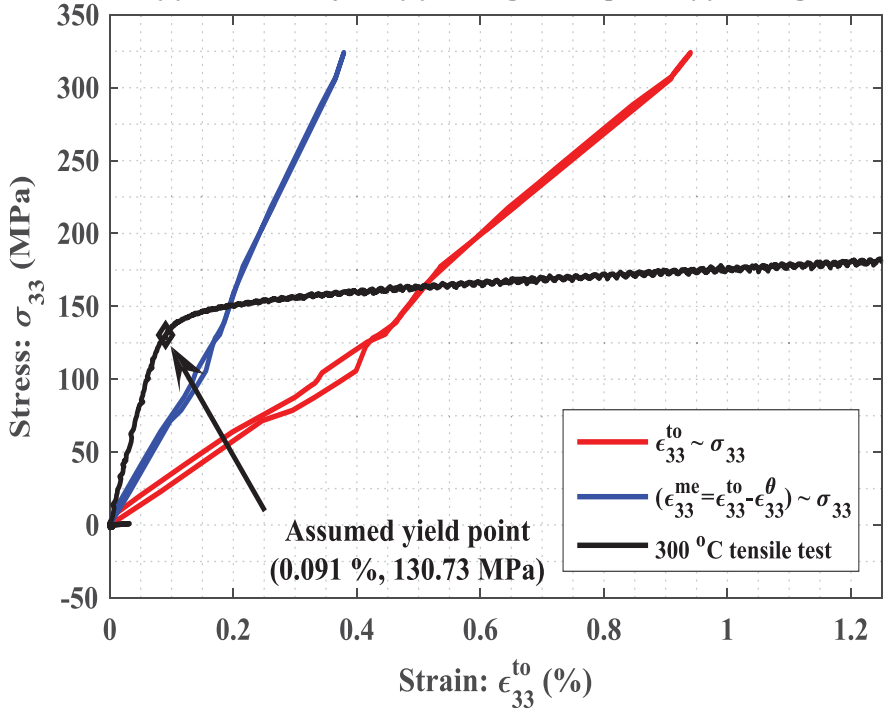

Figure 2. 27 Hysteresis curves ($\epsilon^{to}_{33} \sim \sigma_{33}$ and $\epsilon^{me}_{33} \sim \sigma_{33}$) at the centroid of a typical element near pressurizer end and comparison with respect to tensile test strain~stress curve for 300 °C. The elastic FE simulation was conducted for case 2.

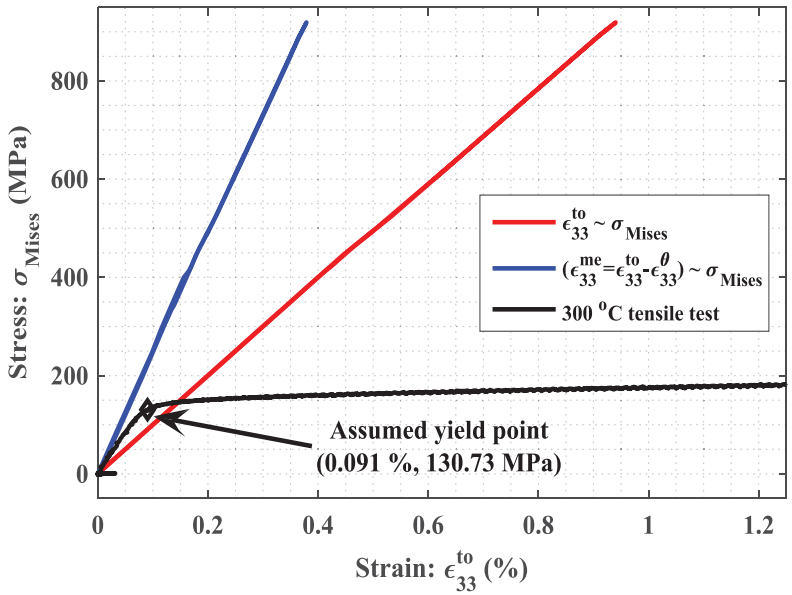

Figure 2. 28 Hysteresis curves ($\epsilon_{33}^{to} \sim \sigma_{Mises}$ and $\epsilon_{33}^{me} \sim \sigma_{Mises}$) at the centroid of a typical element near pressurizer end and comparison with respect to tensile test strain~stress curve at 300 °C. The elastic FE simulation was conducted for case 2.

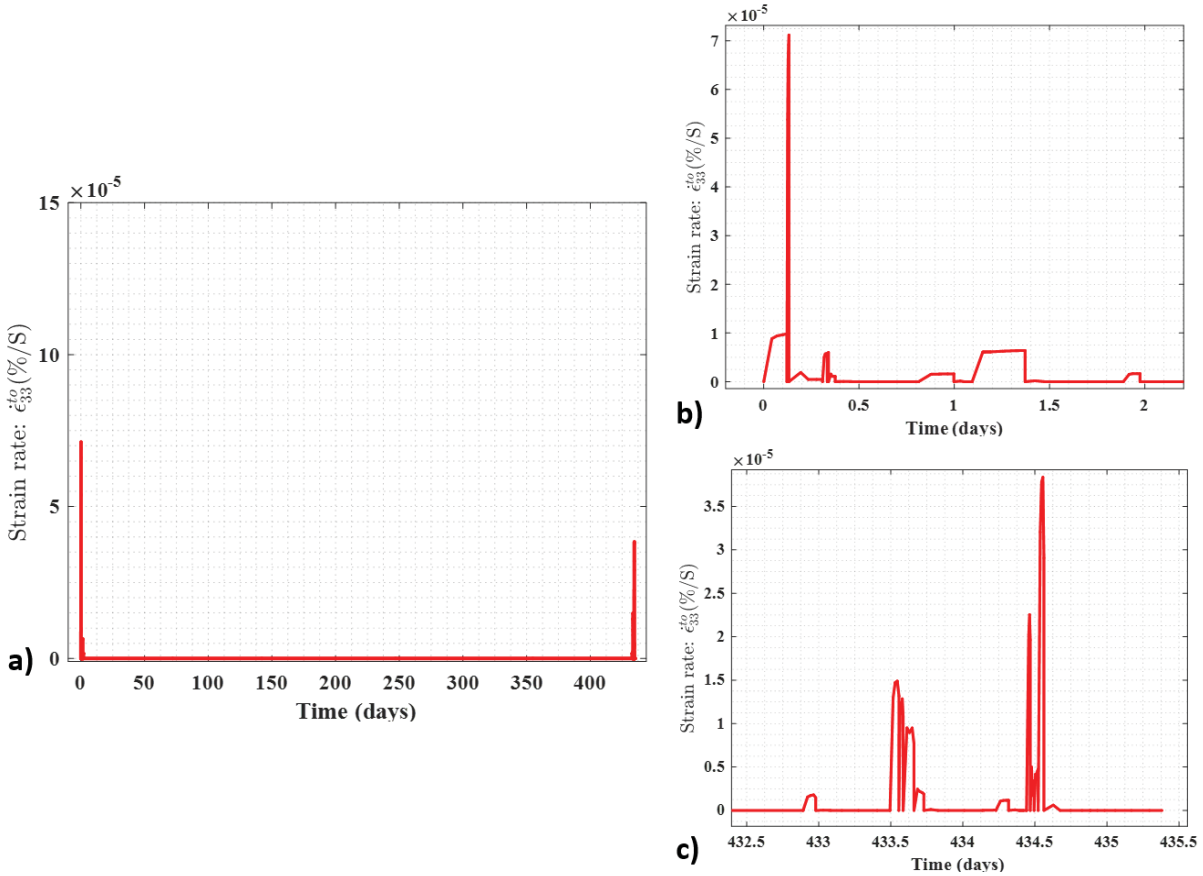

Figure 2. 29 Time-dependent total strain rates (along vertical direction) at the centroid of a typical element near pressurizer end. The elastic FE simulation was conducted for case 2 (a) under full cycle, (b) during heat-up, and (c) during cool-down.

2.2.2.2 Elastic-plastic analysis results under case 2

In addition to the above elastic analysis, an elastic-plastic analysis was performed for the detailed design-basis loading cycle. Figure 2.30 shows the corresponding contour plots at 1.975 days with pressurizer and HL temperatures of 347.3 ºC, and 326.4 ºC, respectively. Figure 2.31 shows the time-dependent total strain (ϵ_{33}^{to}), thermal strain (ϵ_{33}^{θ}), and the corresponding mechanical strain (ϵ_{33}^{me}) at the centroid of a typical element near the pressurizer end. Figure 2.32 shows the time-dependent equivalent plastic strain magnitude (ϵ_{mag}^{pl}) and plastic strain component along the vertical direction (ϵ_{33}^{pl}) at the centroid of a typical element near the pressurizer end. Figure 2.33 shows the time-dependent equivalent stress or Von Mises stress (σ_{Mises}) and stress component along the vertical direction (σ_{33}). Figure 2.34 shows the time-dependent maximum principal stress ($\sigma_{Max.\ prin}$) and minimum principal stress ($\sigma_{Min.\ prin}$). Figure 2.35 shows the hysteresis curves ($\epsilon_{33}^{to} \sim \sigma_{33}$ and $\epsilon_{33}^{me} \sim \sigma_{33}$) with respect to the σ_{33} component stress and their comparison with respect to the tensile test strain~stress curve for 300 ºC. Figure 2.36 shows the hysteresis curves ($\epsilon_{33}^{to} \sim \sigma_{Mises}$ and $\epsilon_{33}^{me} \sim \sigma_{Mises}$) with respect to the Von Mises stress σ_{Mises} and its comparison with respect to the tensile test strain~stress curve for 300 ºC. Figure 2.37 shows the time-dependent total strain rates (along the vertical direction).

These results (Figures 2.30-2.37) for case 2 are qualitatively very similar to the elastic-plastic analysis results (Figures 2.15-2.22) for case 1, except for the difference with respect to time. The other major difference is that the estimated mechanical strain for case 2 is higher than that of the mechanical strain estimated for case 1. For example, the maximum mechanical strain in case 2 is 0.65%, whereas the corresponding maximum mechanical strain in case 1 is 0.575%. As discussed before for the elastic stress analysis under case 2, the higher mechanical strain in case 2 is due to its higher temperature differential compared with case 1. Overall, these results illustrate the importance of knowing the prototypical loading profile that actually acts on a specific component. Fatigue life can be substantially different if there is a substantial change in strain amplitude. The related experimental results are discussed in the next section.

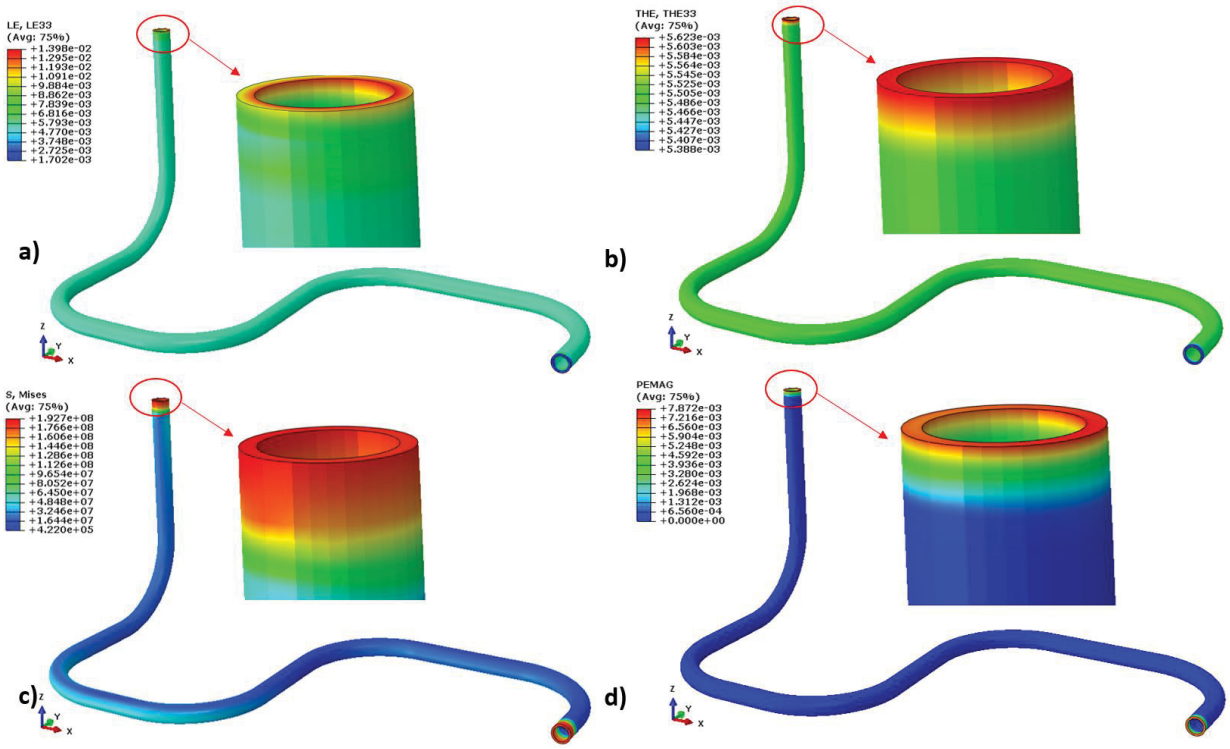

Figure 2. 30 Contour plots at 1.975 days with pressurizer temperature of 347.3 °C and HL temperature of 326.4 °C: (a) vertical-direction (LE33) total strain, (b) vertical-direction (THE33) thermal strain, (c) Von Mises stress, and (d) effective plastic strain (PEMAG). The elastic-plastic FE simulation was conducted for case 2.

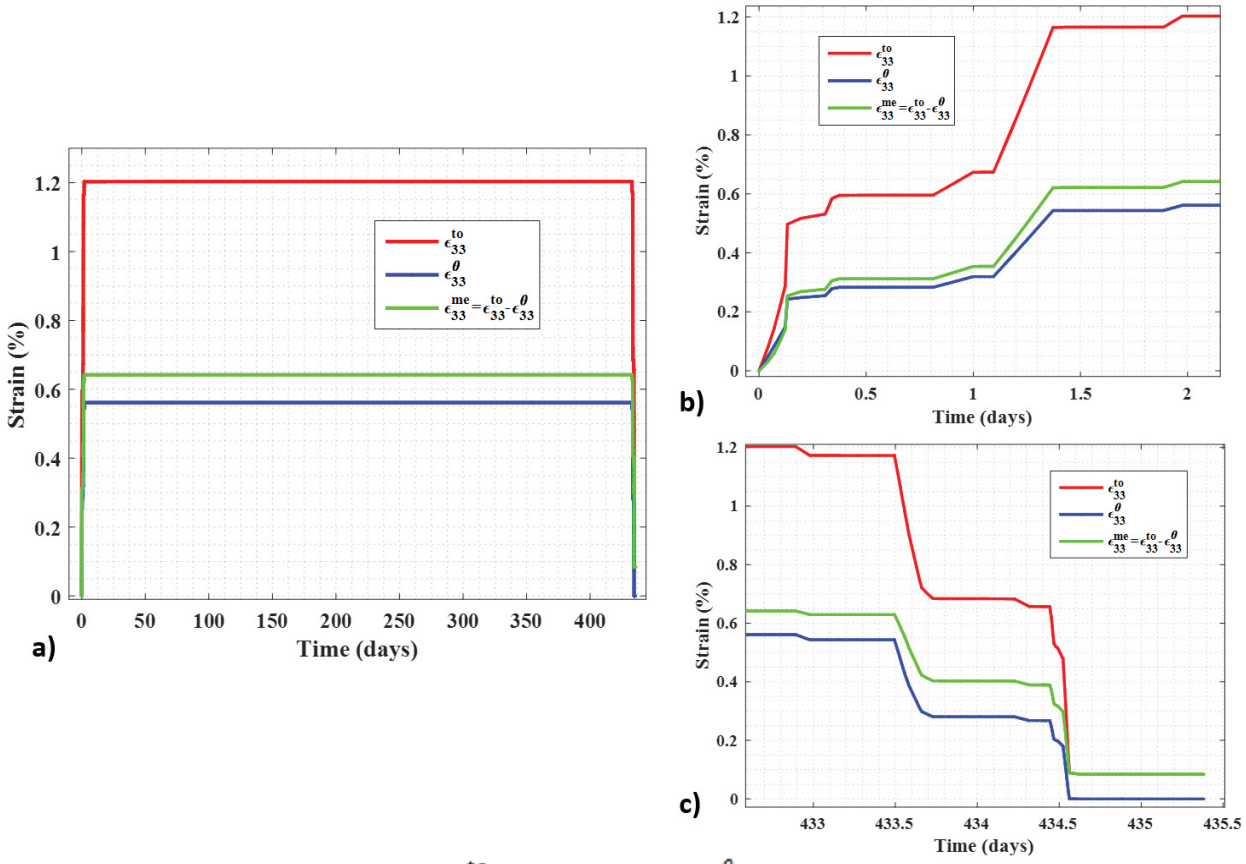

Figure 2. 31 Time-dependent total strain (ϵ_{33}^{to}), thermal strain (ϵ_{33}^{θ}), and the corresponding mechanical strain (ϵ_{33}^{me}) along the vertical direction at the centroid of a typical element near pressurizer end. The elastic-plastic FE simulation was conducted for case 2 (a) under full cycle, (b) during heat-up, and (c) during cool-down.

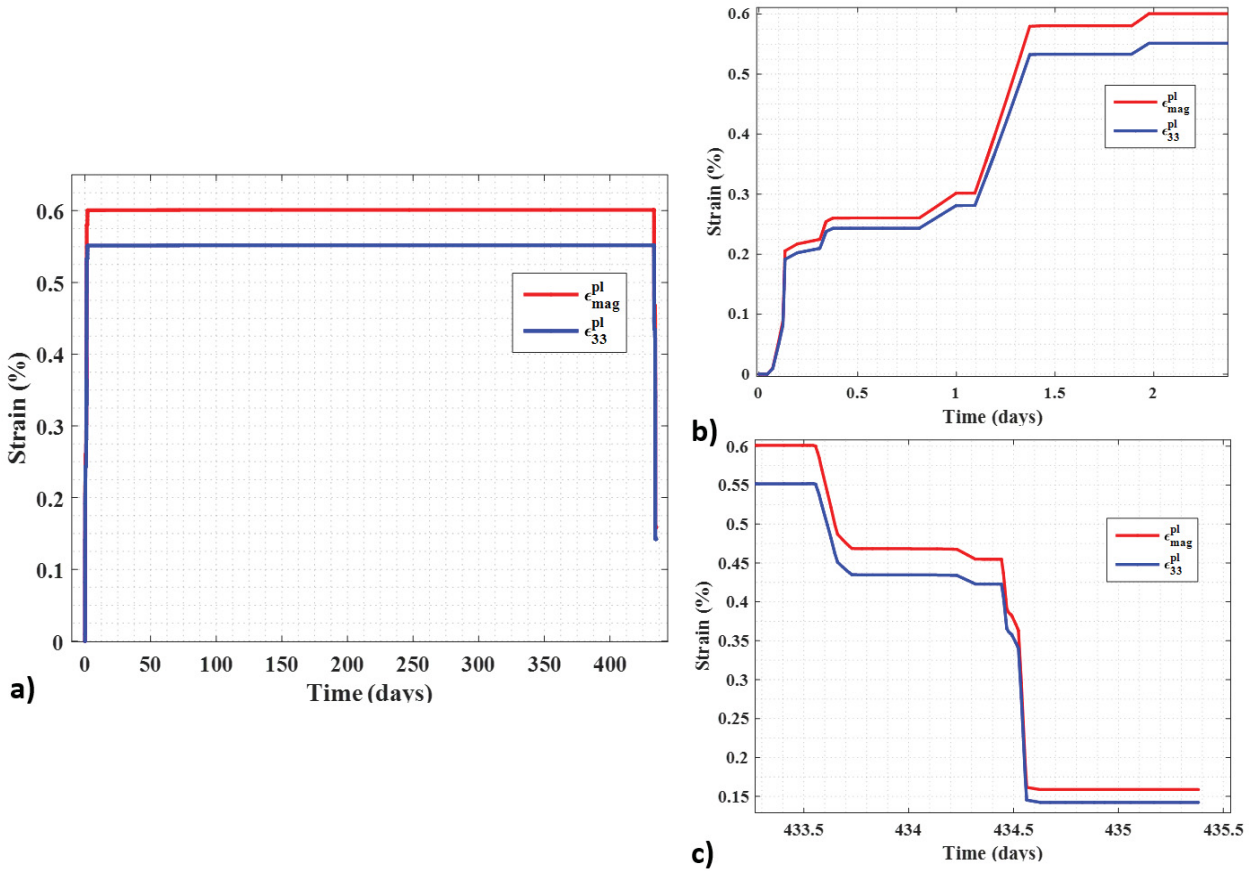

Figure 2. 32 Time-dependent equivalent plastic strain magnitude (ϵ^{pl}_{mag}) and plastic strain component along the vertical direction (ϵ^{pl}_{33}) at the centroid of a typical element near pressurizer end. The elastic-plastic FE simulation was conducted for case 2 (a) under full cycle, (b) during heat-up, and (c) during cool-down.

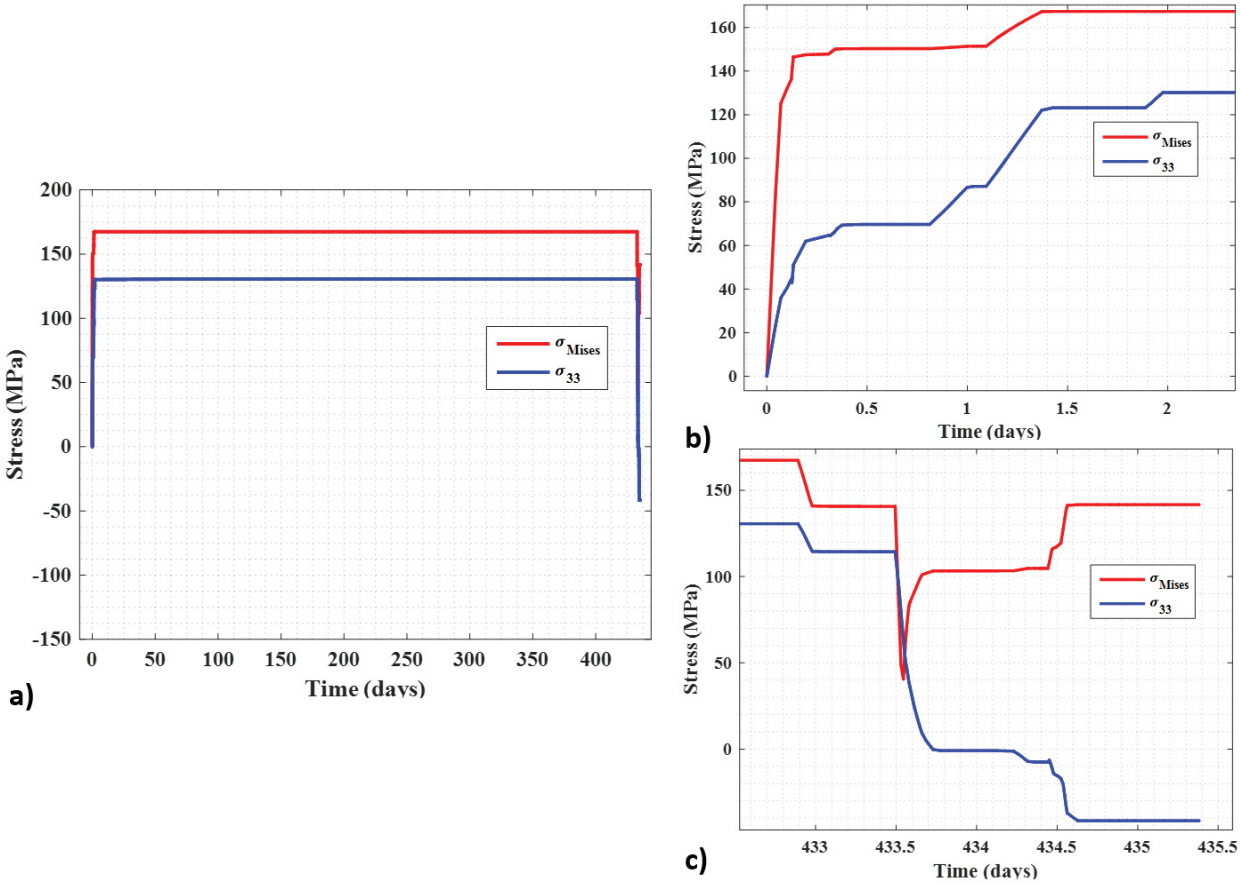

Figure 2. 33 Time-dependent equivalent stress or Von Mises stress (σ_{Mises}) and stress component along the vertical direction (σ_{33}) at the centroid of a typical element near pressurizer end. The elastic-plastic FE simulation was conducted for case 2 (a) under full cycle, (b) during heat-up, and (c) during cool-down.

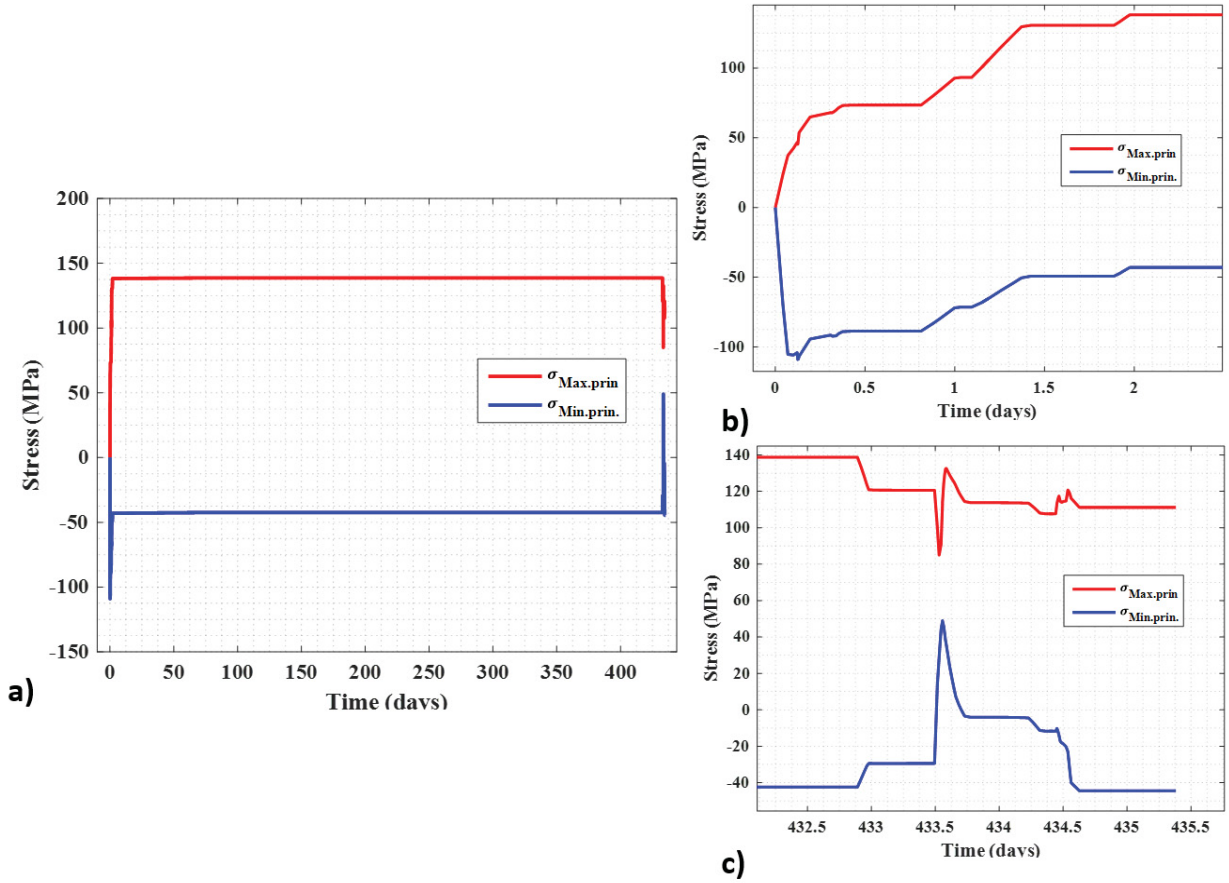

Figure 2. 34 Time-dependent maximum principal stress ($\sigma_{Max.\ prin}$) and minimum principal stress ($\sigma_{Min.\ prin}$) at the centroid of a typical element near pressurizer end. The elastic-plastic FE simulation was conducted for case 2 (a) under full cycle, (b) during heat-up, and (c) during cool-down.

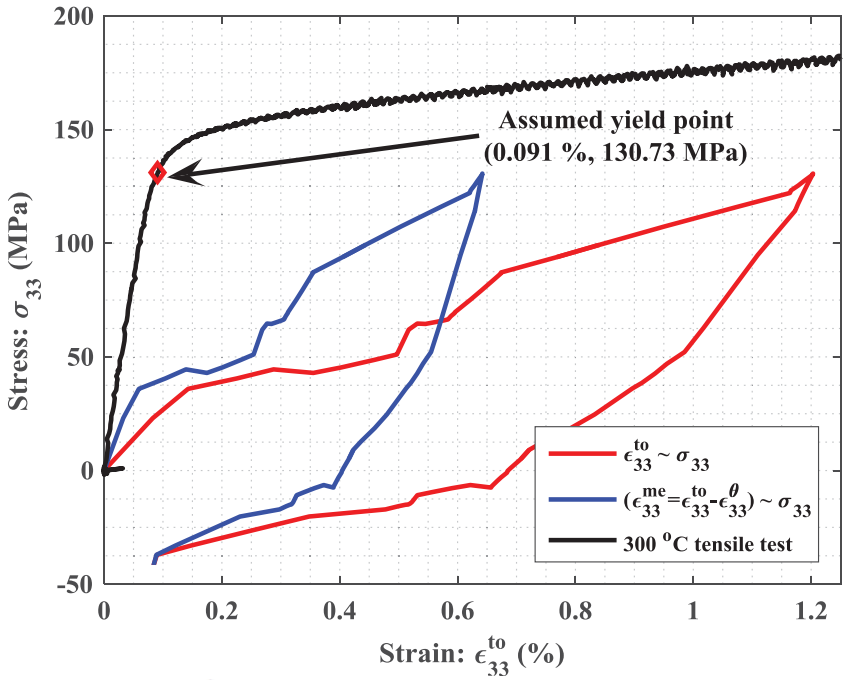

Figure 2. 35 Hysteresis curves ($\epsilon_{33}^{to} \sim \sigma_{33}$ and $\epsilon_{33}^{me} \sim \sigma_{33}$) at the centroid of a typical element near pressurizer end and comparison with tensile test strain~stress curve for 300 °C. The elastic-plastic FE simulation was conducted for case 2 (a) under full cycle, (b) during heat-up, and (c) during cool-down.

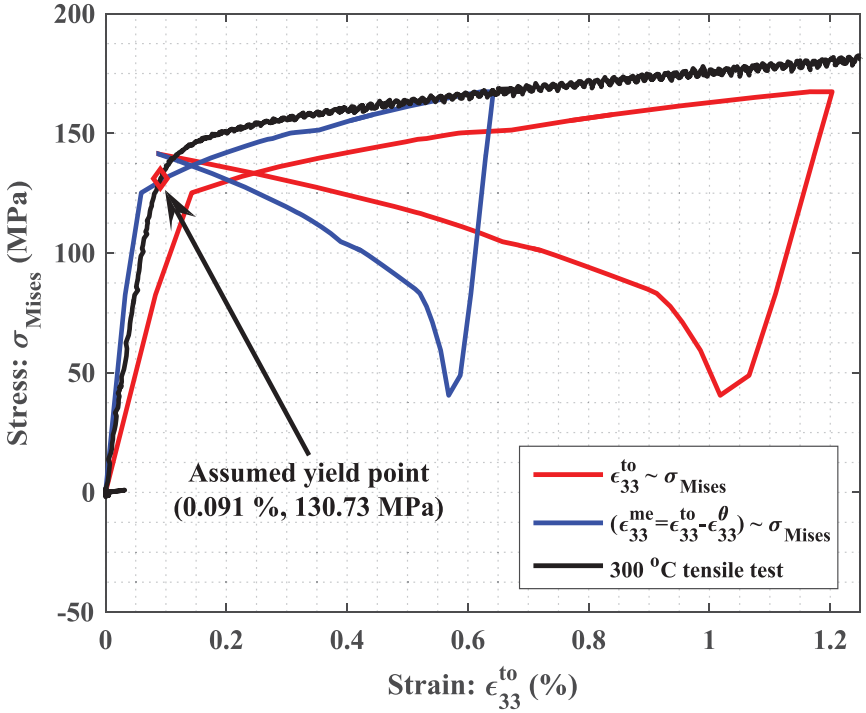

Figure 2. 36 Hysteresis curves ($\epsilon_{33}^{to} \sim \sigma_{Mises}$ and $\epsilon_{33}^{me} \sim \sigma_{Mises}$) at the centroid of a typical element near pressurizer end and comparison with tensile test strain~stress curve for 300 °C. The elastic-plastic FE simulation was conducted for case 2 (a) under full cycle, (b) during heat-up, and (c) during cool-down.

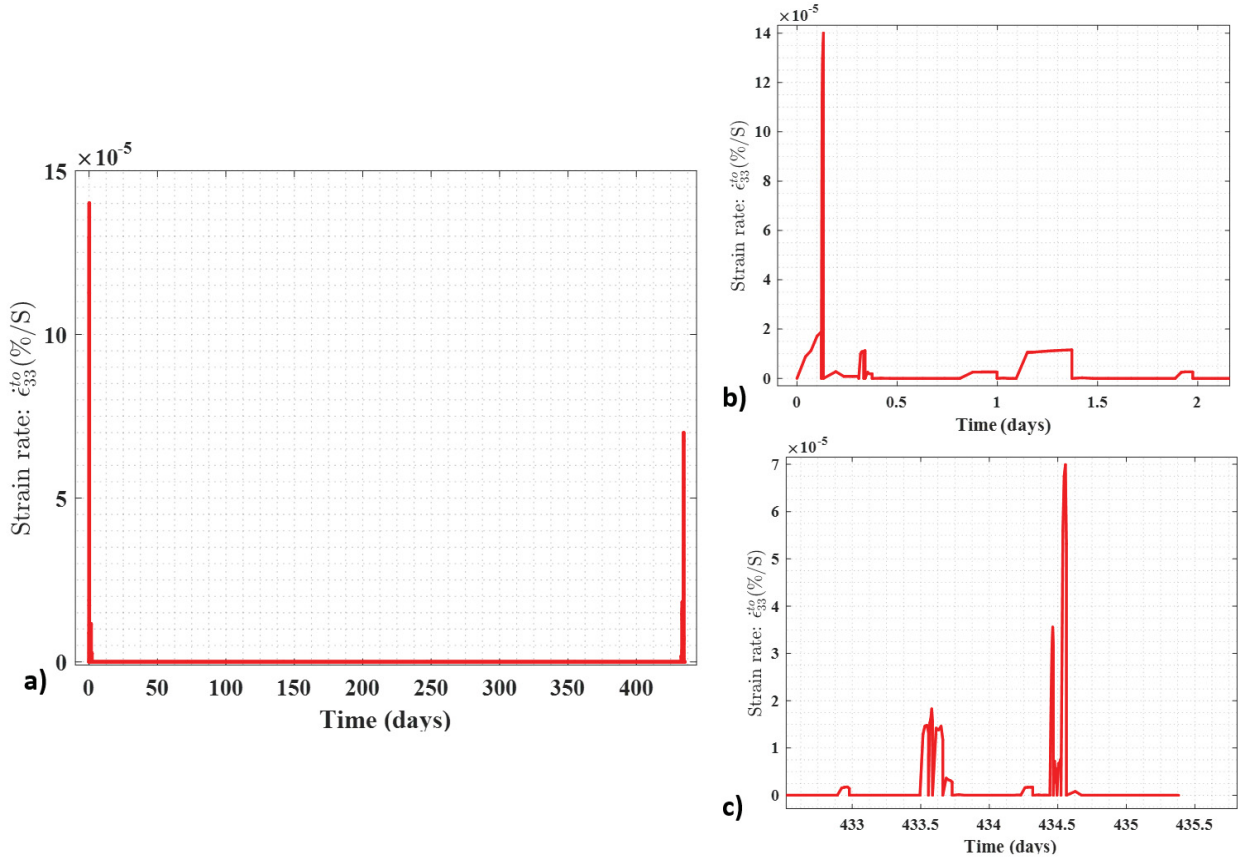

Figure 2. 37 Time-dependent total strain rates (along the vertical direction) at the centroid of a typical element near pressurizer end. The elastic-plastic FE simulation was conducted for case 2 (a) under full cycle, (b) during heat-up, and (c) during cool-down.

3 Fatigue Experiment Results

In the previous section, we presented FE model results for 316 SS SL pipe under two loading conditions (cases 1 and 2). These results were presented for a single cycle. However, mechanistic fatigue evaluations require an understanding of the multi-cycle stress-strain evolution of material under the loading cycles. This knowledge is gained through both experimental fatigue testing and computational modeling. Fatigue testing of real reactor components with realistic loading is nearly impossible to conduct because of its complexity and associated high cost and time requirements. However, it is possible to perform fatigue testing of small laboratory specimens, which can be subjected to a similar loading profile as a real reactor component at a much lower cost and in a shorter period. The fatigue test can be performed with a conventional uniaxial specimen subjected to loading input (either stress or strain), which has to be estimated from multiaxial FE models of real components. Although multiaxial behavior of material stress-strain evolution cannot be predicted fully through a simplistic uniaxial fatigue test, this is the best possible way to avoid the high cost and time requirements for multiaxial testing. In this section, we present uniaxial fatigue test results conducted with the strain profile estimated based on the FE models discussed in Section 2. The corresponding multi-cycle FE modeling results of uniaxial specimens are discussed in Section 5. Both the uniaxial fatigue experiment and modeling are performed under in-air conditions at isothermal temperature of 300 ^{o}C. We used the mechanical strain (total strain minus thermal strain) as input strain with the assumption that it will not be affected by temperature. In addition, the time axis of the FE simulated results for cases 1 and 2 cover a very long period, and it may not be possible to use the same time scale to conduct the fatigue tests. Hence, before using the FE simulated strain profile in the fatigue tests, we scaled the FE simulated strain profiles to finish the fatigue tests in a reasonable time. We used the elastic-plastic FE simulated mechanical strain history (time vs. ϵ_{33}^{me}) shown in Figures 2.16 and 2.31 for generating the strain inputs for case 1 (simplified loading cycle) and case 2 (detailed loading cycle) fatigue tests, respectively. We scaled the time axis of the mechanical strain (ϵ_{33}^{me}) such that the strain rise (during heat-up) and strain drop (during cool-down) follow a fixed strain rate of 0.1%/s. This rate is consistent with our tensile and fatigue test material models, which are primarily based on tensile/fatigue test data for 0.1%/s. In addition, during steady-state full power operation and during any other steady-state or hold conditions (e.g., during heat-up and cool-down), the time axis of the FE estimated strain profile (Figures 2.16 and 2.31) was substantially truncated to conduct the test in a reasonable time. Furthermore, due to the complexity in applying the strain input with a non-zero end point, the fatigue test input profiles are designed such that the strain goes to the zero set point at the end of each cycle. Note that the FE model results for mechanical strain history (Figures 2.16 and 2.31) show that the mechanical strain does not drop to its starting value due to the accumulated plastic strain. However, for a strain-controlled fatigue test, the strain profiles are not known beforehand beyond the first cycle. Allowing the strain to be consistent with the FE model results requires conducting stress-controlled fatigue tests. These tests are highly complex to conduct due to the asymptotic behavior of 316 SS in the stress-strain curves and the associated chances of buckling with small perturbation in stress input. Hence, for simplicity, we selected the strain-controlled testing approach to start with. Stress-controlled fatigue testing can be completed in future work, depending on the resources and time available.

The two fatigue experiments conducted based on the above strain profiles are as follows:

a) ET-F47: 316 SS strain-controlled fatigue specimen, 300 ^{o}C, in-air condition with strain rate of 0.1 %/s and Case 1 (simplified design-basis loading cycle).

b) ET-F48: 316 SS strain-controlled fatigue specimen, 300 ^{o}C, in-air condition with strain rate of 0.1 %/s, and Case 2 (detailed design-basis loading cycle).

The strain profiles (coded to INSTRON™ test frame controller) and the associated experimental results for the two loading cases are presented below.

3.1 ET-F47 Fatigue Test Subjected to Case 1

The strain profile for the ET-F47 fatigue test is shown in Figure 3.1, which has a truncated time period of 20 s. As shown in the figure, unlike the conventional fatigue tests with symmetric strain input (that is, zero-baseline and equal amplitude in both tension and compression), the strain input for ET-F47 has an asymmetric (non-zero baseline and only tensile strain loading) strain profile. This condition may create different test results compared to the symmetric input fatigue test. Figure 3.2 shows the ET-F47 results observed for the stress history over the entire fatigue life. The associated fatigue life for the ET-F47 specimen is 24,800 cycles. Figure 3.3 shows the observed fatigue cycle versus maximum stress amplitudes for ET-F47. This figure shows that there is a first-stage primary hardening and then a second-stage secondary hardening. These two stages were not observed in our previous fatigue tests of 316 SS specimens subjected to symmetric and zero-baseline loading, although they were conducted under similar test conditions. Figure 3.4 shows the observed fatigue cycle versus maximum stress amplitudes in our earlier ET-F13 test [4]. The ET-F13 fatigue specimen was subjected to a symmetric (zero baseline) stroke loading (frame crosshead displacement), which is equivalent of applying a symmetric gauge area strain loading. This secondary hardening under more prototypical loading is worth noting. Observation of secondary loading under asymmetric loading may require further validation testing under similar loading profiles. Figure 3.5 shows the first 10 cycles of the hysteresis (input strain versus observed stress) curves for ET-F47. Figures 3.6 and 3.7 show the corresponding input strain history and observed stress history (first 10 fatigue cycles), respectively.

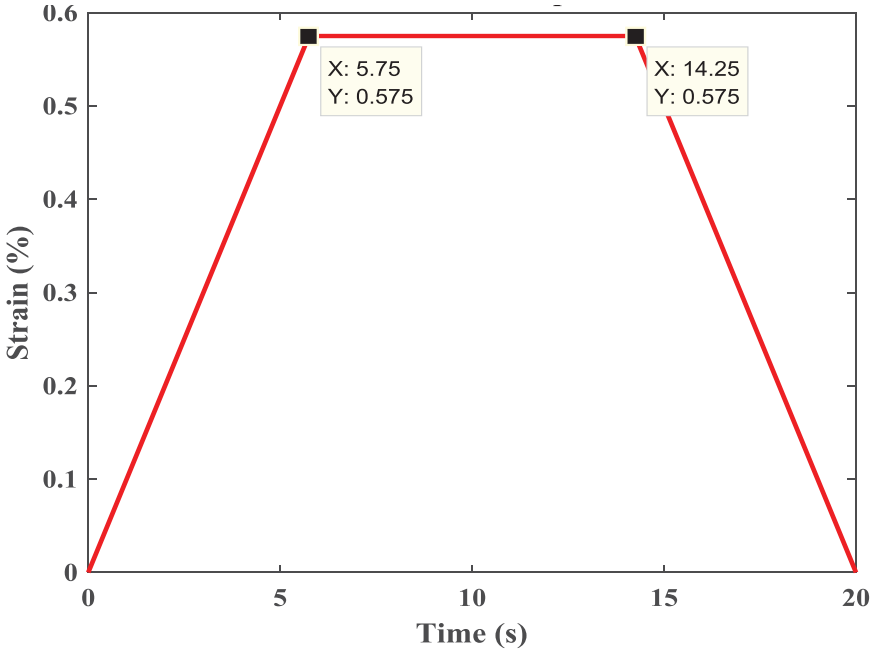

Figure 3. 1 ET-F47 input strain profile. The profile was estimated based on elastic-plastic FE model of PWR surge line pipe that was subjected to case 1

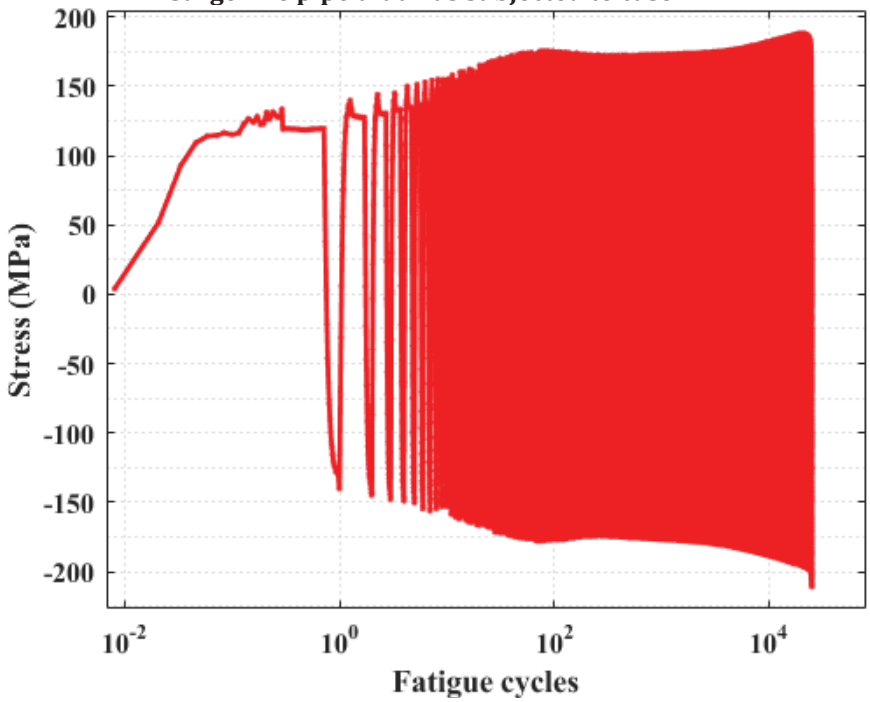

Figure 3. 2 Observed stress history from ET-F47 test. The fatigue specimen was subjected to asymmetric (with non-zero baseline) strain input obtained from FE model with case 1.

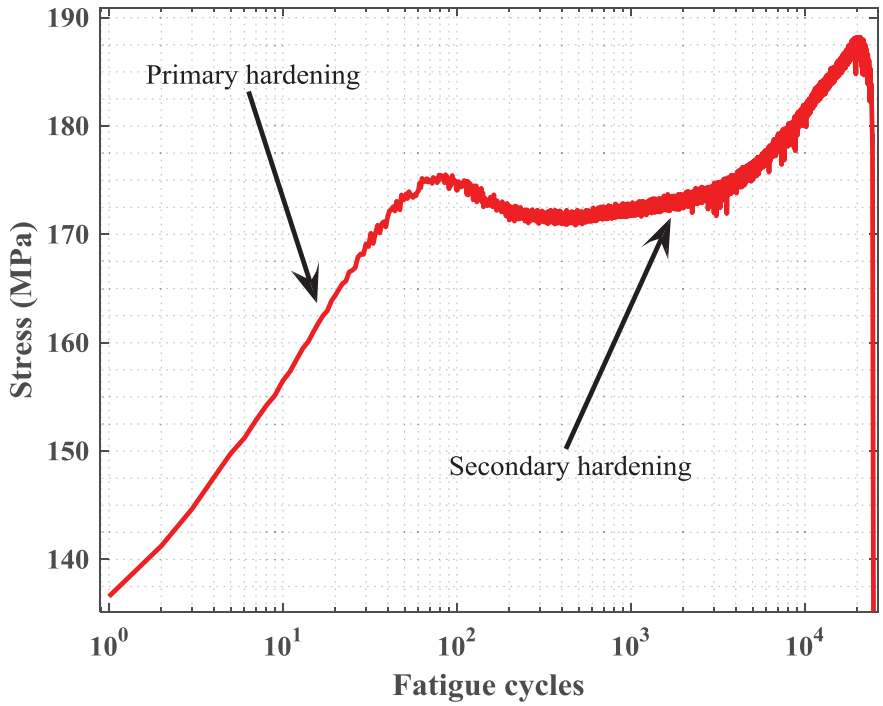

Figure 3. 3 Observed fatigue cycle versus maximum stress amplitudes for ET-F47 test. The fatigue specimen was subjected to asymmetric (with non-zero baseline) strain input obtained from FE model with case 1.

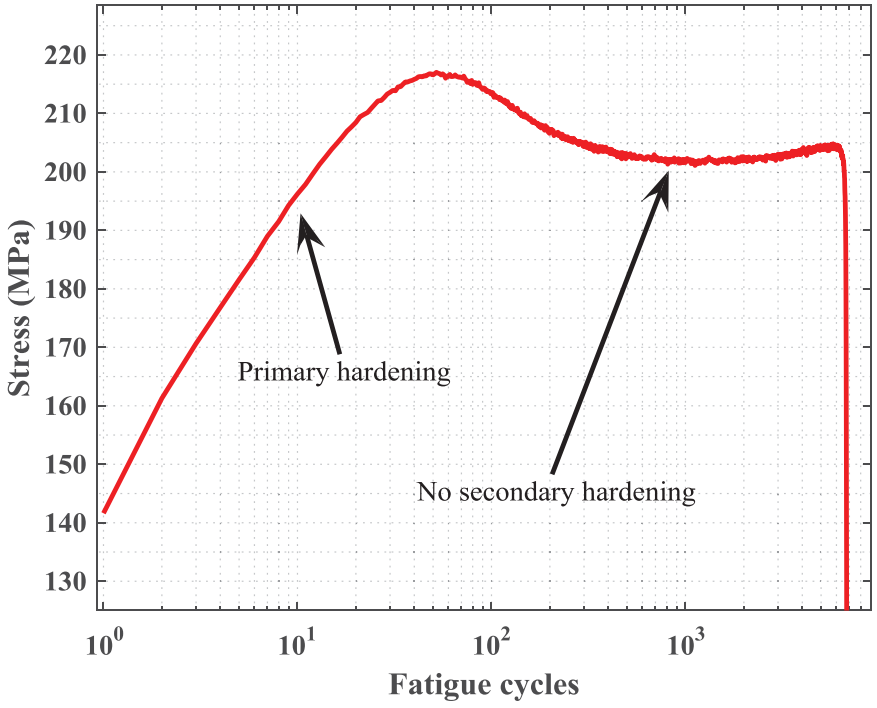

Figure 3. 4 Observed fatigue cycle versus maximum stress amplitudes in our earlier conducted ET-F13 test. The fatigue specimen was subjected to symmetric (zero baseline) stroke loading (frame crosshead displacement) or equivalent symmetric gauge area symmetric strain loading [4].

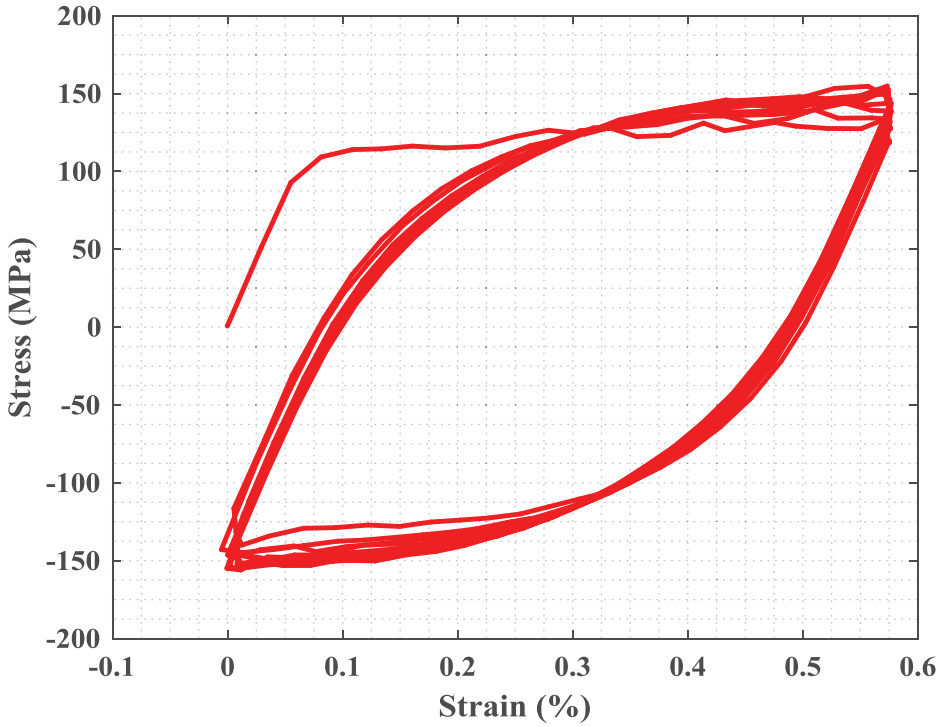

Figure 3. 5 First 10 cycle of hysteresis (input strain versus observed stress) curves for ET-F47 test. The fatigue specimen was subjected to asymmetric (with non-zero baseline) strain input obtained from FE model with case 1.

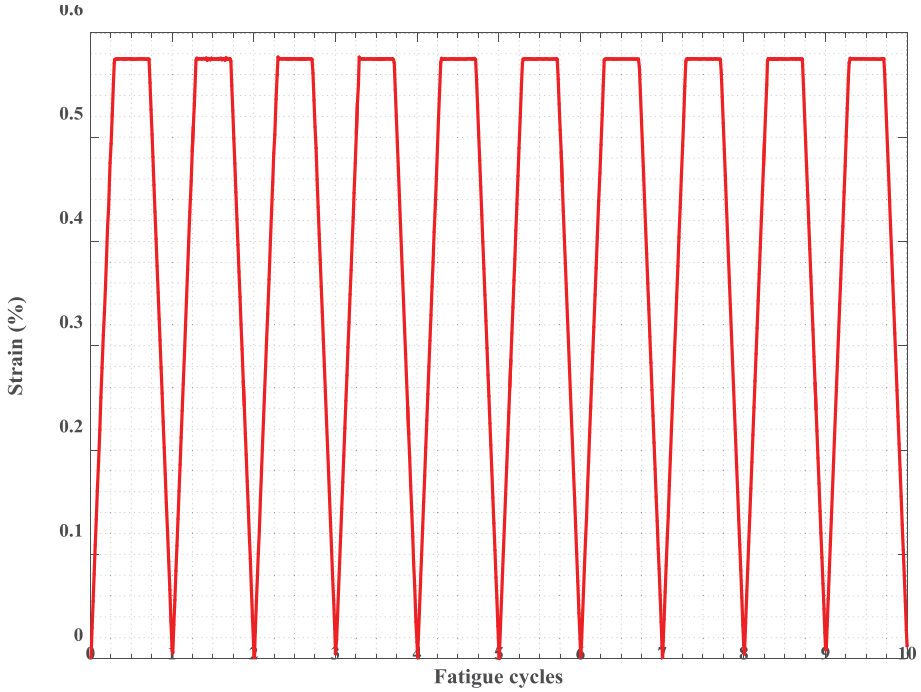

Figure 3. 6 First 10 cycle of input strain history for ET-F47 test. The fatigue specimen was subjected to asymmetric (with non-zero baseline) strain input obtained from FE model with case 1.

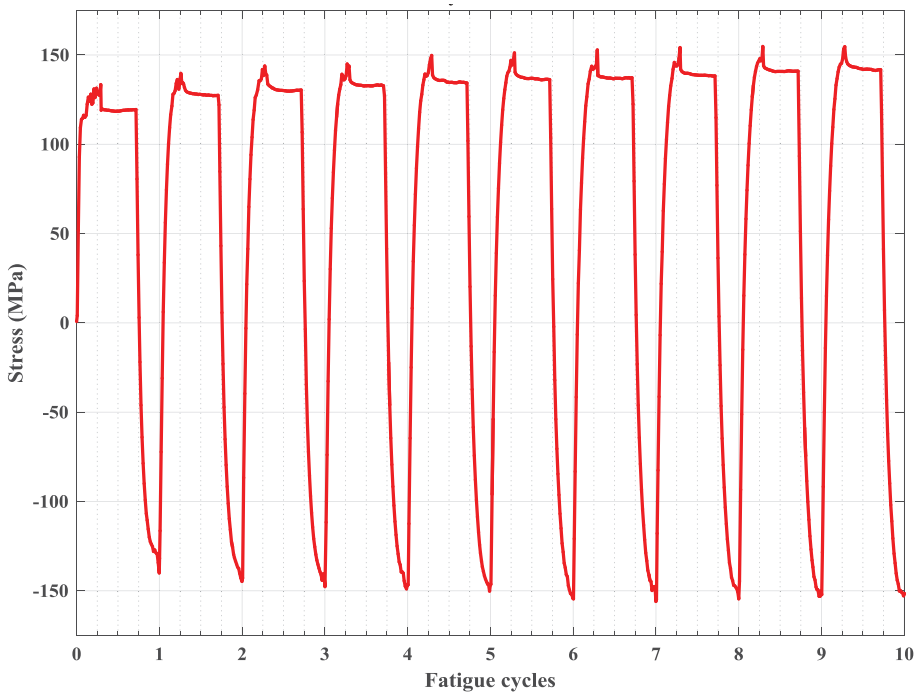

Figure 3. 7 First 10 cycle of observed stress history for ET-F47 test. The fatigue specimen was subjected to asymmetric (with non-zero baseline) strain input obtained from FE model with case 1.

3.2 ET-F48 Fatigue Test Results under Case 2

Fatigue test ET-F48 was conducted for case 2. Its strain profile is shown in Figure 3.8. This test input has a time period of 30 s. Similar to the strain input for ET-F47 (Figure 3.1), the ET-F48 strain input has an asymmetric strain profile, i.e., non-zero baseline and strain amplitudes only in the tensile direction. The resulting stress history of the ET-F48 specimen for the entire fatigue life is shown in Figure 3.9. The associated fatigue life is 15,966 cycles. Figure 3.10 presents the fatigue cycle versus maximum stress amplitudes for ET-F48. Similar to the ET-F47 fatigue specimen (Figure 3.3), the ET-F48 fatigue specimen also experiences both primary and secondary hardening due to the asymmetric strain loading associated with the thermal loading cycle in a real reactor component. More tests are needed to confirm the secondary hardening behavior. Figure 3.11 shows the first 10 cycles of hysteresis curves (input strain versus observed stress) for ET-F48. Figures 3.12 and 3.13 show the corresponding 10-cycle input strain and observed stress histories.

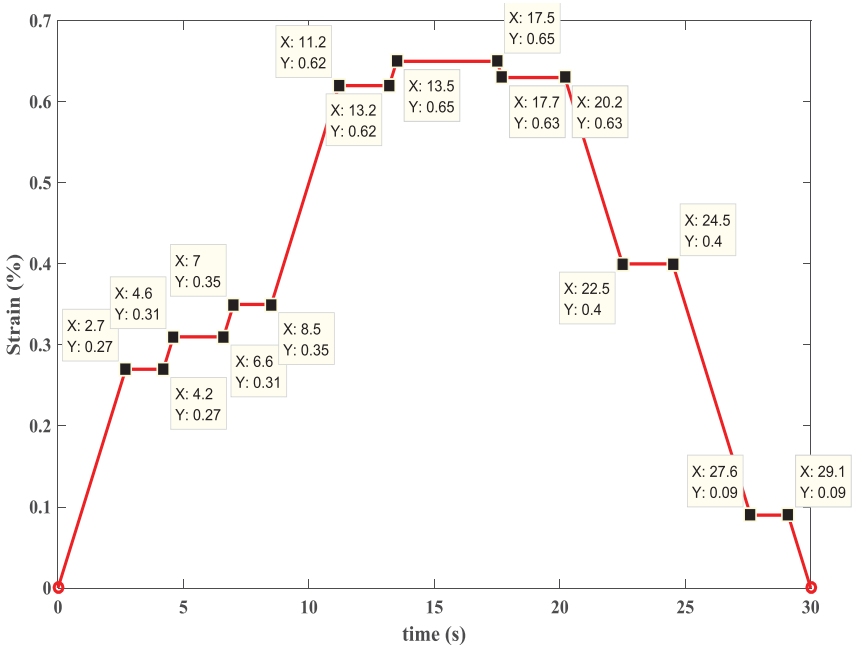

Figure 3. 8 ET-F48 input strain profile. The profile was estimated based on elastic-plastic FE model of PWR surge line pipe for case 2.

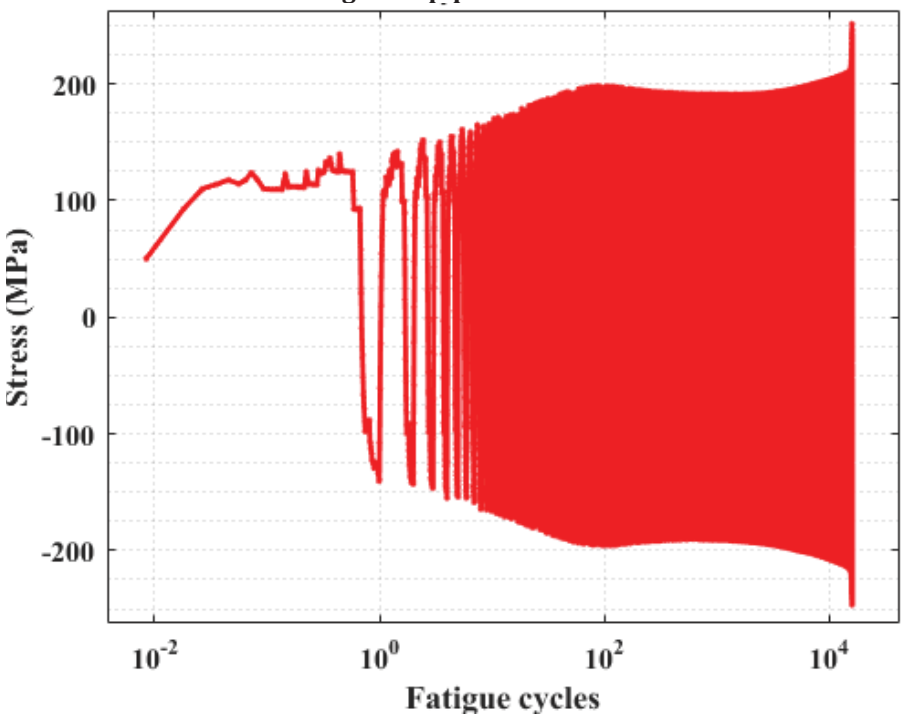

Figure 3. 9 Observed stress history from ET-F48 test. The fatigue specimen was subjected to asymmetric (with non-zero baseline) strain input obtained from FE model for case 2.

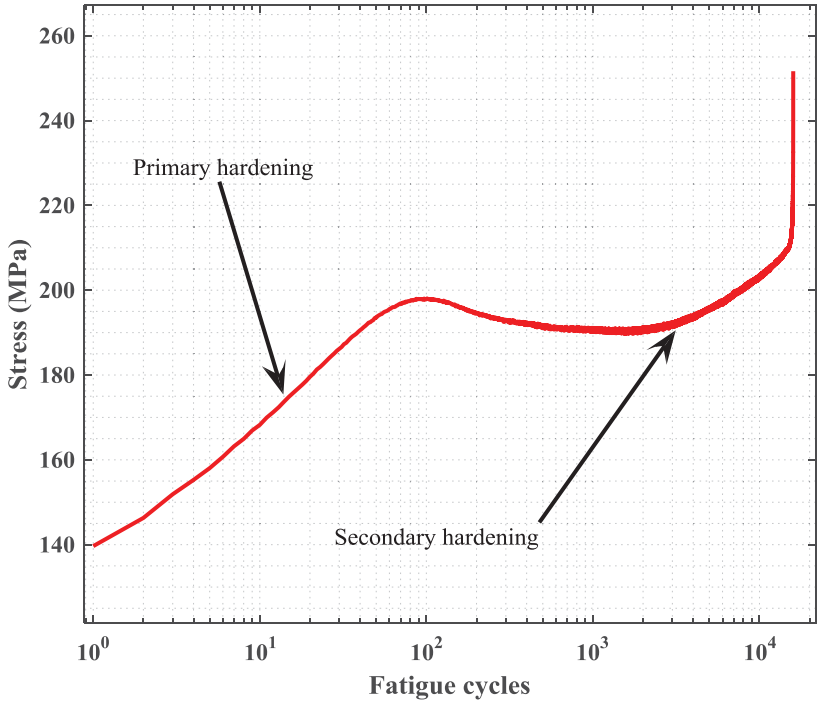

Figure 3. 10 Observed fatigue cycle versus maximum stress amplitudes for ET-F48 test. The fatigue specimen was subjected to asymmetric (with non-zero baseline) strain input obtained from FE model for case 2.

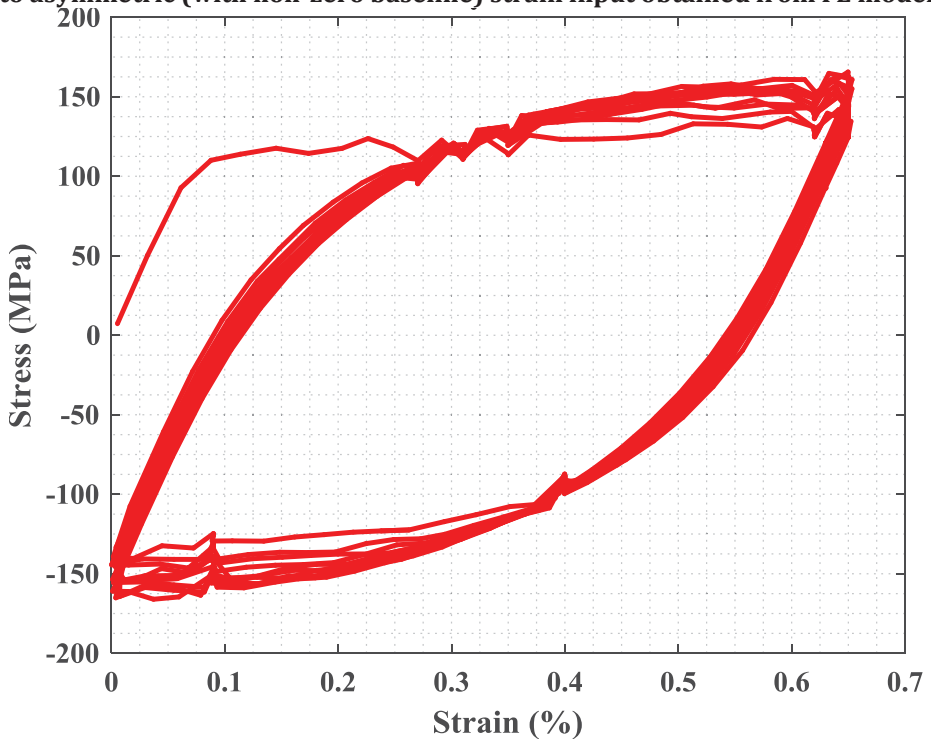

Figure 3. 11 First 10 cycles of hysteresis curves (input strain versus observed stress) for ET-F48. The fatigue specimen was subjected to asymmetric (non-zero baseline) strain input obtained from FE model for case 2.

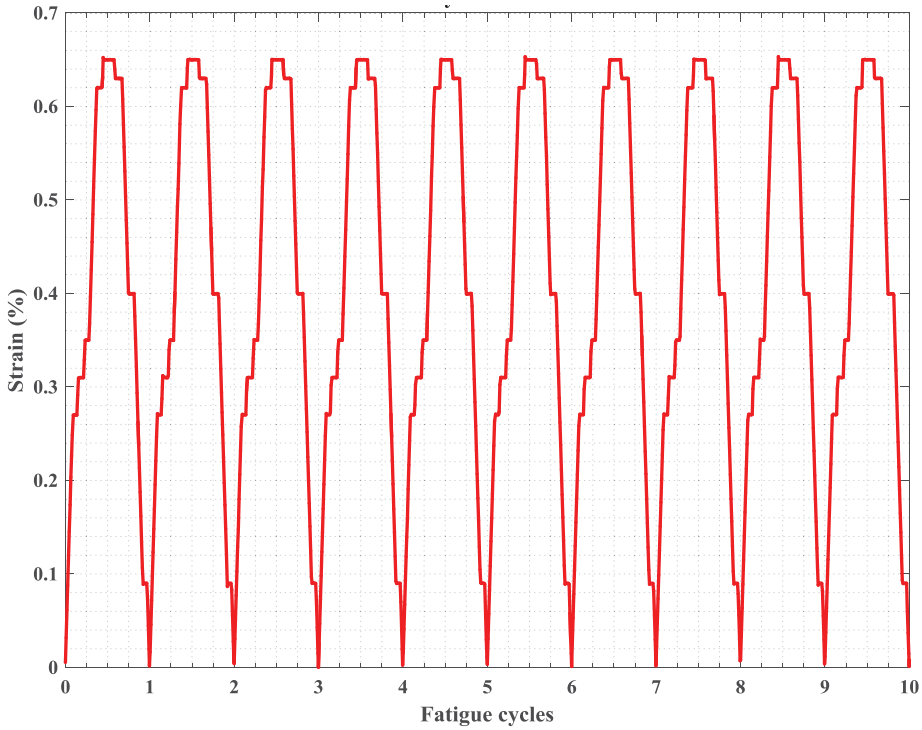

Figure 3. 12 First 10 cycles of input strain history for ET-F48. The fatigue specimen was subjected to asymmetric (with non-zero baseline) strain input obtained from FE model for case 2.

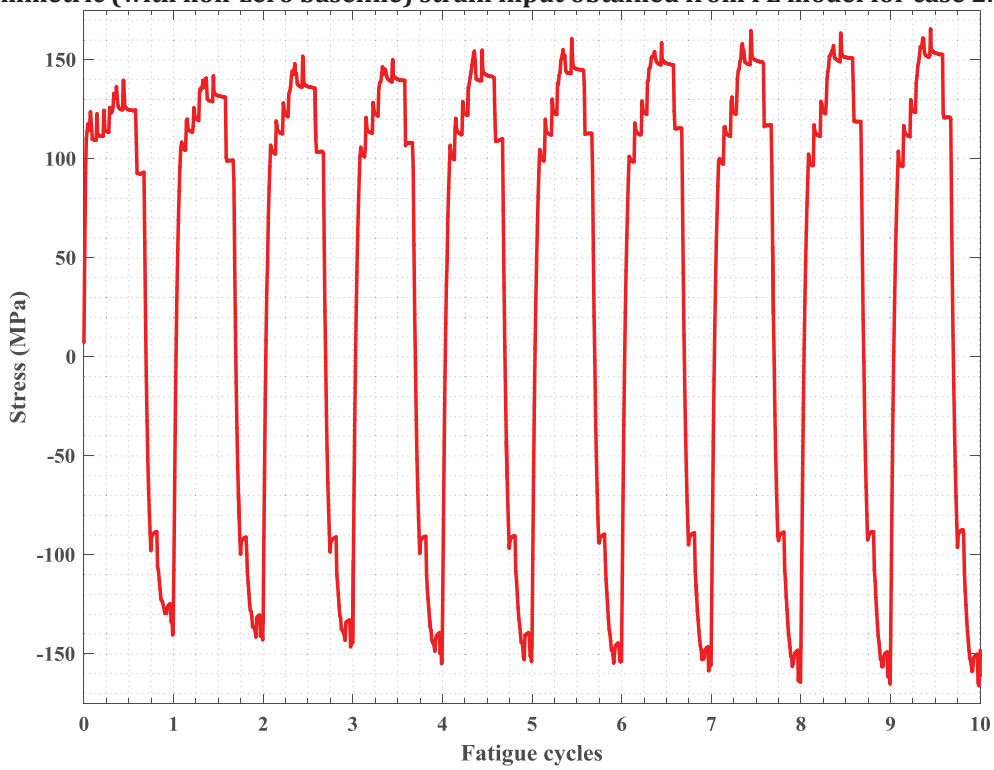

Figure 3. 13 First 10 cycles of observed stress history for ET-F48 test. The fatigue specimen was subjected to asymmetric (non-zero baseline) strain input obtained from FE model for case 2.

4 Implementation and Validation of Fully Mechanistic Modeling in an ABAQUS-WARP3D High Performance Computing Framework

Although approaches based on the S~N curve are widely followed for fatigue evaluation of nuclear reactor components and other safety critical structural systems, there is a chance of large uncertainties in the estimated fatigue lives. This uncertainty could be due to the over-dependence on empirical S~N curves based on end-of-life fatigue test data. The end-of-life data do not have much bearing on the exact evolution of material damage (e.g., cycle-dependent hardening and softening of material) over the entire fatigue life. This uncertainty might be reduced by using a more mechanistic approach, such as material model based on evolutionary plasticity and their implementation through physics-based FE modeling. In previous work [*5-9*], we proposed an evolutionary cyclic plasticity model for key reactor materials, including 316 SS base, 508 low alloy steel base, and 316 SS-316 SS weld. We assumed that the material yield surface and the corresponding hardening and softening behavior evolve over time. Thus, a single set of material parameters is not enough to predict material behavior for the entire fatigue lifetime. We demonstrated that material parameters (estimated from uniaxial fatigue experiments) such as elastic modulus, yield stress, and kinematic hardening do not stay constant but evolve over the lifetime of the specimen. Thus, material parameters should be functions of time or other physical states of the material, which can be defined as a "field variable." The use of field-variable material properties is important for accurate estimation of the evolution of the stress-strain state at a given time.

Based on the evolutionary cyclic plasticity material model in our recent work [1], we have developed an FE modeling framework to estimate the life of nuclear reactor components. A flowchart of this modeling framework is shown in Figure 4.1 [1]. As shown, the mechanistic-based fatigue modeling starts with uniaxial fatigue experiments followed by material model development (based on the evolutionary cyclic plasticity model) along with material model parameter estimations. The details of this work and related results are discussed in refs. [1, 3]. The next step is validation of the evolution cyclic plasticity model through analytical and 3D-FE modeling of the specimen. In a recent Argonne report [1], we presented analytical and 3D-FE modeling results of 316 SS fatigue specimens under constant, variable, and random loading and validated the model calculations with experimental results. We used a commercial code, ABAQUS, for the 3D-FE modeling. We developed a user material subroutine to incorporate the evolutionary cyclic plasticity model into ABAQUS. In the final step, as represented in Figure 4.1, the developed FE model framework and material model parameters are utilized to extrapolate uniaxial fatigue test-based material behavior to a multiaxial domain for structural analysis of nuclear reactor components subjected to multiaxial fatigue loading.

In our previous work [1], we performed a fatigue simulation of nuclear reactor components by extrapolating the evaluation of material behavior (e.g., material hardening and softening) under uniaxial fatigue loading. We performed a structural simulation of a PWR SL pipe under idealistic constant-amplitude loading for 100 cycles and compared the results with experimental data from a uniaxial constant-amplitude fatigue test of 316 SS. For the simulation, we used the FE modeling framework that was developed based on the evolutionary cyclic plasticity material models and implemented through commercially available ABAQUS FE software. However, we found that the component/system level FE simulation using commercial software, such as ABAQUS, is extremely expensive, particularly when using a large number of cores. For example, the simulation time for performing structural simulation of PWR SL pipe for 20 fatigue cycles is 29 hours when 1 CPU (Intel Xenon E5-2620, 2.4 GHz) and 1 GPU

(Nvidia Quadro K2200) are used. Furthermore, a fully mechanistic determination of the fatigue life of nuclear component/system requires structural analysis of the component for thousands of fatigue cycles. Thus, HPC implementation of our evolutionary cyclic plasticity model is required to simulate large components/systems for thousands of fatigue cycles. In this section, we present an approach for such a HPC framework.

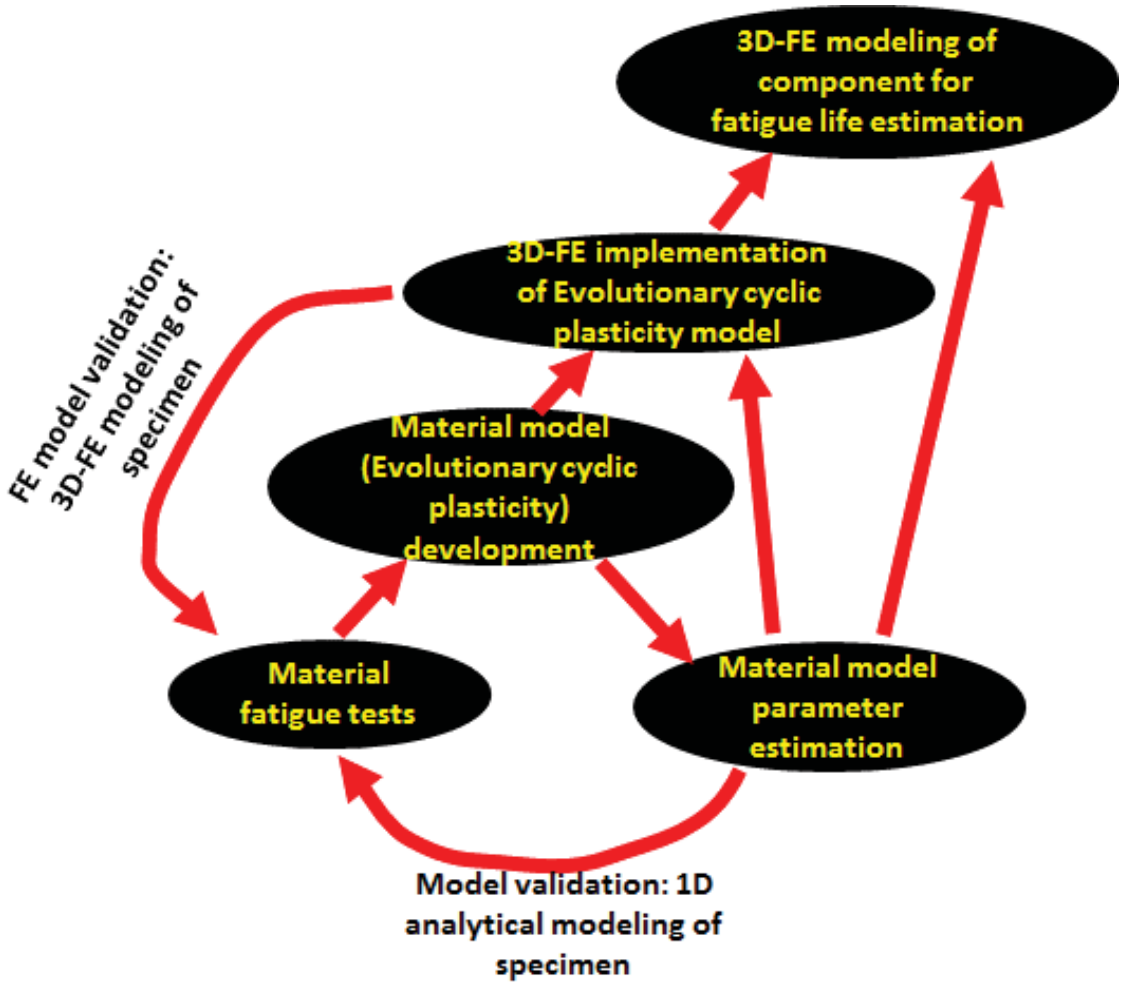

Figure 4. 1 Flowchart showing the steps in mechanistic-based fatigue modeling framework.

4.1 High Performance Computing Framework

Nowadays researchers and engineers are often required to use numerical methods to solve complex problems in mathematical modeling and design. The FE method is a powerful tool for numerical simulation of a wide range of problems, such as stress-strain analysis of components, heat transfer, and fluid dynamics. Implementation of the FE method in CAD systems allows engineers and researchers to solve large-scale models [10-14]. However, large engineering problems often require much more computation time and storage than available with regular desktop machines. Moreover, the complexity of many components and their construction leads to complex mathematical models of geometric areas, and the subsequent application of discretization techniques can lead to meshes with a large number of finite elements [10-14]. Powerful computational capability is required to process mathematical models

with a large number of finite elements and to obtain reliable results within a reasonable time. Furthermore, the mechanistic-based fatigue evaluation of nuclear reactor components/systems requires performing structural simulation for thousands of fatigue cycles, which necessitates use of significant computational resources. Parallel computing can fulfill such needs for HPC. Parallel computing is a type of computation in which many calculations or the execution of processes is carried out concurrently. Large problems can often be divided into smaller ones, which can then be solved at the same time. For many years, Open Multi-Processing (OpenMP) and Message Passing Interface (MPI) have been the two primary programming models most widely used for high performance computing. In the present work, the OpenMP- and MPI-based HPC frameworks (either standalone or in combination) are evaluated to ascertain their computational efficiency and are briefly described below.

4.1.1 OpenMP Approach

OpenMP is a portable approach for parallel programming on shared memory systems [15-16]. In a sheared memory system, each processor has access to a common shared memory space (Figure 4.2). OpenMP uses a multi-threading parallelizing approach whereby a master thread forks off a specific number of slave threads and the system divides a task among them (Figure 4.3). The threads then run concurrently, with the runtime environment allocating threads to different processors. The data within a parallel region are shared, so that they are visible and accessible by all threads simultaneously. OpenMP uses a portable, scalable model that gives programmers a simple and flexible interface for developing parallel applications for platforms ranging from standard desktop computers to supercomputers [15-16]. It is easy to program and debug. On the other hand, it is often hard to obtain decent performance from OpenMP, especially at large scale [17]. This is due to the fine-grained memory access governed by a memory model that is unaware of the non-uniform memory. Moreover, the scalability is limited by memory architecture. OpenMP is used only for parallelization across multiple cores on the same node of a cluster.

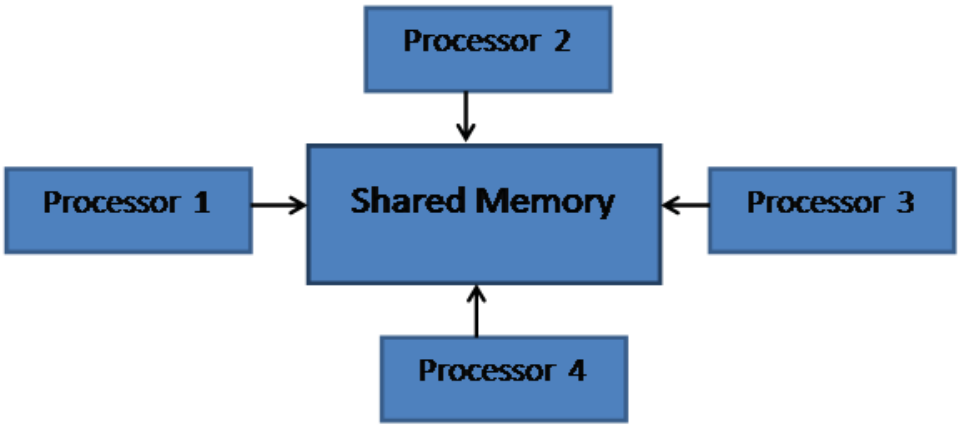

Figure 4. 2 Shared memory system where Processor 1, 2, 3, and 4 can see whole memory (OpenMP).

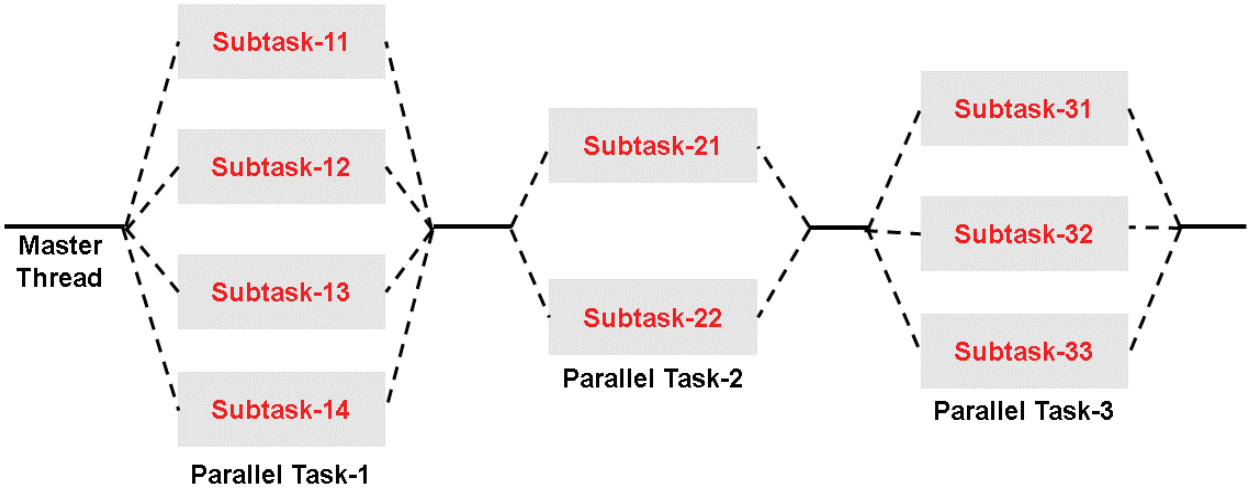

Figure 4. 3 Illustration of multi-threading during OpenMP.

4.1.2 Message Passing Interface Approach

MPI is a portable message-passing style of parallel programming. It is based on a distributed memory model, where each processor has its own local memory (Figure 4.4). The processors communicate with each other via calls to MPI functions. The availability of optimized MPI libraries on a wide range of machines along with full control in the development cycle makes the MPI model advantageous in terms of achievable performance and portability [17]. However, the discrete memory view in programming makes it difficult to write code and often involves a very long development cycle [18, 19]. Carefully thought-out strategies are required for partitioning the data and managing the resultant communication. Moreover, due to the distributed nature of the model, global data may be duplicated for performance reasons, resulting in an increase in the overall memory requirement.

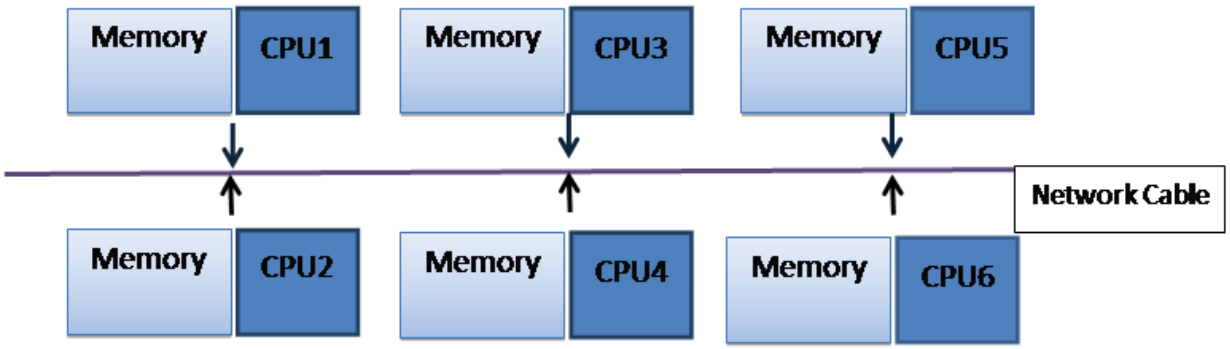

Figure 4. 4 Distributed memory system where CPUs can see only limited memory of their own and communicate via message passing through a network cable (MPI).

4.1.3 Hybrid MPI + OpenMP Approach

Today most HPC systems feature a hierarchical hardware design in which shared memory nodes with several multi-core CPUs are connected via a network infrastructure. Parallel programming must combine distributed memory parallelization on the node interconnect with shared memory parallelization inside each node [20], which can be achieved by using a hybrid MPI + OpenMP approach. In this approach, as shown in Figure 4.5, MPI is used for communication across distributed memory nodes, and OpenMP is used for fine-grained parallelization within a node [17, 19, and 20]. By using the advantages of both OpenMP and MPI models, the hybrid model can maintain cross-node performance with MPI and reduce the number of MPI processes needed within a node. The hybrid approach can help reduce the demand for memory and network, which can be very important for running very large jobs. Due to its easily exploitable multilevel parallelism, the hybrid model can potentially reduce application development effort [17, 19, and 20].

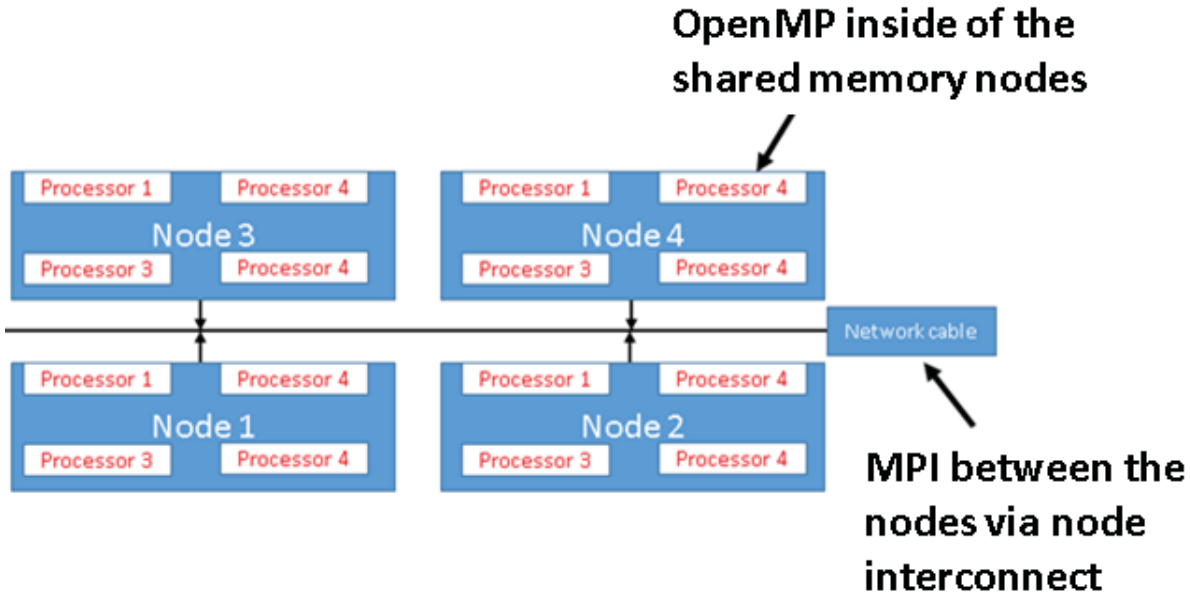

Figure 4. 5 Hybrid MPI + OpenMP model for a cluster of four nodes.

4.2 Framework for Fully Mechanistic Fatigue Evaluation using HPC

Speeding up the FE simulation of components or systems requires the use of a higher number of cores, which is extremely costly, particularly when a commercial FE code is used. Also, commercial software is not necessarily optimized for use in an HPC environment. An open source parallel computing solver along with a multi-core cluster can be used to scale up the number of cores and perform the FE simulation within a reasonable time. Figure 4.6 shows a schematic of Argonne National Laboratory's (ANL's) approach to evaluating the fatigue life of large components/systems using HPC. According to the framework, a commercial FE code such as ABAQUS can be used to generate the CAD model and FE mesh along with the loading and boundary conditions of the component/system. The ABAQUS generated model can then be used in an open source parallel solver for numerical

calculations. We have selected WARP3D [21] as an open source FE solver for mechanistic fatigue simulation. WARP3D can use the hybrid MPI + OpenMP on a multi-core parallel system. To incorporate ANL's evolutionary cyclic plasticity model and a material behavior model dependent on time and the accumulated plastic strain energy (APSE) for fully mechanistic fatigue evaluation, we developed a material and mechanics model code and implemented it in WARP3D. We used the Nuclear Engineering Division's HPC cluster facility at ANL to perform the final FE simulation.

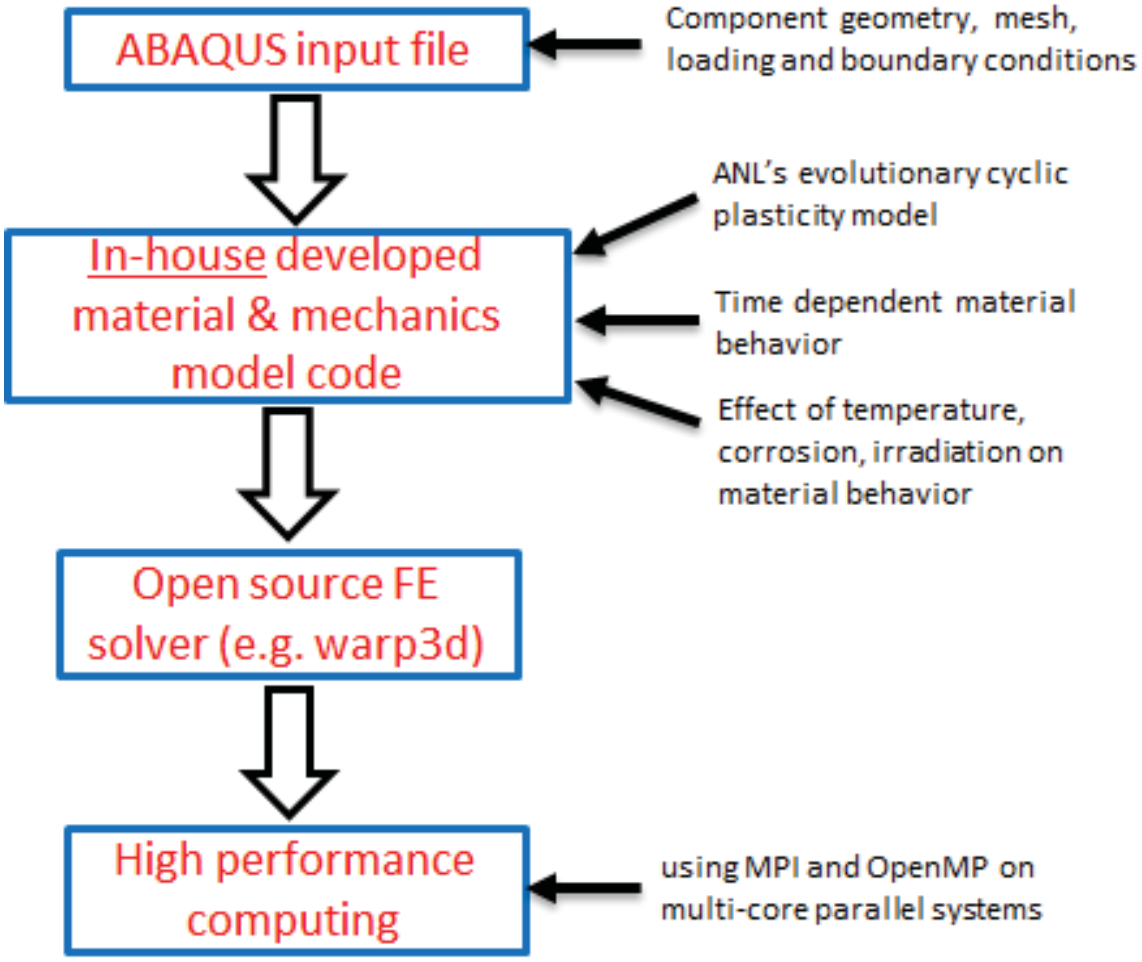

Figure 4. 6 Schematic of ANL's approach for fully mechanistic fatigue evaluation of large components/systems using high performance computing.

4.3 Fully Mechanistic Fatigue Evaluation of PWR SL Pipe under Ideal Loading

We performed an elastic-plastic analysis of a PWR SL pipe. The FE mesh of the PWR SL along with the boundary conditions and the direction of applied displacement is shown in Figure 4.7a. Cyclic displacements equivalent to ±0.5% constant strain amplitude in the negative z-direction were applied to nodes near one of the ends, as shown in Figure 4.7b. The profile of the applied cyclic displacement is shown in Figure 4.7c. Application of the 0.5% strain amplitude may seem unwarranted. However, the

motivation of selecting the strain amplitude is based on a computational fluid dynamics/heat transfer analysis and subsequent ST analysis results of the SL pipe under outs-surge condition. The related analysis results are discussed in ref. [1]. Unlike the actual case discussed in ref. [1], where the strain loading is multiaxial due to actual multiaxial thermal-mechanical loading, in this work, the strain was applied only along the vertical direction. There are two reasons for applying strain loading along only one direction. First, applying multiaxial strain loading at different nodes (according to actual loading conditions) in the FE model is nearly impossible. Second, we wanted to compare the life of the SL with the experimentally observed life of the uniaxial specimen under a constant-amplitude fatigue test (ET-F41 test in Refs. [1, 22]), so we decided to keep a similar loading condition for the component. Through this ideal loading case, we are trying to compare the simulation results with uniaxial fatigue experiment (ET-F41) data and determine whether the FE framework (Figure 4.1) based on the evolutionary cyclic plasticity model is applicable for component-level elastic-plastic analysis. We used the APSE-based modeling approach for structural simulation of the PWR SL pipe. Details of the APSE-based modeling can be found in Refs. [1, 22].

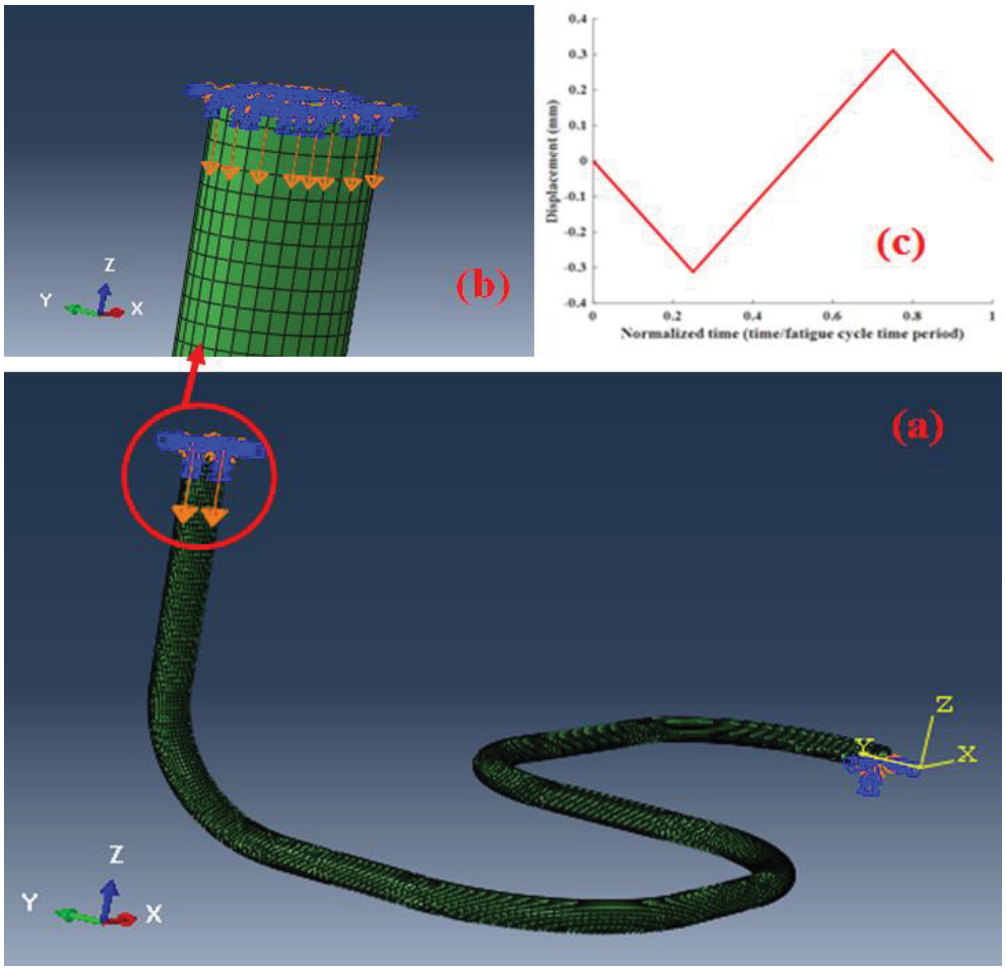

Figure 4. 7 (a) FE mesh of the PWR SL pipe. Blue arrows at two ends show the fixed boundary condition, (b) yellow arrows indicate the location and direction of applied cyclic displacement. (c) profile of the applied cyclic displacement.

4.3.1 Computational Time vs. Number of CPUs

To investigate how increasing the number of CPUs reduces the computational time of the simulation, we performed structural simulations of PWR SL pipe for 10 fatigue cycles. These simulations were performed using both commercial FE code (ABAQUS) and open source FE code (WARP3D). Table 4.1 shows the change in computational time for the ABAQUS simulation with the number of CPUs. Note that the ABAQUS simulation was performed on a 32 core node. Also note that the auto step size was employed during the ABAQUS simulation. Table 4.1 shows that the simulation time is greatly reduced with the increase of the number of CPUs. It should be noted that our current ABAQUS license does not allow the use of more than 22 CPUs for simulation. Thus, further increase of the number of CPUs to reduce the simulation time additionally was not possible due to lack of ABAQUS license tokens. To enable the use of a higher number of CPUs, we have developed a WARP3D open source software based on computing HPC framework for multi-cycle fatigue evaluation of reactor components. This framework is still in the development stage.

In this report, we present some preliminary results based on this framework. Table 4.2 shows the computation time using only OpenMP and hybrid MPI + OpenMP. As seen in the table, the computation time to simulate 10 fatigue cycles had been significantly reduced from 5.3 to 0.5 hr by using 64 CPUs on hybrid MPI + OpenMP model and 40 fixed steps per fatigue cycle. We used this combination to simulate the PWR SL pipe for full-life fatigue simulation, the computation time for which was 12.5 days.

Table 4. 1 Computation time as a function of CPUs to simulate PWR SL for 10 fatigue cycles using ABAQUS

Number of CPUs[a]	4	8	12	22[b]
Computation time (hr)	25.1	10.3	8.9	3.5

[a] A 32 core node was used for simulation but the number of CPUs used during simulation was restricted by the number of ABAQUS license tokens.

[b] Maximum number of CPUs that can be used by current ABAQUS license.

Table 4. 2 Computation time as a function of CPUs to simulate PWR SL for 10 fatigue cycles using WARP3D and HPC

	Number of CPUs	Computation time (hr)	
OpenMP (1 node with 32 cores)	32	5.3	Non-uniform step size similar to ABAQUS simulation in Table 4.1
MPI + OpenMP (2 nodes, each with 32 cores)	64	2.5	Non-uniform step size similar to ABAQUS simulation in Table 4.1
MPI + OpenMP (2 nodes, each with 32 cores)	64	0.5	Fixed step size (40 steps per fatigue cycles)

4.3.2 Full-Life Fatigue Simulation and Comparison with Experiment

Full-life fatigue simulation of the PWR SL pipe was performed under ideal constant-amplitude displacement control loading as shown in Figure 4.7. Full-life simulation was performed using WARP3D and hybrid MPI + OpenMP based on the developed framework, as discussed in Section 4.2, for HPC mechanistic fatigue evaluation. An element with the highest stress values was selected from the FE model to compare the full-life fatigue simulation results (at the centroid of that element) with experimental observation. This element was determined from the contour plot of the ABAQUS simulation. While the ABAQUS simulation was not performed for full fatigue life simulation, the results were used for visual observation of the stress-strain state of the PWR SL pipe after a few fatigue cycles. WARP3D based HPC framework was used for full-life fatigue simulation. As mentioned in previous sub-section, the computation time for full-life fatigue simulation of PWR SL pipe was 12.5 days. For the full-life simulation using WARP3D based HPC framework, we used MPI+OpenMP (2 nodes, each with 32 cores) with total 64 CPUs. Note that WARP3D only outputs simple flat files of node and element results in text or stream formats [23], which were processed with a program developed in MATLAB.

Figure 4.8 shows a contour plot of the von Mises stress at a typical instant. As shown in the figure, maximum stress concentration occurs in the elements that are directly subjected to the applied deformation. One of these elements, as shown in the magnified inset in Figure 4.8, was selected as the element of interest for analyzing the results from simulation. As the evolutionary cyclic plasticity model uses von Mises stress for checking the yield criteria during elastic-plastic analysis, the von Mises stress is used for comparing simulation results with experimental observations. A comparison between von Mises stress amplitudes determined from experimental observation and simulation is shown in Figure 4.9. The curves indicate initial material hardening followed by softening in the simulated stress profile; this behavior is typical of 316 SS as observed during uniaxial fatigue tests. The calculated value of maximum hardening von Mises stress from the simulation is 243.6 MPa, which is very close to the experimentally observed value (244.2 MPa). The simulated stress profile also indicates that the model can predict the material behavior during the initial rapid hardening, the quasi-stable state (during quasi-stabilized cycles), and the fast stress drop toward the end of the fatigue life (which represents unstable or rapid crack propagation). The simulated fatigue life was 5855 cycles, which is 85% accurate as compared to the experimental fatigue life (6914 cycles) of the specimen.

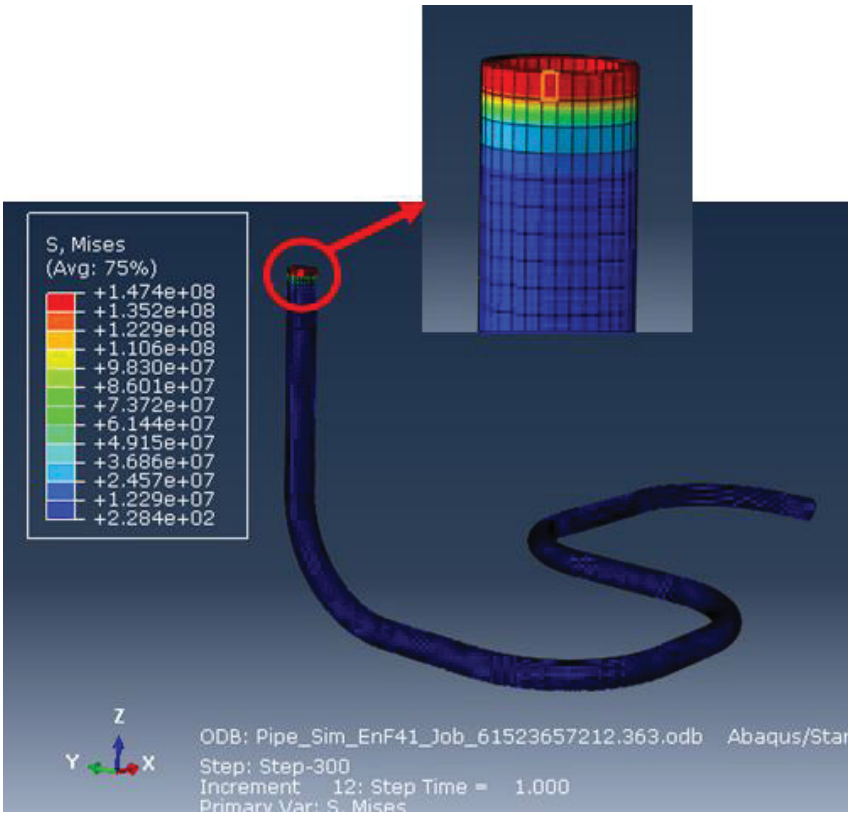

Figure 4. 8 Contour plot (from ABAQUS simulation) of the von Misses stress at an instant during the displacement control fatigue loading shown in Figure 4.7. The highlighted element in the magnified inset is the element of interest for analyzing results from full life simulation using WARP3D and hybrid MPI + OpenMP.

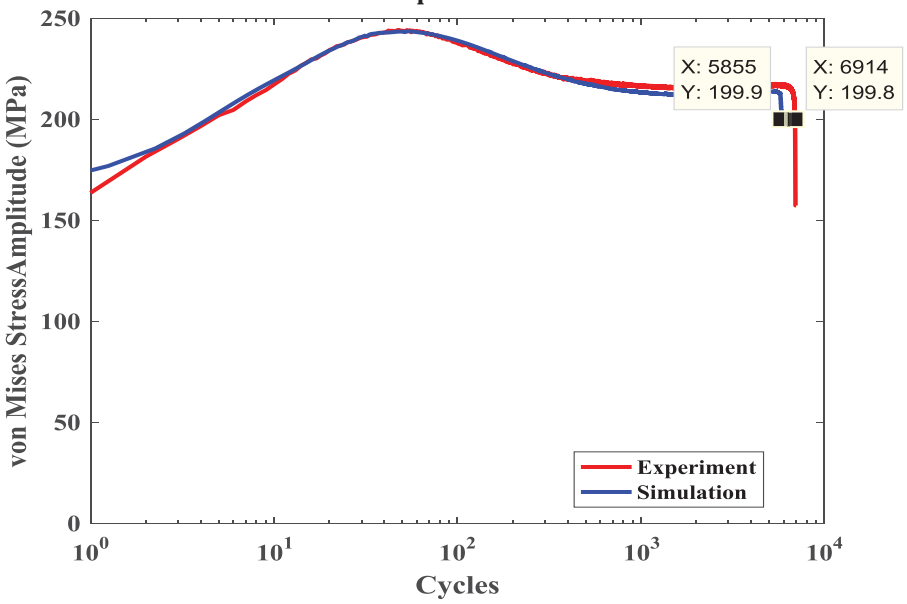

Figure 4. 9 Von Mises stress amplitudes from experiment and simulation.

5 Finite Element Full-Life Simulation of Fatigue Specimen Subjected to PWR-SL Experienced Design-Basis Loading Profiles

In Section 3, we presented results from strain-controlled uniaxial fatigue experiments performed under simplified and detailed design-basis loadings. In this section, we present results from fatigue modeling of 316 SS specimens under both loading cases and compare the experimental and simulated fatigue lives. We performed the full-life fatigue simulation of ET-F47 and ET-F48 tests (see Section 3 for experimental results) on a single 3D eight-node brick element representing the gauge section (0.5 in.) of the fatigue specimen. The geometry of the actual specimen and FE-modeled equivalent specimen is shown in Figure 5.1. A single element was used to reduce the computational time for simulating thousands of fatigue cycles. The cross section of the 3D brick element (hexahedral 8-node linear brick element: C3D8) was considered equal to the nominal cross section of the specimen. Simulations representing strain-controlled fatigue tests ET-F47 and ET-F48 were performed by applying corresponding deformation in the z-direction, as shown by the arrows in Figure 5.1. Note that ET-F47 represents fatigue loading under case 1 (refer to Figures 2.2 and 3.1), while ET-F48 represents fatigue loading under case 2 (refer to Figures 2.3 and Figure 3.8). We performed the FE simulations using our HPC mechanistic modeling framework (see Section 4.2 and Figure 4.6 for details). We used the APSE-based fatigue modeling approach [1], the details of which can be found in ref. [1]. In this approach, the calculated APSE at the end of a time step is used to select the material parameters for predicting the stress-strain in the next step. The material parameters estimated from a variable-amplitude fatigue test (ET-F38 in ref. [1]) were used for the APSE-based modeling.

Figures 5.2 to 5.5 show the material parameters calculated as functions of APSE. Note that the APSE-dependent elastic modulus (Figure 5.2) and elastic-limit stress (Figure 5.2) do not change much except during the end. However, the Chaboche parameters (C_1 and $\gamma 1$) show strong dependence on APSE. The lack of change in elastic modulus and elastic-limit stress indicates that the elastic behavior of the material does not change much with respect to APSE. In our previous work [1] and in the present work, the elastic limit stress is used as the yield limit stress to capture more of the plasticity region under the stress-strain curve. The strong dependence of the Chaboche parameters on APSE shows that 316 SS experiences significant cyclic hardening and softening associated with cyclic plasticity. Nevertheless, these APSE-dependent material parameters were used to map the material parameters between the earlier variable-amplitude test (ET-F38 in ref. [1]) and the tests (ET-F47 and ET-F48) being modeled here. The simulation results for the loading cases are given below.

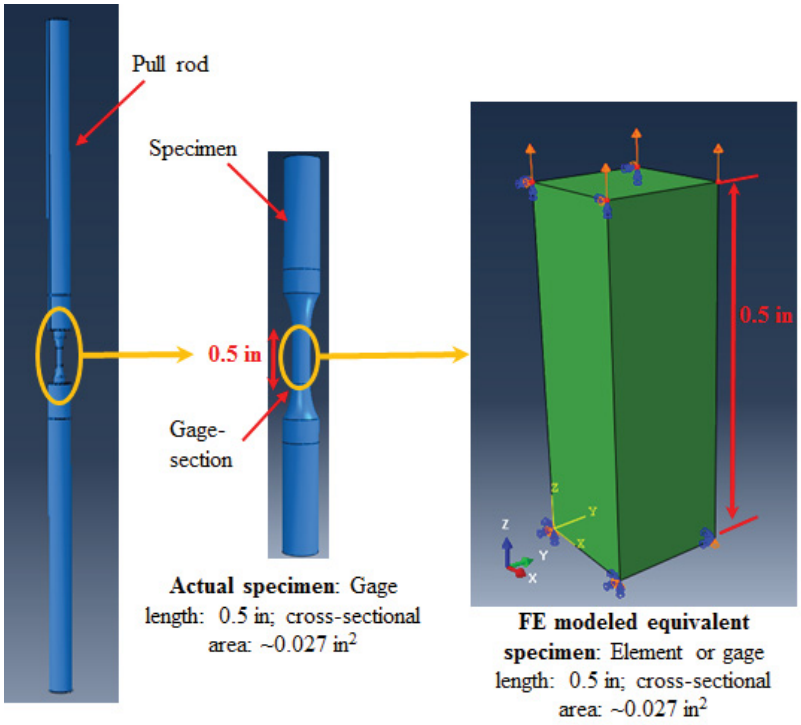

Figure 5. 1 Three-dimensional 8-node brick element used for FE simulation of fatigue experiment in WARP3D.

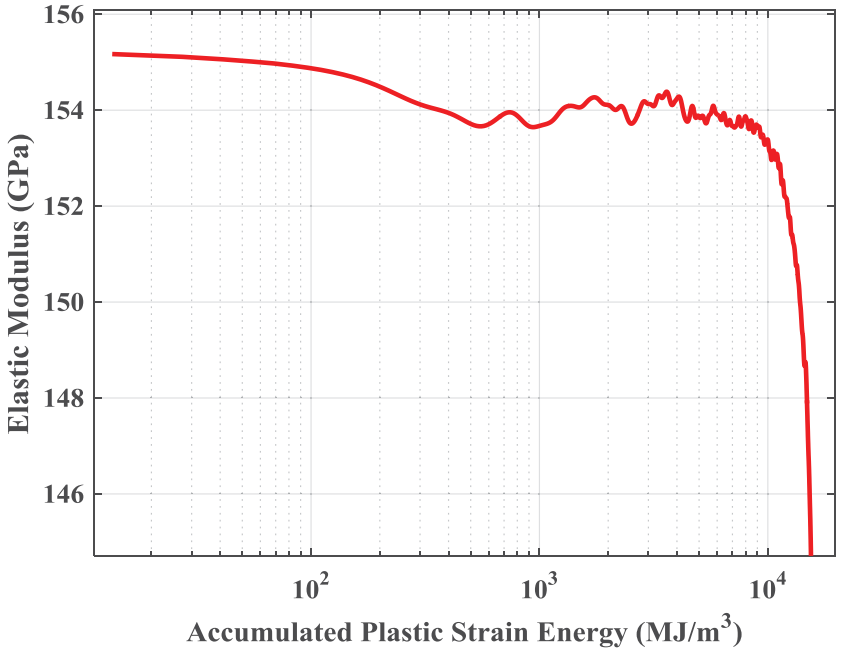

Figure 5. 2 APSE-dependent elastic modulus.

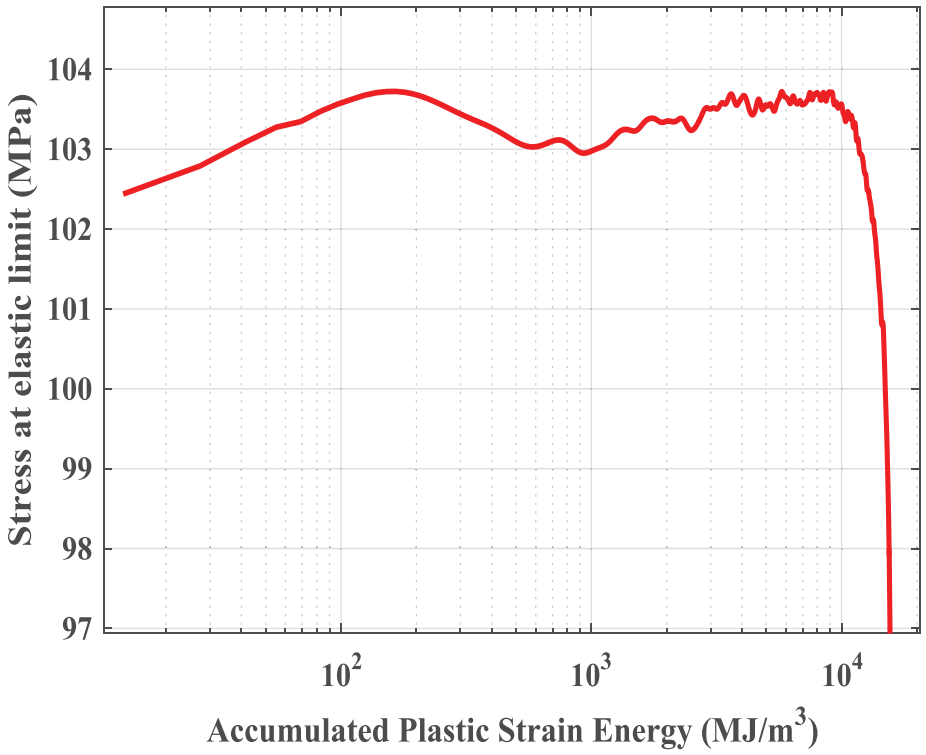

Figure 5. 3 APSE-dependent elastic limit stresses, which was used as the yield stress.

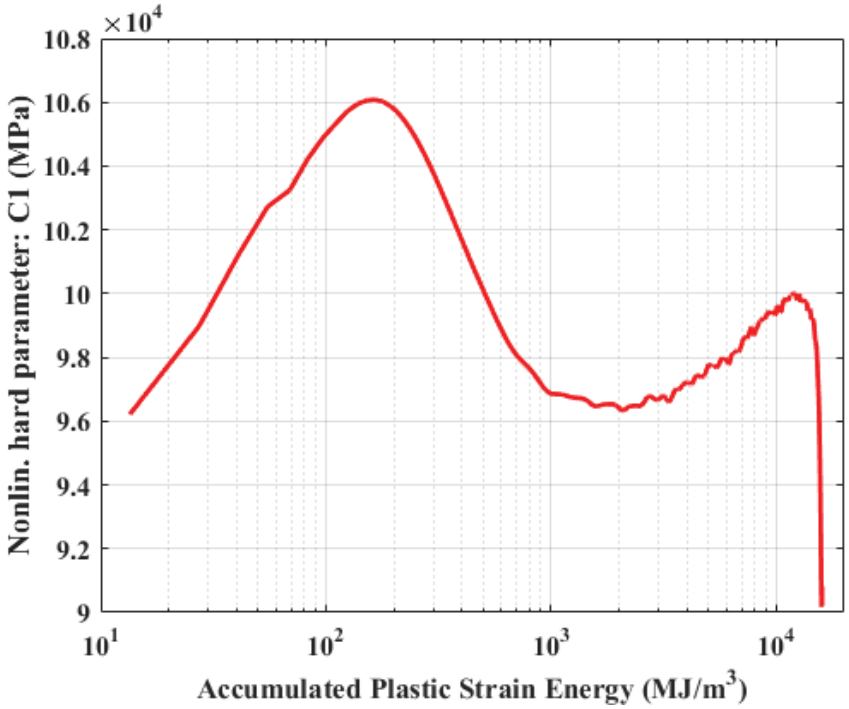

Figure 5. 4 APSE-dependent nonlinear kinematic hardening parameter C_1.

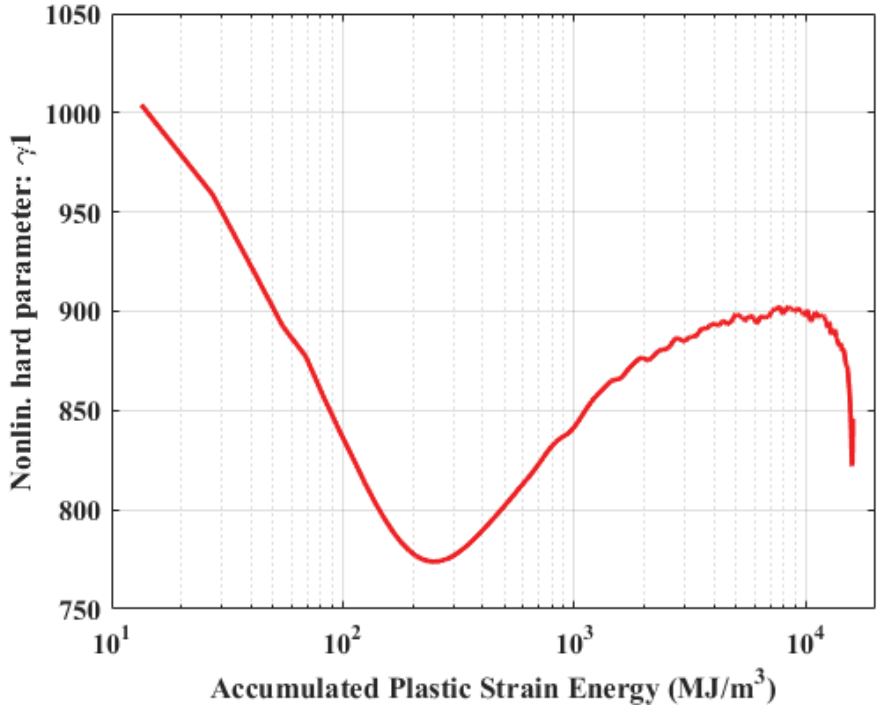

Figure 5. 5 APSE-dependent nonlinear kinematic hardening parameter, γ1.

5.1 Full-Life Simulation of ET-F47 Specimen Subjected to Case 1: Simplified Design-Basis Loading Profile

Using the HPC fatigue simulation framework and strain profile shown in Figure 3.1, the stress history of ET-F47 was simulated up to final failure. For the failure cycle prediction, the ASME-based load drop criterion of 25% was selected. The simulated and experimental fatigue lives are compared in Table 5.1. Under case 1 loading, the simulated fatigue life is 19,700 cycles, which is 79% accurate compared to the experimental fatigue life. Figure 5.6 shows the simulated stress profile for the entire fatigue life. Figure 5.7 shows the first 10 cycles of the simulated stress-strain hysteresis curves. The corresponding 10-cycle strain history can be found in Figure 3.6. The simulated 10-cycle stress history is shown in Figure 5.8. The simulation was conducted using a desktop computer with 12 CPUs (Intel Xenon E5-2620, 2.4 GHz) and with an approximate simulation time of 5 hours. Note that for single element simulation (as it in the present case) it may not be beneficial to use HPC, because parallelization significantly helps when it requires solving large stiffness matrix associated with large number of finite elements. The discussed two-step approach of ABAQUS based single cycle model of the entire component and then the WARP3D based single element FE model for entire fatigue life, can give an firsthand approximation of fatigue life. However, For more accurate fatigue life estimation it is required to perform cycle-by-cycle FE modeling of entire component as discussed in Sections 4.2 and 4.3.

Nevertheless, the predicted life is 79% accurate compared to the experimental fatigue life. However to note that the simulated stress profile (magnified 10-cycle stress history shown in Figure 5.8) is not the same as the experiment stress profile (magnified 10-cycle stress history shown in Figure 3.7). This

discrepancy is further evident by comparing the fatigue cycle versus maximum stress amplitude predicted through FE simulation (Figure 5.9) and experiment (Figure 3.3). The simulated maximum stress amplitude only shows the primary stress hardening, whereas the experiment shows both primary and secondary stress hardenings. The possible reasons of discrepancy between predicted and experimental stress history and associated remedial measures are discussed at the end of this section.

Table 5. 1 Experimental and simulated fatigue life under different design basis loading types

	Single-element FE simulation (cycles)	Uniaxial fatigue experiment (cycles)	Accuracy (%)
Case 1: Simplified design-basis loading cycle	19,700	24,800	79
Case 2: Detailed design-basis loading cycle	15,400	15,966	96

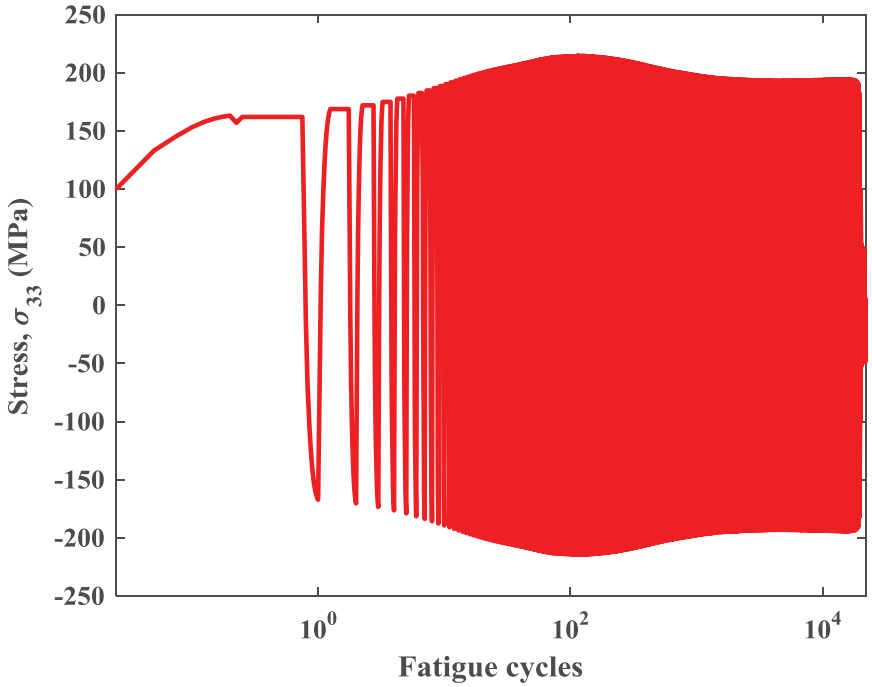

Figure 5. 6 Simulated stress profile for ET-F47 fatigue specimen under case 1 (strain input shown in Figure 3.1).

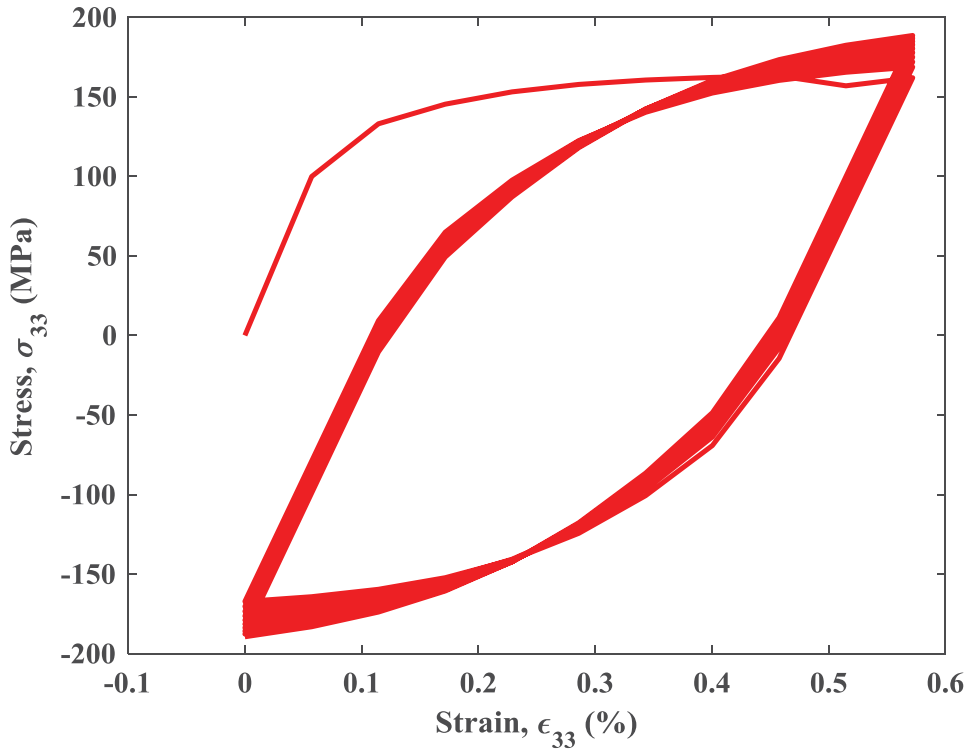

Figure 5. 7 First 10 cycles of simulated stress-strain hysteresis curves for ET-F47 (case 1).

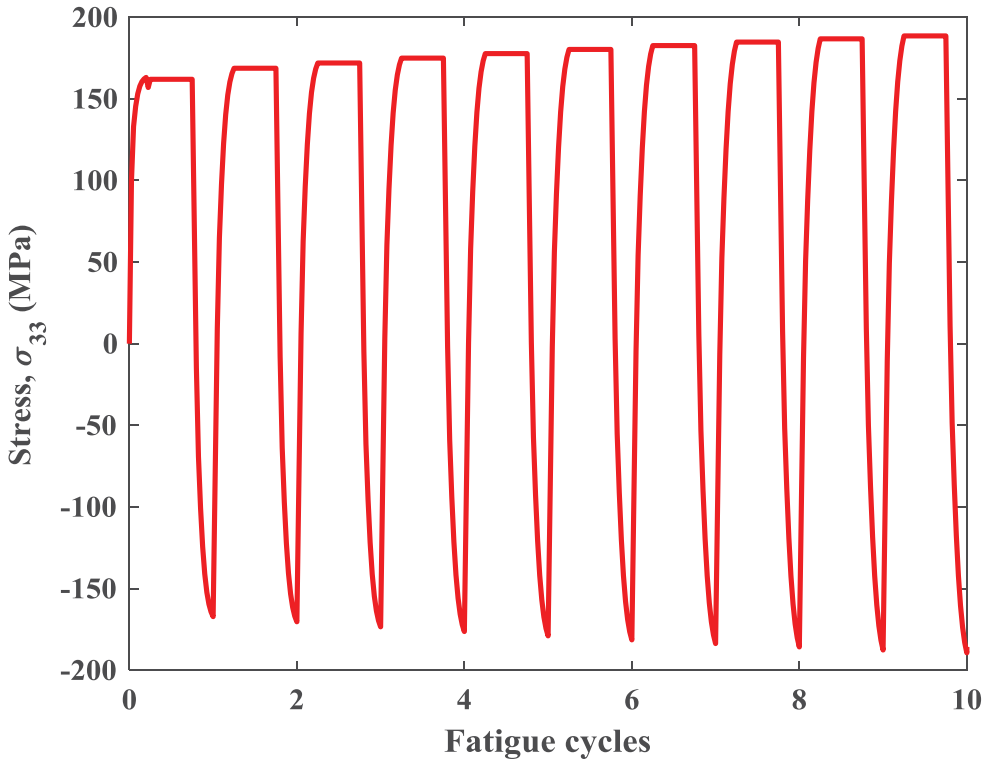

Figure 5. 8 First 10 cycles of simulated stress history for ET-F47 (case 1).

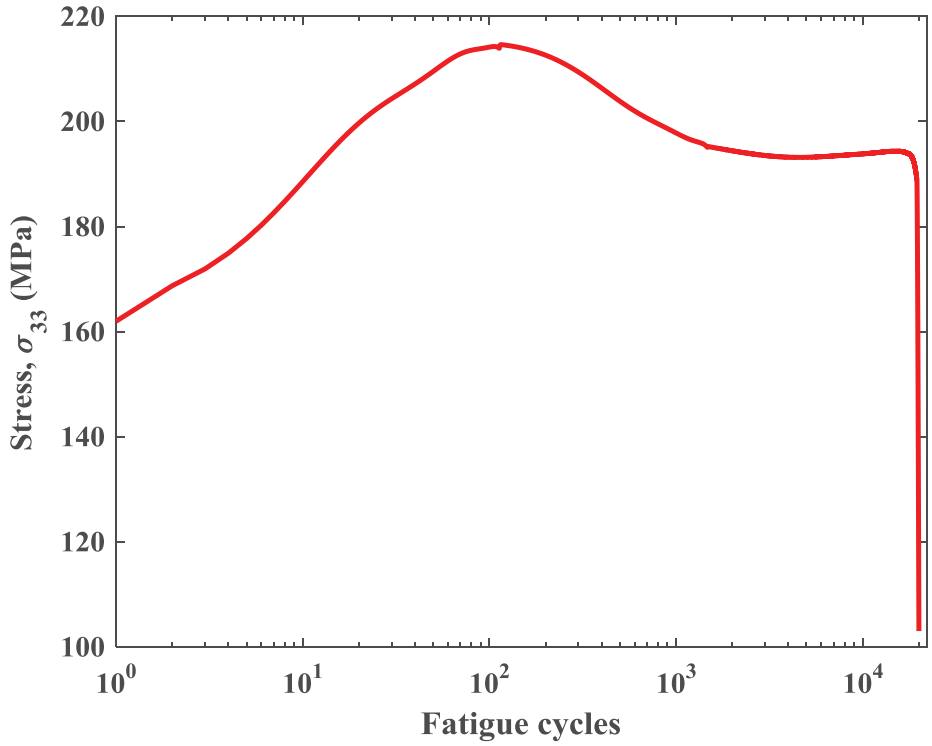

Figure 5. 9 Simulated fatigue cycles versus maximum stress amplitudes for ET-F47 (case 1).

5.2 Full-Life Simulation of ET-F48 Specimen Subjected to Case 2: Detailed Design-Basis Loading Profile

In addition to the ET-F47 simulation, we simulated ET-F48 using the HPC fatigue simulation framework and strain profile under case 2 (shown in Figure 3.8). The objective is to simulate the stress history of the ET-F48 specimen up to final failure (Figure 5.10). The corresponding predicted life (based on the 25% load drop criterion of ASME) is 15,400 fatigue cycles, which is very close to the experimental life of 15,966 fatigue cycles (Table 5.1), with 96% accuracy. The simulation was conducted using a desktop computer with 12 CPUs (Intel Xenon E5-2620, 2.4 GHz) and with an approximate simulation time of 4 hours. Figure 5.11 shows the first 10-cycle hysteresis curves. The corresponding 10-cycle history can be found for strain in Figure 3.12 and stress in Figure 5.12. Comparing the simulated stress history (Figure 5.12) with the experiment stress history (Figure 3.13), we can see that, although the predicted fatigue life is 96% accurate, the simulated stress profile is not quite similar to the experiment stress profile. This difference is further evident by comparing the fatigue cycle versus maximum stress amplitude plot from the FE simulation (Figure 5.13) and experiment (Figure 3.10). Similar to case 1, the simulated maximum stress amplitude from case 2 only shows the primary stress hardening, whereas the corresponding experiment shows both primary and secondary stress hardening.

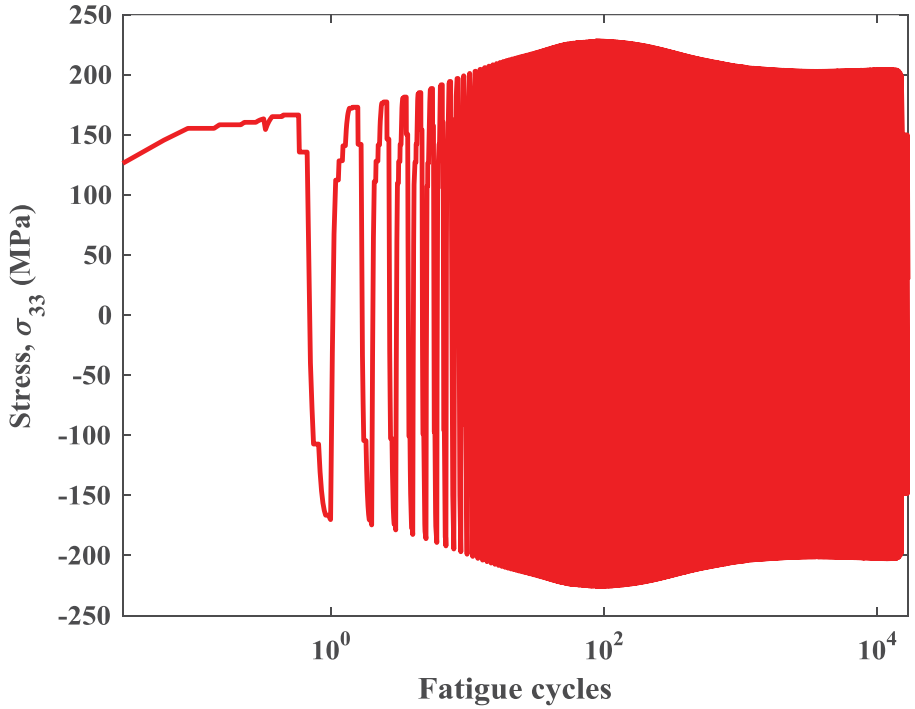

Figure 5. 10 Simulated stress history for ET-F48 fatigue specimen under case 2 (strain input shown in Figure 3.8).

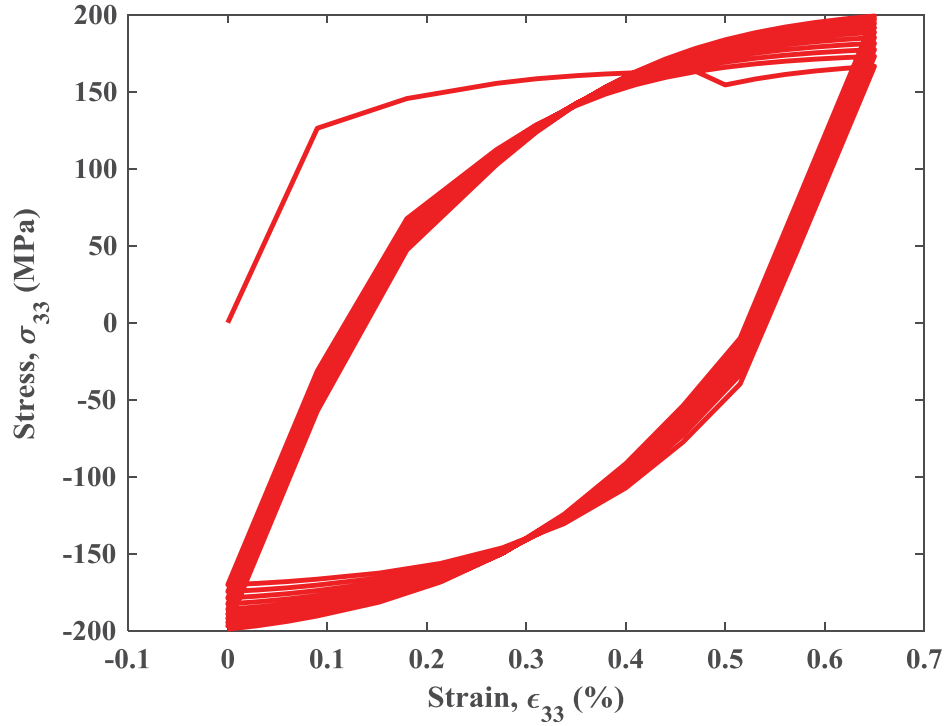

Figure 5. 11 First 10 cycles of simulated stress-strain hysteresis curves for ET-F48 (case 2).

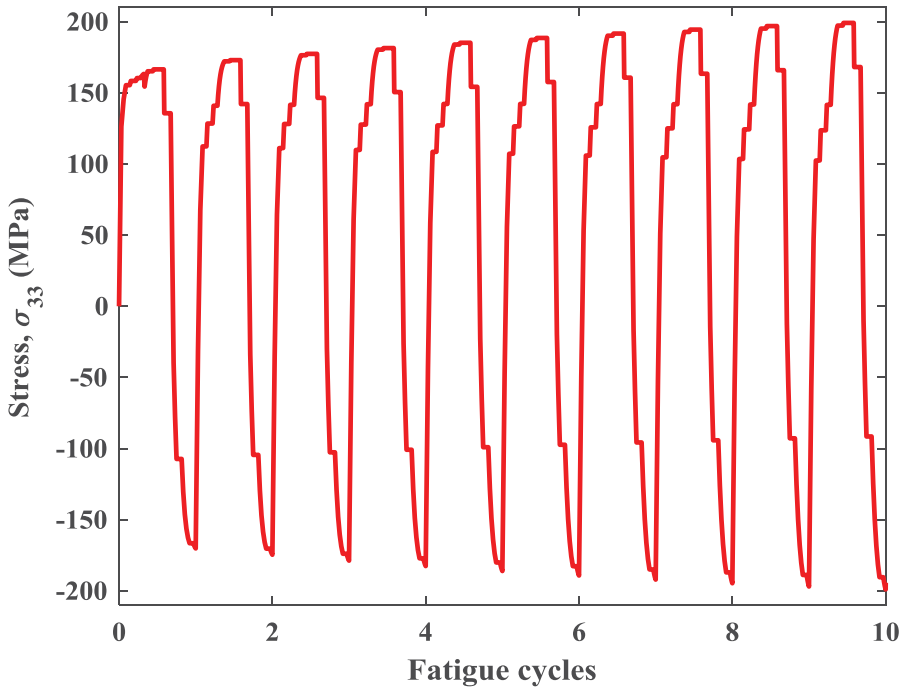

Figure 5. 12 First 10 cycles of simulated stress history for ET-F48 (case 2).

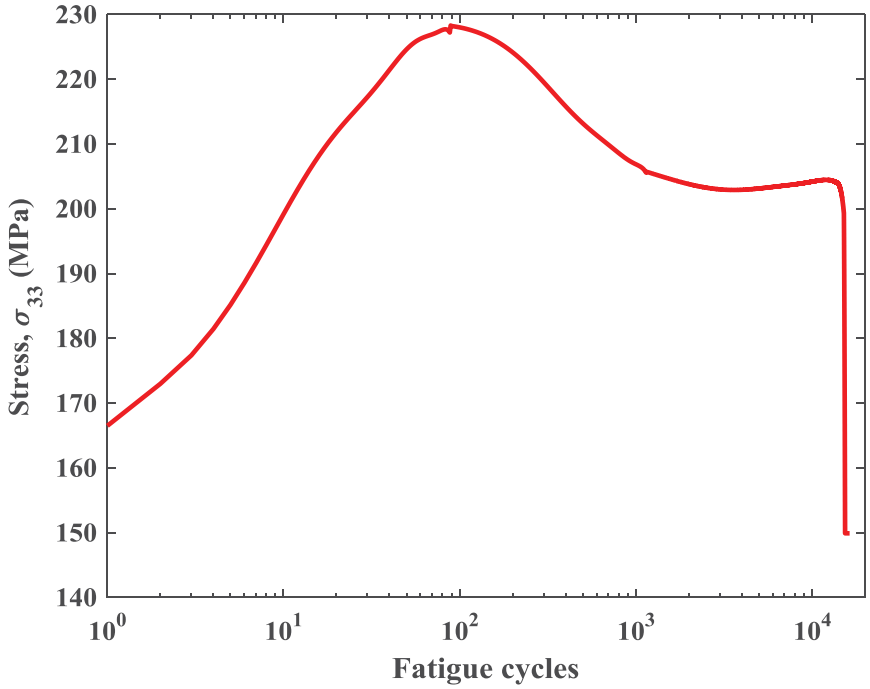

Figure 5. 13 Simulated fatigue cycles versus maximum stress amplitudes for ET-F48 (case 2).

The discrepancy in simulated stress history with respect to experiment for cases 1 and 2 could be due to multiple reasons that require further attention. For example, the following are the possible causes and the corresponding remedial steps for further improving the results.

- **Cause**: Due to usual material scatter. → **Remedial measure**: Perform more fatigue tests to ascertain the behavior.
- **Cause**: Material model based on symmetric fatigue test used for predicting the material behavior in fatigue specimen subjected to asymmetric loading profile. → **Remedial measure**: Use a material model based on asymmetric loading fatigue test data.
- **Cause**: Only gauge portion is FE modeled. → **Remedial measure**: Either fully model the specimen along with entire drive train and/or more tightly control the gauge area temperature to avoid discrepancy associated with differential thermal strain in gauge area.
- **Cause**: Material or strain inertia effect during fatigue testing i.e. the inertia effect associated with rapid transition during high strain rate regime (e.g. during heat up) to lower or zero strain rate regime (e.g during steady state operation) →**Remedial measure**: Selection of smooth transition strain rate, and longer hold time while designing the strain/stress loading input for fatigue testing.

6 Summary and Future Study

6.1 Summary

In this report, we present an HPC-based mechanistic modeling framework for fatigue evaluation of nuclear reactor components, such as PWR SL pipe made from 316 SS base metal. The HPC-based FE modeling framework can mechanistically simulate the stress-strain behavior of test specimens and full components for thousands of fatigue cycles in a reasonable time. This achievement demonstrates the possibility of fully mechanistic fatigue modeling (without using the conventional S~N curve approach) of safety-critical structural components such as nuclear reactor components. We anticipate that use of this approach will reduce the uncertainty in predicted fatigue lives obtained with conventional S~N approaches. This new approach has been validated with respect to experimental data obtained from fatigue tests of 316SS specimens subjected to ideal loading cycles and various design-basis loading cycles. There was a good correlation between the simulated and experimentally observed fatigue lives. The HPC-based modeling framework still is in the development stage and needs further improvement and validation.

6.2 Future Work

Future work envisioned is as follows:

1. Further improve the accuracy of the 316 SS SL pipe prediction results by incorporating asymmetric (with non-zero baseline or mean stress/strain effect) fatigue loading material models.
2. Predict the fatigue cycles for 316 SL pipe under more realistic loading, such as under grid-load-following loading cycles.
3. Extend the material model of 316 SS to capture the PWR coolant water environment, both under design-basis and grid-load-following loading cycles.
4. Study the strain rate and hold effect on 316 SS base metal, when the material is subjected to realistic design-basis and grid-load-following loading cycles.
5. Extend the overall methodology for 316 SS-508 LAS dissimilar metal butter and filler welds and associated reactor components.

References

1. Mohanty, S., Barua, B., Listwan, J., Majumdar, S., and Natesan, K., 2017, "Final Report on CFD and Thermal-Mechanical Stress Analysis of PWR Surge Line under Transient Condition Thermal Stratification and an Evolutionary Cyclic Plasticity Based Transformative Fatigue Evaluation Approach without Using S~N Curve," Argonne National Laboratory, Lemont, IL, Report No. ANL/ LWRS-17/03-rev1.
2. Gamble, R. "Evaluation of pressure-temperature limits for normal RPV startup and shutdown. EPRI-NRC Public Meeting, Rockville, MD, August 28, 2012 (http://pbadupws.nrc.gov/docs/ML1224/ML12243A266.pdf).
3. Barua, B., Mohanty, S., Listwan, J. T., Majumdar, S., & Natesan, K. (2018). Methodology for Stress-Controlled Fatigue Test Under In-Air and Pressurized Water Reactor Coolant Water Condition and to Evaluate the Effect of Pressurized Water Reactor Water and Loading Rate on Ratcheting. *Journal of Pressure Vessel Technology*, *140*(3), 031403.
4. Mohanty, S., Soppet, W. K., Majumdar, S., & Natesan, K. (2015, July). Pressurized Water Reactor Environment Effect on 316 Stainless Steel Stress Hardening/Softening: An Experimental Study. In *ASME 2015 Pressure Vessels and Piping Conference* (PVP2015-45694, pp. V06AT06A038-V06AT06A038). American Society of Mechanical Engineers.

5. Mohanty, S., Soppet, W. K., Majumdar, S., and Natesan, K., 2015, "Tensile and Fatigue Testing and Material Hardening Model Development for 508 LAS Base Metal and 316 SS Similar Metal Weld Under In-air and PWR Primary Loop Water Conditions," Argonne National Laboratory, Lemont, IL, Report No. ANL/LWRS-15/02.
6. Mohanty, S., Soppet, W. K., Majumdar, S., and Natesan, K., 2016, "ChabocheBased Cyclic material Hardening Models for 316 SS–316 SS Weld Under inAir and Pressurized Water Reactor Water Conditions," Nuclear Engineering and Deign., 305, pp. 524–530.
7. Mohanty, S., Soppet, W. K., Majumdar, S., and Natesan, K., 2015, "Effect of Pressurized Water Reactor Environment on Material Parameters of 316 Stainless Steel: A Cyclic Plasticity Based Evolutionary Material Modeling Approach," ASME Paper No. PVP2015-45701.
8. Mohanty, S., Barua, B., Soppet, W. K., Majumdar, S., and Natesan, K., 2016, "Study the Cyclic Plasticity Behavior of 508 LAS Under Constant, Variable and Grid-Load-Following Loading Cycles for Fatigue Evaluation of PWR Components," Argonne National Laboratory, Lemont, IL, Report No. ANL/ LWRS-16/03.
9. Barua, B., Mohanty, S., Soppet, W. K., Majumdar, S., and Natesan, K., 2017, "Fatigue Modeling of 508 LAS Under Variable Amplitude Loading: A Mechanistic Based Analytical Approach," ASME Paper No. PVP2017-65876.

10. Ahmad, A., 2007, "Parallel Programming in the Finite Element Method," Proceedings of Failure of Engineering Materials and Structures, pp. 87-93.
11. Liu, W., Wang, R., 2009, "December. Parallel Computing Based Finite Element Analysis," 1st International Conference on In Information Science and Engineering, pp. 295-298.

12. Choporov, S.V., 2013, "Parallel computing technologies in the finite element method," Radio Electronics, Computer Science, Control 2.
13. Thompson, J.F., Soni, B.K., Weatheril, N.P., 1999, "Hand book of grid generation," CRC Press, New York.
14. Heister, T., Kronbichler, M., Bangerth, W., 2010, "Massively parallel finite element programming," European MPI Users' Group Meeting, pp. 122-131.
15. Chapman, B., Jost, G., Van Der Pas, R., 2008, "Using OpenMP: portable shared memory parallel programming," MIT press, Vol. 10.
16. Pan, Y., 2002, "Teaching parallel programming using both high-level and low-level languages," International Conference on Computational Science, pp. 888-897.
17. Jin, H., Jespersen, D., Mehrotra, P., Biswas, R., Huang, L., Chapman, B., 2011, "High performance computing using MPI and OpenMP on multi-core parallel systems," Parallel Computing 37, pp. 562-575.
18. Hochstein, L., Basili, V. R., 2008, "The ASC-alliance projects: a case study of large-scale parallel scientific code development," Computer 41, pp. 50–58.
19. Hochstein, L., Shull, F., Reid, L. B., 2008, "The role of MPI in development time: a case study," ACM/IEEE Conference on Supercomputing.
20. Rabenseifner, R., Hager, G., Jost, G., 2009, "Hybrid MPI/OpenMP parallel programming on clusters of multi-core SMP nodes," 17th Euromicro International Conference on Parallel, Distributed and Network-based Processing
21. http://www.warp3d.net/
22. Barua, B., Mohanty, S., Listwan, J. T., Majumdar, S., & Natesan, K. (2018). A Cyclic-Plasticity-Based Mechanistic Approach for Fatigue Evaluation of 316 Stainless Steel Under Arbitrary Loading. *Journal of Pressure Vessel Technology*, *140*(1), 011403.
23. WARP3D User Manual: 3-D dynamic nonlinear fracture analyses of solids using parallel computers, Structural Research Series (SRS 607) UILU-ENG-95-2012, University of Illinois at Urbana-Champaign. *University of Illinois at Urbana-Champaign, https://www.dropbox.com/s/xajaedhsi4i2lvz/WARP3D_Manual.pdf?dl=0 (Last revision March 1, 2018).*

This page intentionally left blank

Nuclear Engineering Division
Argonne National Laboratory
9700 South Cass Avenue, Bldg. 208
Argonne, IL 60439

www.anl.gov